TECHNISCHE UNIVERSITÄT MÜNCHEN

TUM School of Natural Sciences

Spin Wave Imaging Using Nitrogen-Vacancy Centers in Diamond

Carolina S. I. Lüthi

Vollständiger Abdruck der von der von der TUM School of Natural Sciences der Technischen Universität München zur Erlangung des akademischen Grades einer

Doktorin der Naturwissenschaften (Dr. rer. nat.)

genehmigten Dissertation.

Vorsitz: Prof. Dr. David Egger
Prüfende der Dissertation: 1. Prof. Dr. Christian Back
2. Prof. Dr. Dominik Bucher

Die Dissertation wurde am 21.10.2024 bei der Technischen Universität München eingereicht und durch die TUM School of Natural Sciences am 02.12.2024 angenommen.

Carolina Lüthi
Spin Wave Imaging Using Nitrogen-Vacancy Centers in Diamond
Dissertation, October, 2024
Reviewers: Prof. Dr. Christian Back and Prof. Dr. Dominik Bucher

Technische Universität München
Lehrstuhl für Experimentalphysik funktionaler Spinsysteme
James-Franck-Straße 1
85748 Garching

CONTENTS

ABSTRACT

In this dissertation, nitrogen-vacancy (NV) centers in diamond are used for the detection and imaging of spin waves. For this purpose, three NV center microscopes were developed: a confocal NV center microscope using a lock-in amplifier for low-noise measurements, a combined confocal NV center and time-resolved magneto-optical Kerr effect (TR-MOKE) microscope with the aim of enabling the simultaneous imaging of spin waves using both techniques, and a widefield NV center microscope for fast data acquisition. To demonstrate the functionality of these setups, optically detected magnetic resonance measurements were performed to determine the strength of external magnetic fields, the coherent control of NV centers was demonstrated through pulsed measurements to measure relaxation times and Rabi oscillations, and magnetic domains in Permalloy squares were imaged. A major focus of this work lies on the use of shallowly implanted NV centers to image spin waves in yttrium iron garnet thin films. The dispersion of Damon-Eshbach spin waves was determined and a comparative analysis with TR-MOKE imaging highlights the strengths and limitations of NV-based spin wave imaging.

KURZFASSUNG

In dieser Dissertation werden Stickstoff-Fehlstellen-Zentren (NV-Zentren) in Diamant zur Detektion und Bildgebung von Spinwellen eingesetzt. Zu diesem Zweck wurden drei NV-Zentren-Mikroskope entwickelt: ein konfokales NV-Zentren-Mikroskop mit einem Lock-in Verstärker für rauscharme Messungen, ein kombiniertes konfokales NV-Zentren- und zeitaufgelöstes magneto-optisches Kerr-Effekt (TR-MOKE)-Mikroskop, mit dem Ziel die gleichzeitige Abbildung von Spinwellen durch beide Techniken zu ermöglichen, sowie ein Weitfeld-NV-Zentren-Mikroskop für die schnelle Erfassung von Messdaten. Zur Demonstration der Funktionalität der Aufbauten wurden optisch detektierte magnetische Resonanzmessungen durchgeführt, um die Stärke externer Magnetfelder zu bestimmen. Die kohärente Kontrolle von NV-Zentren wurde durch gepulste Messungen zur Bestimmung von Relaxationszeiten und Rabi-Oszillationen demonstriert und magnetische Domänen in Permalloy-Quadraten wurden abgebildet. Ein zentraler Schwerpunkt dieser Arbeit liegt auf der Verwendung eines Ensembles von NV-Zentren zur Messung und Abbildung von Spinwellen in Yttrium-Eisen-Granat Dünnfilmen. Die Dispersion von Damon-Eshbach Spinwellen wurde sowohl durch NV-Zentren als auch durch TR-MOKE Messungen bestimmt und eine vergleichende Analyse diskutiert die Stärken und Schwächen der NV-basierten Abbildung von Spinwellen.

PREFACE

Für Aline, Nico, meine Mutter und mein Vater.

Lüthi Carolina
Munich, August 2024

1

INTRODUCTION

Contemporary computing systems rely on principles where information is stored in electric charge or voltage, and computation is driven by charge manipulation. Complementary metal-oxide semiconductor (CMOS) field-effect transistors, crucial to integrated circuits, offer high density, low power consumption, and cost-effectiveness [1–4]. However, the clock speed of CMOS-based processors has plateaued as transistors approach atomic scale, accompanied by rising fabrication costs, raising concerns regarding the viability of Moore's law [5], which states that the number of transistors on a microchip doubles approximately every two years. This has spurred exploration into alternative technologies beyond CMOS to advance computation platforms [1, 6–15]. A promising field of research is spintronics, which exploits the spin degree of freedom for information processing.

In magnon spintronics, devices and circuits utilize spin currents carried by magnons, the quanta of spin waves. Spin transport by magnons offers advantages such as separating spin motion from charge motion, thereby minimizing energy dissipation due to Ohmic losses. Moreover, the magnon spectrum spans from GHz to THz frequencies, facilitating high-speed computation, as the spin wave frequency sets the maximum clock rate of a computing device. Furthermore, the wavelength of spin waves can reach down to just a few nanometers, with the minimum wavelength constrained by the lattice constant of the magnetic material. This ultimately sets the lower limit for the size of wave-based computing elements [16]. Consequently, spin waves facilitate efficient downscaling of wave-based computing elements.

Potential applications of spin waves in information processing and spintronic devices are for example spin wave logic gates [17] and spin wave transistors [18]. Unlike conventional logic gates, which rely on the flow of electrical current, where binary states are represented by low or high voltage, spin wave logic gates operate based on interference patterns created when two or more spin waves interact [17]. Similarly, spin wave transistors modulate the amplitude or phase of spin waves to encode and transfer information, analogous to how traditional transistors control the flow of electrical current [18]. While these devices have proven feasible in research settings, they remain in the experimental phase and are not yet commercially produced. The development of such devices requires a deep understanding of the properties of spin waves, including their excitations, propagation, and interaction with other physical phenomena.

In the field of magnonics, the ferrimagnetic insulator yttrium iron garnet (YIG) is of great importance due to its extremely low intrinsic Gilbert damping $\alpha = 2.7(5) \times 10^{-5}$ [19] and the remarkably long spin wave propagation length, which can extend up to several centimeters [20]. It is widely used as a prototypical material in various experiments [18, 21–23] and is essential for microwave technology. Furthermore, polycrystalline metallic films of Permalloy (Py)[24, 25] are often used materials as well, as they combine a relatively low magnetic damping with good suitability for microsized patterning. In this work, we therefore use YIG and Py as example materials for the study of spin waves and magnetic domains.

Due to the great interest in both the application of spin waves in information technology and their fundamental physics, many techniques have been developed to study spin waves. For non-local detection of spin waves broadband ferromagnetic resonance [26], inverse spin-Hall effect [27, 28], and inelastic neutron scattering [29–31] measurement techniques are often used. Important techniques for imaging spin waves are X-ray scattering [32–34], Brillouin light scattering [35–37], and imaging based on the magneto-optical Kerr effect [38, 39]. However, these methods often have limitations in terms of spatial resolution and sensitivity, particularly when studying spin waves in nanoscale systems or beneath opaque materials, or they need large and expensive facilities for their implementation, as in the case of X-ray microscopy.

One promising novel platform for studying spin waves is the nitrogen-vacancy (NV) center in diamond. The NV center is a defect in the diamond lattice consisting of a substitutional nitrogen atom and a missing carbon atom [40–42]. It exhibits remarkable properties including long spin coherence times of up to two milliseconds at room temperature in highly purified diamond samples [43–45], the ability to detect magnetic fields with high sensitivity of $\mathrm{nT}/\sqrt{\mathrm{Hz}}$ and spatial resolution in the range of 10 nm to a few microns, depending on whether a single NV center or an ensemble is used [42, 46–53], and its sensitivity to temperature variations with a resolution of $\mathrm{mK}/\sqrt{\mathrm{Hz}}$ [54, 55]. By using an ensemble of NV centers instead of a single NV, the magnetic field sensitivity can be further enhanced by a factor of $1/\sqrt{N}$, where N is the number of NV centers [56]. Using high-density ensembles of NV centers, magnetic field sensitivities of $\mathrm{pT}/\sqrt{\mathrm{Hz}}$ [45] can be achieved. These properties, combined with a high photostability at room temperature [45] make NV centers an ideal candidate for detecting magnetic fields and spin wave excitations.

In particular, NV centers can be used to image spin waves by detecting their magnetic stray field. By coupling the NV center to a magnetic material, either by placing a diamond chip on a magnetic sample or by direct contact via a NV center tip, the NV center can sense the magnetic field changes induced by the spin waves and provide information about their properties such as frequency, wavelength, and damping [57]. In [58], an ensemble of NV centers was used to characterize the spin wave damping underneath metal electrodes in a YIG thin film. Additionally, an ensemble of NV centers was used to study spin waves propagating underneath an optically opaque superconductor. This enabled insight into the nature of the spin wave-superconductor interaction and provided the opportunity to control the propagation, dispersion, and refraction of spin waves [59]. It is also possible to detect the magnetic field noise from magnons by measuring the lifetimes of nearby NV center spin states. Magnetic noise creates stray fields in the GHz range, reducing the lifetimes of the NVs, thus allowing the measurement of the spectral profile of thermally excited spin wave noise, as demonstrated in [56]. In [60], relaxometry measurements with a single NV center were used to image non-collinear antiferromagnetic spin textures by probing the magnetic noise generated by thermal magnons. The increased spin relaxation rate of the NV defect, induced by this magnetic noise, led to a reduction in its photoluminescence (PL) signal under continuous laser illumination, which enabled imaging of domain walls, spin spirals, and antiferromagnetic skyrmions.

Given the unique capabilities of NV centers to probe magnetic phenomena, this work focuses on the implementation of NV center microscopy for the study of magnetic spin waves and domains. It is organized as follows:

In Chapter 2, we begin with a discussion of the theoretical background of spin waves. This chapter covers the static and dynamic properties of ferromagnets which are needed for understanding the experimental results presented later. It includes an introduction to magnetism and magnetic domains as well as a discussion of the relevant energy contributions in magnetic materials. The chapter also derives the conditions for ferromagnetic resonance and examines how the orientation of an external magnetic field influences the spin wave dispersion. Finally, it covers inductive spin wave excitation, a method employed in our experiments.

In Chapter 3, we examine the properties of NV centers. We first introduce the diamond host material and then explain the characteristics of NV centers, including their charge states and electronic structure. We then present how NV centers are used to detect static and oscillating magnetic fields. We conclude the chapter with a discussion on detecting and imaging spin waves using NV centers.

Chapter 4 introduces the sensing and imaging techniques employed using ensembles of NV centers to obtain results presented in this thesis. This chapter covers the principles of confocal and widefield microscopy and discusses the spatial resolution of optical microscopes. It describes the assembly and capabilities of three different NV center microscopes that were set up during this thesis and used for the experiments presented in the following chapters.

In Chapter 5, we present initial measurements to characterize the diamonds used. We first provide details about the diamond substrates and the parameters used for nitrogen implantation. We then present optically detected magnetic resonance (ODMR) measurements that examine the dependence of the PL signal on the microwave power and the usage of a $\lambda/2$-wave plate to adjust the contrast in the detected spectra. We also determine the magnitude of an external bias field, a crucial experiment for the reconstruction of magnetic vector fields. The chapter concludes with coherent NV center measurements including lifetime measurements of NV states and the detection of AC magnetic fields through Rabi oscillations.

Chapter 6 discusses the use of shallowly implanted NV centers to measure spin waves in a magnetic thin film, specifically YIG. The chapter introduces the samples used and determines the distance between the NV layer and the YIG surface. It covers the detection and imaging of spin waves using NV centers, the determination of the spin wave dispersion, and a comparison to TR-MOKE imaging. The chapter continues with a phenomenological model to simulate the NV spin wave measurements and concludes with a short summary of the findings.

In Chapter 7, we investigate magnetic domains in Py squares using NV center widefield imaging. This chapter first introduces the sample used and then discusses the application of anti-reflection coatings to enhance the signal quality. It examines the impact of strong field gradients on the magnetic resolution in NV widefield experiments. Furthermore, it presents the results of imaging magnetic domains in demagnetized and uniformly magnetized Py squares and compares these findings to L-MOKE widefield microscopy. The chapter concludes with a summary.

Finally, in Chapter 8 we provide a summary of the results and findings of the thesis and conclude with a discussion of the advantages and limitations of NV centers for spin wave imaging.

2

SPIN WAVES

To understand the physics of spin waves, as well as to provide the necessary theoretical background for the experimental results presented throughout this thesis, we discuss static and dynamic properties of ferromagnets in this chapter. We start with an introduction to magnetism and magnetic domains in the Sections 2.1 and 2.3, respectively, along with a discussion of the relevant energy contributions in magnetic materials in Section 2.2, which is needed in the following sections to describe magnetization dynamics. Starting with the Landau-Lifshitz-Gilbert equation in Section 2.5, we derive conditions for ferromagnetic resonance in Section 2.6. Subsequently, we continue with the discussion of spin wave dispersion and excitation in Section 2.7. The theoretical framework presented follows the reasoning and derivations found in existing references, including textbooks [61–65], literature [57, 66–69], supplemented by additional works [70–76]. These sources provide the basic concepts needed to understand the findings in this thesis.

2.1. INTRODUCTION TO MAGNETISM

Within a uniformly magnetized system with volume V, the macroscopic magnetization $\mathbf{M}$ can also be expressed as

$$\mathbf{M} = \frac{1}{V}\sum_i \mu_\mathbf{i} = \mathbf{m}M_\mathrm{S}. \tag{2.1}$$

Here, $\mu_\mathbf{i}$ represents the effective magnetic moments of the individual atoms within the system. The magnetization vector $\mathbf{M}$ can be decomposed into its unit vector $\mathbf{m}$ times its magnitude M_s, referred to as saturation magnetization. In magnetic solids, the magnetic flux density $\mathbf{B}$ can be described by the external magnetic field strength $\mathbf{H}$ and the magnetization $\mathbf{M}$ using the relation

$$\mathbf{B} = \mu_0(\mathbf{M}+\mathbf{H}) = (\hat{\chi}+1)\mathbf{H}, \tag{2.2}$$

where $\mu_0 = 4\pi \times 10^{-7}\frac{\mathrm{Vs}}{\mathrm{Am}}$ represents the vacuum permeability, $(\hat{\chi}+1)$ is defined as the permeability $\hat{\mu}$, and $\hat{\chi}$ denotes the complex-valued susceptibility tensor, dictating the anisotropic response of the material $\mathbf{H}$.

In the presence of an external magnetic field **H**, the magnetization **M** can be expressed as

$$\mathbf{M} = \hat{\chi}\mathbf{H}. \tag{2.3}$$

In the isotropic case, where $\hat{\chi} = \chi$, the susceptibility enables the classification of materials into diamagnets ($\chi < 0$), paramagnets ($\chi > 0$), ferromagnets or ferrimagnets ($\chi \gg 0$), as well as antiferromagnets ($\chi \approx 0$). In the latter three cases, magnetic moments spontaneously align at temperatures $T < T_c$, where T_c denotes the critical temperature. For ferro- and ferrimagnets, T_c is commonly referred to as the Curie temperature. In this thesis we focus on ferro- and ferrimagnetic materials. Among chemical elements, only iron (Fe), cobalt (Co), nickel (Ni), and gadolinium exhibit ferromagnetism above room temperature. Certain compounds like garnets and alloys of Fe, Ni, and Co frequently exhibit ferri- or ferromagnetism. Examples include Yttrium Iron Garnet $\mathrm{Y_3Fe_5O_{12}}$ (YIG) and permalloy $\mathrm{Ni_{80}Fe_{20}}$ (Py), which are used throughout this work.

2.2. ENERGY CONTRIBUTIONS

To describe the magnetization ground state as well as the magnetization dynamics within a ferromagnet, we need to consider all energy contributions that affect the orientation of the magnetization. The total magnetic energy E_{tot}, normalized to both the volume V and the saturation magnetization M_{S}, is referred to as the total energy density $\epsilon_{\mathrm{tot}} = E_{\mathrm{tot}}/(VM_{\mathrm{S}})$. It can be expressed as [63]

$$\epsilon_{\mathrm{tot}} = \epsilon_{\mathrm{z}} + \epsilon_{\mathrm{ex}} + \epsilon_{\mathrm{d}} + \epsilon_{\mathrm{ani}}. \tag{2.4}$$

Here, ϵ_{z} represents the normalized Zeeman energy density of the magnetization in a static magnetic field **H**, ϵ_{ex} is the normalized exchange energy density, ϵ_{d} refers to the normalized dipolar energy density, and ϵ_{ani} denotes the magneto-crystalline anisotropy energy density. We define the effective magnetic field as [63]

$$\mu_0\mathbf{H}_{\mathrm{eff}} = -\nabla_{\mathbf{m}}\epsilon_{\mathrm{tot}}, \tag{2.5}$$

where $\nabla_{\mathbf{m}} = \left(\frac{\partial}{\partial m_{\mathrm{x}}}, \frac{\partial}{\partial m_{\mathrm{y}}}, \frac{\partial}{\partial m_{\mathrm{z}}}\right)$ represents the gradient along the magnetization unit vector $\mathbf{m} = (m_{\mathrm{x}}, m_{\mathrm{y}}, m_{\mathrm{z}})$. A short overview of relevant contributions is given in the following.

2.2.1. ZEEMAN ENERGY

The Zeeman energy E_{z} arises from the interaction between the magnetization **M** of the system and the external magnetic field $\mathbf{H_0}$. It accounts for the energy change associated with the alignment of magnetic moments in response to $\mathbf{H_0}$ and is expressed as

$$E_{\mathrm{z}} = -\mu_0 \int \mathrm{d}V\, \mathbf{M}\cdot\mathbf{H_0}. \tag{2.6}$$

2.2.2. EXCHANGE ENERGY

The exchange energy E_{ex}, which is responsible for the occurrence of spontaneous magnetization, arises from the interplay between the Coulomb interaction and the Pauli exclusion principle in quantum mechanics. It is determined by the exchange integral J, which represents the overlap of electron wave functions. As a result, the exchange energy decreases rapidly as the spatial separation between spins increases [65]. The exchange energy between two spins $\mathbf{S}_\mathrm{i}$ and $\mathbf{S}_\mathrm{j}$ is expressed as [65]

$$E_{\mathrm{ex,ij}} = -2J\mathbf{S}_\mathrm{i}\cdot\mathbf{S}_\mathrm{j}. \tag{2.7}$$

When the exchange integral J is positive ($J > 0$), there is a preference for parallel alignment of spins. On the other hand, when J is negative ($J < 0$), an antiparallel alignment of spins is favored. This corresponds to ferromagnetic and antiferromagnetic couplings, respectively. In the continuum limit the resulting exchange energy is given by

$$E_{\mathrm{ex}} = A\int \mathrm{d}V(\nabla\mathbf{m})^2, \tag{2.8}$$

where A is the exchange stiffness constant.

2.2.3. DIPOLAR ENERGY

In a magnetized sample with finite size, the presence of magnetic surface charges gives rise to an internal magnetic field, which arises from the dipolar interaction between the magnetic moments and opposes the externally applied magnetic field. This internal field is commonly known as the demagnetizing field. The magnitude of the demagnetizing field can vary significantly depending on the shape of the sample and the direction of the magnetization. The demagnetizing energy contribution is often referred to as shape anisotropy and is non-uniform for arbitrary shapes. It is given by

$$E_\mathrm{d} = -\frac{\mu_0}{2}\int \mathrm{d}V\mathbf{H_d}\cdot\mathbf{M}. \tag{2.9}$$

To simplify the discussion, the analysis can be focused on ellipsoidal shapes, where the demagnetizing fields are uniform and can be expressed as follows [64]

$$\mathbf{H_{dem}} = -\hat{\mathbf{N}}\mathbf{M} = -\begin{pmatrix} N_\mathrm{xx} & N_\mathrm{xy} & N_\mathrm{xz} \\ N_\mathrm{yx} & N_\mathrm{yy} & N_\mathrm{yz} \\ N_\mathrm{zx} & N_\mathrm{zy} & N_\mathrm{zz} \end{pmatrix}\begin{pmatrix} M_\mathrm{x} \\ M_\mathrm{y} \\ M_\mathrm{z} \end{pmatrix}, \tag{2.10}$$

with the demagnetizing tensor $\hat{N}$. The trace of the tensor is given by the sum of its diagonal elements and fulfills

$$\mathrm{Tr}(\hat{\mathbf{N}}) = N_{xx} + N_{yy} + N_{zz} = 1. \tag{2.11}$$

This relationship holds regardless of the shape of the ferromagnetic material, though the individual values of N_{xx}, N_{yy}, and N_{zz} will vary depending on the geometry.

In a coordinate system aligned with the main axes of the ellipsoid, the demagnetization tensor can be simplified to its diagonal components N_xx, N_yy, and N_zz. The dipolar energy density can then be simplified to

$$\epsilon_\mathrm{d} = -\frac{\mu_0}{2}\mathbf{M}\cdot\mathbf{H}_\mathrm{dem} = \frac{1}{2}\mathbf{M}\hat{N}\mathbf{M}. \tag{2.12}$$

When the magnetization is perpendicular to the surface of a thin film (e.g. parallel to the z axis), the demagnetization factors are given by $N_{xx} = N_{yy} = 0$, and $N_{zz} = 1$, while for magnetizations lying in the plane $N_{xx} = N_{yy} = N_{zz} = 0$. To minimize the energy density, the magnetic moments strive to minimize stray fields. In the case of a magnetic thin film, this is accomplished by rotating the magnetization towards the plane of the film and avoiding the strong out-of-plane demagnetizing fields. In real samples, in the absence of any factors favoring a specific direction, demagnetization leads to the formation of magnetic domains, which helps to further reduce the in-plane demagnetizing fields.

2.3. MAGNETIC DOMAINS

Magnetic domains are regions within a ferromagnetic material where the magnetic moments are aligned in the same direction. The formation of magnetic domains can be understood as a mechanism to minimize the total free energy. In a uniformly magnetized ferromagnetic sample, large magnetic surface charges develop on the opposing surfaces, resulting in significant magnetostatic fields and, consequently, magnetostatic energy due to these fields, as illustrated in Fig. 2.1a. The magnetostatic energy can be substantial, especially if the sample has a square-like shape. By forming domains with alternating magnetization directions, the material reduces its magnetostatic energy by minimizing the stray fields. When the magnetization aligns parallel to the sample boundaries, no surface charges are generated because the perpendicular component of the magnetization to the sample surface is zero. This is referred to as the charge-avoidance principle [77] (Fig. 2.1b and c). Conversely, the exchange energy is minimized when the magnetic moments are aligned parallel. Similarly, the anisotropy energy is minimized if the uniform magnetization aligns with the material's easy axis.

In the region between two magnetic domains, known as a domain wall, the magnetization transitions smoothly from the orientation of one domain to that of the other. Within a domain wall, the magnetization is not aligned in parallel, resulting in increased exchange energy and, if the magnetization deviates from the easy axis, anisotropy energy. The formation of domains and domain walls is thus a consequence of minimizing all these contributions to the total free energy.

A common domain configuration in in-plane magnetized thin ferromagnetic films with low anisotropy and lateral sizes in the micrometer range is the Landau state, shown in Fig. 2.1c. In this state, the magnetization within the sample decays into four orthogonal magnetized directions [62, 76, 77].

2.4. MAGNETO-OPTICAL KERR EFFECT

The interaction of light with matter is influenced by the magnetic state of the medium and is linked with the electronic structure of the material. This interaction between electromagnetic radiation and magnetically polarized materials leads to the manifestation of magneto optic effects. We distinguish between the Faraday effect, in which the polarization of linearly polarized light is rotated while passing through a magnetic material, and the Kerr effect, which describes the rotation of the polarization direction of light upon reflection from a magnetic surface. In the following, we discuss the mathematical de-

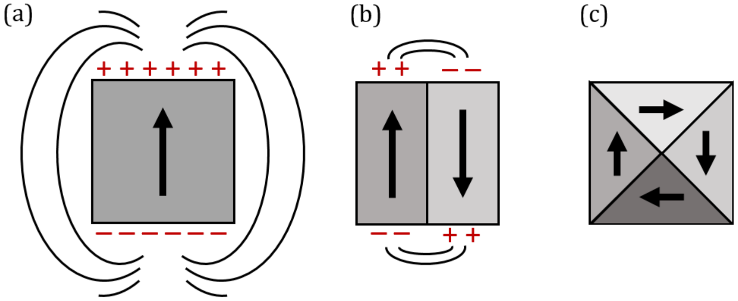

Figure 2.1.: (a) Illustration of a uniformly magnetized ferromagnetic sample showing large magnetic surface charges on opposing surfaces, resulting in significant magnetostatic fields and energy. (b) Formation of magnetic domains with alternating magnetization directions, reducing the magnetostatic energy by minimizing the stray fields. (c) Landau state in an in-plane magnetized thin ferromagnetic film, where the magnetization decays into four orthogonal magnetized directions.

scription of the Kerr effect based on [78].

Light propagation in a ferromagnet is described by the Maxwell equations and the macroscopic properties of the ferromagnet. As the effect of a magnetic permeability tensor $\hat{\mu}(\omega)$ on optical phenomena is small, we assume that $\hat{\mu} = \mu_0 \mathbb{1}$, where μ_0 is the magnetic permeability in vacuum and $\mathbb{1}$ is the identity matrix. Therefore, the macroscopic property of the material is specified by the dielectric permeability tensor $\hat{\varepsilon}(\omega)$, which is given by

$$\mathbf{D} = \varepsilon_0 \hat{\varepsilon}(\omega)\mathbf{E}, \tag{2.13}$$

where $\mathbf{D}$ is the electric displacement vector, ε_0 is the dielectric permeability in vacuum, and $\mathbf{E}$ is the electric field vector of light. In the following, we will consider a material with cubic symmetry and a magnetization $\mathbf{M}$ aligned with the z-direction. Due to the magnetization $\mathbf{M}$, which induces a preferential axis for the system of electrons in the material, $\hat{\varepsilon}(\omega)$ becomes anisotropic

$$\hat{\varepsilon}(\mathbf{M},\omega) = \begin{pmatrix} \varepsilon_{xx} & \varepsilon_{xy} & 0 \\ -\varepsilon_{xy} & \varepsilon_{xx} & 0 \\ 0 & 0 & \varepsilon_{zz} \end{pmatrix}. \tag{2.14}$$

We now solve the Maxwell equations,

$$\nabla \times \mathbf{E} = -\mu_0 \frac{\partial \mathbf{H}}{\partial t}, \tag{2.15}$$

$$\nabla \times \mathbf{H} = \varepsilon_0 \hat{\varepsilon} \frac{\partial \mathbf{E}}{\partial t}, \tag{2.16}$$

with a plane wave ansatz of the following form

$$\mathbf{E} = \mathbf{E}_0 \exp[-i(\omega t - \mathbf{k}\cdot\mathbf{r})], \tag{2.17}$$

$$\mathbf{H} = \mathbf{H}_0 \exp[-i(\omega t - \mathbf{k}\cdot\mathbf{r})]. \tag{2.18}$$

Thereby, we find

$$\mathbf{k}(\mathbf{k}\cdot\mathbf{E}) - k^2\mathbf{E} + \varepsilon_0\mu_0\omega^2\hat{\varepsilon}(\omega)\mathbf{E} = 0, \tag{2.19}$$

with the wave vector $\mathbf{k}$ and the frequency ω of the electromagnetic wave. A more detailed discussion including different orientations can be found in [79]. With $k_0^2 = \varepsilon_0\mu_0\omega^2$, $\mathbf{N} = \mathbf{k}/k_0$, and solving Eq. 2.19 we find

$$\pm iE_x = E_y, \tag{2.20}$$

$$N_\pm^2 = \varepsilon_{xx} \pm i\varepsilon_{xy}. \tag{2.21}$$

The normal modes of the light are $D_\pm = \varepsilon_0 N_\pm^2(E_x \pm iE_y)$, i.e., a right and a left circularly polarized light with complex indices of N_+ and N_-, respectively, traveling at different velocities within the material. The resulting phase shift induces a rotation in the polarization direction and ellipticity of the linearly polarized light. We can calculate the reflection coefficients $r_\pm$ for the right and left circularly polarized light using the Fresnel relations

$$r_+ = \frac{N_+ - 1}{N_+ + 1}, \quad r_- = \frac{N_- + 1}{N_- - 1}. \tag{2.22}$$

As we consider linearly polarized light incident on the magnetic surface given by $\mathbf{E}_{\text{in}} = (E_x, 0, 0)$, the reflected light $\mathbf{E}_{\text{ref}}$ will be given by $(r_xE_x, r_yE_x, 0)$. The reflection coefficients r_x and r_y of the linear polarized can be calculated by

$$r_+ = r_x + ir_y, \quad r_- = r_x - ir_y, \tag{2.23}$$

and thus,

$$r_x = \frac{r_+ + r_-}{2}, \quad r_y = \frac{i(r_+ - r_-)}{2}. \tag{2.24}$$

The Kerr effect can now be understood as a complex rotation

$$\Phi = \theta + i\eta = -\frac{r_yE_x}{r_xE_x}, \tag{2.25}$$

where θ is the Kerr angle and η the ellipticity. Using the expressions in the Eqs. 2.22 and 2.24, we find that for linearly polarized incident light, the reflected light will in general be elliptically polarized with

$$\theta = -\text{Im}\left(\frac{N_+ - N_-}{N_+N_-} - 1\right), \tag{2.26}$$

$$\eta = \text{Re}\left(\frac{N_+ - N_-}{N_+N_-} - 1\right). \tag{2.27}$$

In dependence of the orientation of the magnetization $\mathbf{M}$ and the plane of incidence

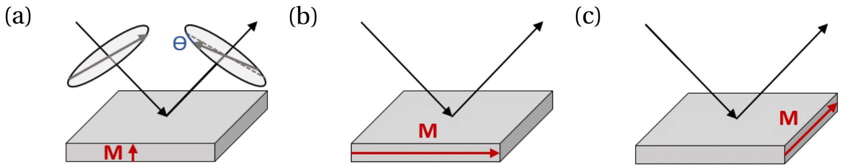

Figure 2.2.: Geometries of the MOKE (a) Polar MOKE. The magnetization **M** is normal to the surface of the magnetic sample from which the linearly polarized electromagnetic wave is reflected. After reflection the polarization is shifted by the angle θ. (b) Longitudinal MOKE. **M** is aligned in the sample plane (IP) and lies in the plane of incidence. (c) Transverse MOKE. **M** is aligned IP and normal to the plane of incidence.

of the electromagnetic wave we distinguish three configurations schematically shown in Fig. 2.2. If **M** is aligned with the out-of-plane direction of the sample, it is referred to as the polar MOKE (PMOKE) effect, where the Kerr effect is strongest. The case where **M** is aligned in the sample plane (IP) and parallel to the plane of incidence is called longitudinal MOKE (LMOKE). When **M** is oriented IP, but perpendicular to the plane of incidence, it is referred to as transverse MOKE. In Chapter 4, we will discuss how PMOKE is used for time-resolved measurements of magnetization dynamics, known as TR-MOKE experiments. This is necessary to understand the results in Chapter 6. Furthermore, in Chapter 7 we will use LMOKE to image magnetic domains.

2.5. MAGNETIZATION DYNAMICS

The dynamics of magnetization in solid-state materials represents a collective behavior, where magnetic moments undergo precession around the effective field direction with a specific phase relationship. Ferromagnetic resonance occurs when the precession phase of all magnetic moments is uniform throughout the material, as depicted in Fig. 2.3a. Conversely, spin waves occur when there is non-uniform precession with a finite phase difference between neighboring spins, as illustrated in Fig. 2.3b.

2.5.1. LANDAU-LIFSHITZ-GILBERT EQUATION

Having evaluated the possible energies contributing to the effective magnetic field in 2.2, we now mathematically describe the magnetization dynamics within a magnetic sample. In static situations, the magnetic moment aligns itself parallel to the effective field direction. However, when deviations from the equilibrium position occur, a torque **T** arises [67]

$$\mathbf{T} = \frac{\mathrm{d}\mathbf{J}}{\mathrm{d}t} = V\mu_0 \mathbf{M} \times \mathbf{H_{eff}}. \tag{2.28}$$

Furthermore, **M** is proportional to the angular momentum **J**

$$\mathbf{M} = -\gamma \frac{\mathbf{J}}{V}, \tag{2.29}$$

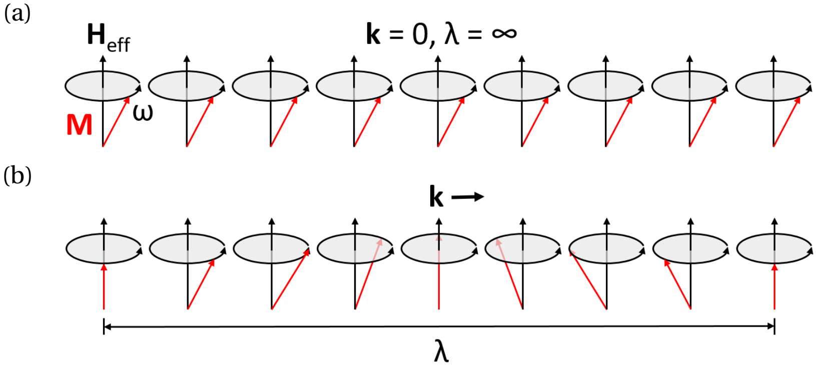

Figure 2.3.: Sketch illustrating the collective excitation of magnetic moments **M** oscillating with frequency ω around an effective field $\mathbf{H_{eff}}$. In (a) the phase difference between the magnetic moments vanishes, resulting in a $\mathbf{k} = 0$ ($\lambda = \infty$) wave vector while in (b), the phase difference is not zero resulting in a propagating spin wave with a wave vector $\mathbf{k} > 0$ and wavelength λ.

where $\gamma = g\mu_B/\hbar$ is the gyromagnetic ratio, with the Landé-factor g and the Bohr magneton μ_B. Combining the two equations above results in the undamped Landau-Lifshitz equation [80], which describes the torque acting on the magnetization, leading to a precessional motion of **M** around $\mathbf{H_{eff}}$

$$\frac{\mathrm{d}\mathbf{M}}{\mathrm{d}t} = -\gamma\mu_0 \mathbf{M} \times \mathbf{H_{eff}}. \tag{2.30}$$

Up to now, we neglected that in a real system, many different dissipation mechanism will result in a relaxation of the precession. This energy dissipation can be accounted for by including a phenomenological damping term to Eq. 2.30, that is proportional to a dimensionless damping constant α. Such a damping term was introduced by T. Gilbert [68], which resulted in the famous Landau-Lifshitz-Gilbert (LLG) equation

$$\frac{\mathrm{d}\mathbf{M}}{\mathrm{d}t} = \underbrace{-\gamma\mu_0 \mathbf{M} \times \mathbf{H_{eff}}}_{\text{precession}} + \underbrace{\frac{\alpha}{M_s}\mathbf{M} \times \frac{\mathrm{d}\mathbf{M}}{\mathrm{d}t}}_{\text{damping}}. \tag{2.31}$$

In Fig. 2.4 the damped precessional motion of **M** is depicted. For large α the process of relaxation towards equilibrium occurs rapidly.

2.6. FERROMAGNETIC RESONANCE

To mathematically describe the case of ferromagnetic resonance, we employ the theoretical framework of the macrospin model. In that case, the effective field accounts for the external field $\mathbf{H_0}$ and the demagnetizing field $\mathbf{H_{dem}}$, but not for exchange interaction. Thereby, we simplify the description of the magnetization dynamics by treating

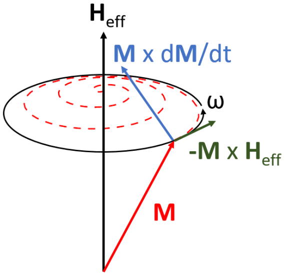

Figure 2.4.: Precessional motion of the magnetization **M** around the external field $\mathbf{H}_{\mathbf{eff}}$ at frequency ω. The black line depicts the undamped motion of Eq. 2.30, while the red dashed line shows the damped case described by Eq. 2.31.

the magnetic material as a single macroscopic magnetic moment, disregarding spatial variations within the sample. This simplification holds true when factors like strong external magnetic fields or significant anisotropies induce fully saturated magnetization. Furthermore, to counter the damped precession shown in Fig. 2.4 a homogeneous driving field, $h_{\text{rf}x,y}(t) = h_{\text{rf}x,y} \cdot \exp(-i\omega t)$, which has a frequency matching the precession frequency of **M** is also included. The total effective field is thus given by

$$\mathbf{H}_{\mathbf{eff}} = \mathbf{H}_{\mathbf{0}} + \mathbf{H}_{\mathbf{dem}} + \mathbf{h}_{\mathbf{rf}}(t) = \begin{pmatrix} -N_{xx}M_x(t) \\ -N_{yy}M_y(t) \\ H_0 - N_{zz}M_s \end{pmatrix} + \begin{pmatrix} h_{\text{rf},x}(t) \\ h_{\text{rf},y}(t) \\ 0 \end{pmatrix} \tag{2.32}$$

The subsequent derivation of the resonance condition focuses on linear response in a sample with ellipsoidal shape. It is thus only valid for excitation fields with magnitudes a lot smaller than the magnitude of the external magnetic field, which is in the following assumed to point in the z-direction. In this case the z-component of the magnetization stays almost constant, e. g. $M_z \approx M_s$, and it is sufficient to reduce the problem to two dimensions. By using the harmonic ansatz $M_{x,y}(t) = M_{x,y} \cdot \exp(-i\omega t)$, as well as the effective field given in Eq. 2.32, and substituting these expressions into the LLG equation 2.31, we obtain a differential equation that represents the linear response relationship between the driving field and the magnetization

$$\begin{pmatrix} h_{\text{rf},x} \\ h_{\text{rf},y} \end{pmatrix} = \hat{\chi}^{-1} \begin{pmatrix} M_x \\ M_y \end{pmatrix}. \tag{2.33}$$

By inverting $\hat{\chi}^{-1}$ and dividing it by M_s, we find the dimensionless, complex Polder susceptibility [81]

$$\hat{\chi} = \frac{1}{\det(\hat{\chi}^{-1})M_s} \cdot \begin{pmatrix} H_0 + (N_{yy} - N_{zz})M_s - \frac{i\omega\alpha}{\gamma\mu_0} & -\frac{i\omega}{\gamma\mu_0} \\ \frac{i\omega}{\gamma\mu_0} & H_0 + (N_{xx} - N_{zz})M_s - \frac{i\omega\alpha}{\gamma\mu_0} \end{pmatrix}. \tag{2.34}$$

The resonance frequency ω_{res} can now be calculated by setting $\det(\hat{\chi}^{-1}) = 0$ and taking the real part of the solution, as $\alpha << 1$. In the case of a ferromagnetic thin film, the resonance frequencies are given by the Kittel equation [67]

$$\omega_{\text{res}} = \gamma\mu_0\sqrt{(H_{\text{res}} + M_s(N_{xx} - N_{zz}))(H_{\text{res}} + M_s(N_{yy} - N_{zz}))}. \tag{2.35}$$

In Fig. 2.5a the resonance frequencies calculated from Eq. 2.35 for the in-plane ($N_{\text{xx}} = 1, N_{\text{yy}} = 0, N_{\text{zz}} = 0$) configuration are shown as a function of the external magnetic field $\mathbf{H}_{\text{ext}}$.

2.7. SPIN WAVES

We now continue with the discussion of spin waves, where adjacent spins oscillate with a constant phase shift between each other. The correlation between the frequency of an excitation and its wavelength is referred to as dispersion. The gradient of the dispersion, known as group velocity, indicates the direction and velocity of the energy transport within the system. In the following, we will discuss the analytical solution of the LLG-Eq. 2.31, yielding the spin wave dispersion as derived by Kalinikos and Slavin [66].

2.7.1. DISPERSION

To describe the dynamics of spin waves, we need to account for the external field $\mathbf{H_0}$ and the dipolar field $\mathbf{H_{dem}}$, the exchange field $\mathbf{H_{ex}}$, and the driving field $\mathbf{h_{rf}}$. The effective field is thus given by

$$\mathbf{H_{eff}} = \mathbf{H_0} + \mathbf{H_{dem}} + \mathbf{H_{ex}} + \mathbf{h_{rf}}(t) \tag{2.36}$$

We consider a thin film of thickness d in the yz-plane. The coordinate system is chosen such that spin waves propagate along the z-direction. Furthermore, the polar angle θ and the azimuthal angle ϕ describe the relationship between the propagation direction $\mathbf{k}$ and the external field $\mathbf{H_0}$, indicated in Fig. 2.5b. As in the case of FMR, we assume a small deviation from the equilibrium saturation magnetization, such that $M_z \approx M_{\text{S}}$, and use the condition that spins near the surface are unpinned, allowing them to precess freely. Utilizing a plane wave ansatz to solve the LLG-Eq. 2.31, the dispersion relation reads [66]

$$\omega = \mu_0\gamma\sqrt{(H_i + H_{\text{ex}})(H_i + H_{\text{ex}} + M_{\text{S}}F)}, \tag{2.37}$$

where H_i is the effective internal field within the sample, and F is given by

$$F = P + \sin^2\theta_{\text{i}}\left(1 - P(1+\cos^2\phi) + \frac{M_{\text{S}}}{H_i + H_{\text{ex}}}P(1-P)\sin^2\phi\right). \tag{2.38}$$

Furthermore, $P = 1 - (1 - \mathrm{e}^{-|k_z d|})/(|k_z d|)$, and the polar angle θ_{i} between $\mathbf{k}$ and the effective field inside the sample $\mathbf{H_i}$ satisfies the following system of equations

$$\begin{aligned} H_i\cos\theta_{\text{i}} &= H_0\cos\theta - M_{\text{S}}\cos\theta_{\text{i}} \\ M_{\text{S}}\sin 2\theta_{\text{i}} &= 2H_0\sin(\theta_{\text{i}} - \theta). \end{aligned} \tag{2.39}$$

Three important cases of spin wave propagation are distinguished based on the orientation of the magnetization in a magnetic film and the wave vector, as illustrated in Fig. 2.5b.

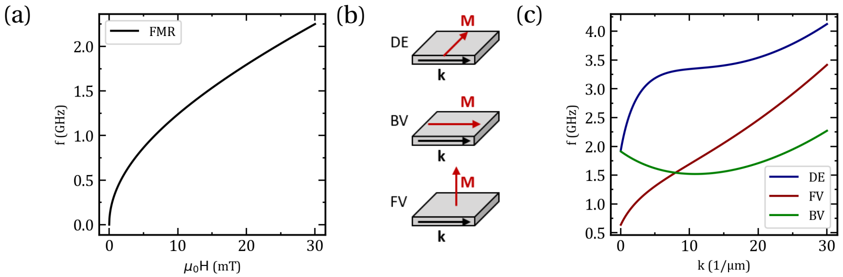

Figure 2.5.: (a) Ferromagnetic resonance: Resonance frequencies calculated from Eq. 2.35 if the external magnetic field $\mu_0\mathbf{H}$ is applied in the sample plane ($N_{xx} = 1, N_{yy} = N_{zz} = 0$). (b) Configurations for BV, FV, and DE spin waves in a thin film, determined by the angles between the magnetization direction **M** and the propagation direction **k**. (c) Dispersion relations for BV (green), FV (red), and DE (blue) spin waves calculated by Eq. 2.37.

- **Backward Volume Waves:** $\theta = 90°, \phi = 0°$
  Spin waves that propagate parallel to the magnetization direction are called backward volume (BV) spin waves due to their negative group velocity $v_\mathrm{g} = \partial\omega/\partial k < 0$ at small wave vectors **k**.

- **Forward Volume Waves:** $\theta = 0°$
  If the magnetic film is perpendicularly magnetized we talk about forward volume (FV) waves. The dispersion becomes isotropic, as all in-plane wave vectors are perpendicular to the magnetization direction.

- **Damon-Eshbach Waves:** $\theta = 90°, \phi = 90°$
  If the magnetic film is in-plane magnetized and the wave vector of the spin wave is oriented perpendicular to this direction, magnetostatic surface waves, also known as Damon-Eshbach (DE) spin waves, are observed. The dynamic stray field of such waves aligns parallel to the dynamic magnetization on the top surface of the film, while on the bottom surface, it aligns antiparallel. This characteristic results in DE spin waves exhibiting a higher amplitude on one side of the film. Furthermore, the amplitude of DE spin waves decays exponentially as one moves away from the surface, as demonstrated by Damon and Eshbach [82]. The stray field $B_\mathrm{sw}(z,t)$, observed at a height x_0 above the thin film, originating from a DE spin wave propagating along the ±z-direction, is given by [57]

  $$B_\mathrm{sw}(z,t) = -B^0_\mathrm{sw}\mathrm{Re}[e^{i(k_z z-\omega t)}(\hat{\mathbf{z}} + i\mathrm{sgn}(k_z)\hat{\mathbf{x}})], \tag{2.40}$$

  with the stray field amplitude $B^0_\mathrm{sw} = \mu_0 m_0(1+\mathrm{sgn}(k_z)\eta)|\mathbf{k}|de^{-k_z x_0}/2$. Furthermore, **k** is the wave vector, $\omega = 2\pi f$ is the frequency given by Eq. 2.37, η is the degree of ellipticity, d is the thickness of the magnetic thin film, and t is the time. From Eq. 2.40 we find that right-propagating DE spin waves ($+k_z$) produce a left-handed circularly polarized stray field above the sample surface, whereas left-propagating spin waves generate a right-handed circularly polarized stray field. In this work, we will focus on DE spin waves.

In Fig. 2.5c, the dispersion relation of BV, FV, and DE is shown. In the following section, we discuss how spin waves can be excited inductively by a microstrip line.

2.7.2. INDUCTIVE SPIN WAVE EXCITATION

The microwave (MW) current flowing through a microstrip line fabricated on a magnetic thin film induces an MW magnetic field, causing the magnetic moments to deviate from their equilibrium, thus generating a spin wave propagating away from the microstrip line.

The MW field of a microstip line oriented parallel to the y-axis with its center at $x = z = 0$ is given by [57]

$$\mathbf{B}_{\mathrm{MW}}(x,z) = \frac{\mu_0 I}{2\pi w}\left(\arctan\left(\frac{w z_0}{z_0^2 + x^2 - \left(\frac{w}{2}\right)^2}\right)\hat{\mathbf{x}} + \frac{1}{2}\ln\left(\frac{z_0^2+\left(x+\frac{w}{2}\right)^2}{z_0^2+\left(x-\frac{w}{2}\right)^2}\right)\hat{\mathbf{z}}\right), \tag{2.41}$$

where I is the current, w the width of the microstrip line, and z_0 the hight above the sample surface.

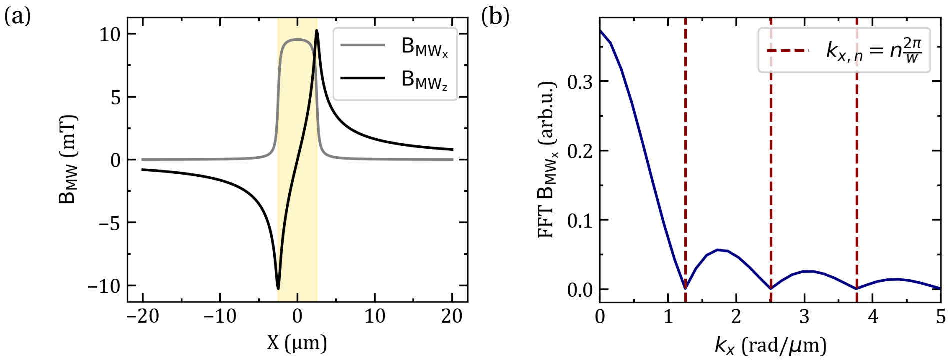

Figure 2.6.: Excitation profile of a microstrip line of width $d = 5\ \mu$m oriented along the y-axis. (a) x- and z-components of the microstrip line magnetic field in real space given by Eq. 2.41. The yellow rectangle marks the dimension of the microstrip line. (b) Fast Fourier transformation of the in-plane MW field as a function of the wave vector magnitude k_x. If $k_x = n \cdot \frac{2\pi}{w}$ the excitation efficiency vanishes (red dashed lines).

Fig. 2.6a shows the in-plane and out-of-plane components of the MW magnetic field given in Eq. 2.41 for a 5 μm wide microstrip line in real-space. The excitation spectra in k-space can be derived by Fourier-transforming the MW field of the microstrip line. In

Fig. 2.6b the k_x component of the wave vector is shown. Only specific values of the spin-wave vector can be excited with a microstrip line. In particular, the excitation efficiency vanishes when an integer number of wavelengths, $k_x = n \cdot \frac{2\pi}{w}$, fits within the width of the microstrip, as indicated by the red dashed lines.

3

NV CENTER MAGNETOMETRY

Advancing the detection and imaging of weak magnetic fields and excitations at the nanoscale is crucial, as many intriguing magnetic phenomena in correlated-electron materials remain difficult to access due to the demanding combination of resolution and magnetic-field sensitivity [83]. To address these challenges, negatively charged nitrogen vacancy centers in diamond have emerged as a new technique for magnetic field sensing. Due to their atomic-sized point defect nature and potential localization in close proximity to a diamond surface, NV centers can be positioned within a few nanometers of magnetic samples, enabling nanoscale spatial resolution down to about 50 nm [84]. Furthermore, their non-invasive nature and high sensitivity to GHz magnetic fields make them ideal for investigating the dynamic excitations of magnetic systems, such as spin waves. In the chapters 5, 7, and 6 we use NV centers for static magnetic field sensing experiments as well as to image spin waves.

In this chapter, we discuss the properties of the NV centers that are essential for understanding this work. We begin by introducing the NV center's host material diamond in Section 3.1. In Section 3.2, we discuss the working principles of nitrogen vacancy (NV) centers, necessary for understanding NV center magnetometry, thereby introducing their charge states and electronic structure. We then proceed to explain how NV centers are used to detect both static and oscillating magnetic fields in Sections 3.3 and 3.4, respectively. We conclude this chapter in Section 3.5 by discussing how NV centers are utilized to detect and image spin waves.

3.1. DIAMOND

To comprehend the characteristics of the nitrogen vacancy center and the subsequent results, we first want to examine the properties and growth of its host material diamond.

3.1.1. DIAMOND PROPERTIES

Diamond possesses a face-centered cubic crystal (fcc) lattice with a two-atom basis as depicted in Fig. (3.1a). Its basic unit cell is a cube with lattice constant $a = 0.357$ nm [85]. The angles between between adjacent carbon-carbon bonds are approximately 109.5° .

Diamond acts as a high band-gap semiconductor with a bandgap of 5.47 eV [86], exhibiting transparency in the visible spectrum. Defects in the diamond lattice create localized states within the band-gap, enabling the absorption and fluorescence of light. However, the rather high refractive index of diamond, $n = 2.4$, limits the detection efficiency of fluorescence light coming from color centers [45]. The total internal reflection angle is as small as $\Theta_c = 22.6°$, such that most of the emitted photons cannot exit the diamonds top surface.

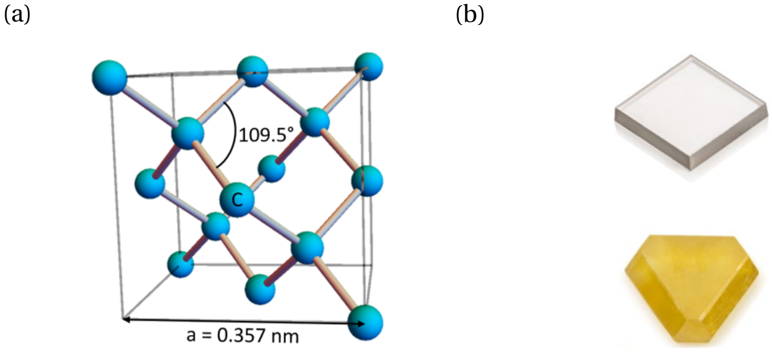

Figure 3.1.: (a) Fcc crystal lattice of diamond with lattice constant $a = 0.357$ nm and bond angles of 109.5°. Carbon atoms are represented as blue spheres. (b) Yellow type I diamond (bottom) and transparent type II diamond (top). Images taken from [87].

The purity and crystallinity of diamond are critical characteristics that significantly impact its properties and potential applications. As the most common impurity in diamond is nitrogen, diamonds are often classified into two types based on their nitrogen concentration [88]. Type I diamonds contain a large concentration of nitrogen impurities, with a nitrogen concentration bigger than 5 parts per million (ppm), making up about 98 % of all natural diamonds. They are further subdivided into type Ia, with an approximate nitrogen concentration of 3000 ppm due to aggregated nitrogen, and type Ib, with a nitrogen concentration of about 300 ppm due to single substitutional nitrogen. The high nitrogen concentration leads to a yellowish color of type I diamonds. Type II diamonds, on the other hand, exhibit minimal nitrogen concentration ($N < 5$ ppm), making them colorless. They are further categorized into type IIa diamonds, predominantly synthetically created, featuring nitrogen as the primary impurity and type IIb diamonds, where boron serves as the major impurity[87]. Fig. (3.1b) shows a colorless type II and a yellow type I diamond. In this thesis we use (100)-oriented type IIa diamond with a nitrogen concentration of less than 1 ppm.

3.1.2. Diamond Growth

Diamonds can be grown by two popular methods. In high pressure, high temperature (HPHT) synthesis the natural conditions under which diamonds form in the Earth's mantle is mimiced. The process typically starts with a carbon source, often graphite, placed in a high-pressure cell along with a metallic solvent, usually consisting of iron, nickel or cobalt, that serves as a catalyst and transport medium, aiding in the diamond growth process, as illustrated in Fig. (3.2a). This assembly is then subjected to extremely high pressures around 5-6 GPa, pushing the carbon atoms into the diamond crystal lattice, and temperatures around 1300 – 1600°C, facilitating the mobility of carbon atoms[89]. Diamonds synthesized using the HPHT method often exhibit a yellow color due to the incorporation of nitrogen from the atmosphere and growth materials into the diamond lattice.

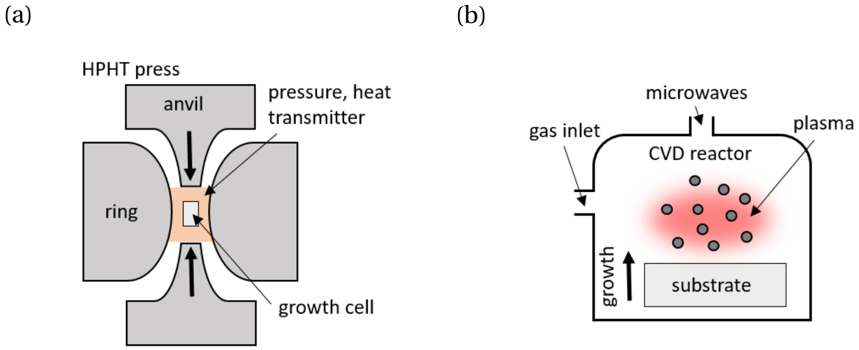

Figure 3.2.: (a) Sketch of a HPHT diamond growth chamber. An anvil press applies through a transmitter solvent extremely high pressures and temperatures to a central growth cell that contains the carbon source and a diamond seed crystal. (b) Sketch of a CVD reactor. A diamond substrate is grown by depositing carbon atoms from a hydrogen and carbon containing gas.

In the chemical vapor deposition (CVD) growth method diamond seed crystals are placed in a vacuum chamber which is filled with a hydrogen and carbon containing gas, such as methane. A microwave beam creates a plasma by breaking down the gas molecules, and the carbon atoms diffuse towards the colder, flat diamond seed crystals. The hydrogen helps to maintain the purity of the growing diamond by selectively removing any non-diamond carbon impurities or amorphous carbon from the surface[90]. In Fig. (3.2b) the sketch of a CVD reactor is shown.

3.2. NITROGEN VACANCY CENTER

The NV defect consists of a nitrogen atom substituting a carbon atom in the diamond crystal lattice, along with a nearby vacancy, as illustrated in Fig. 3.3a. It can align along the four $< 111 >$ crystalline directions of the diamond lattice. The creation of NV centers is achieved through methods such as ion implantation followed by annealing [91, 92]. Ion implantation induces damage by creating carbon vacancies within the diamond lattice as well as nitrogen impurities [93, 94]. Annealing, typically occurring at temperatures ranging from 600 to 1000 °C, allows vacancies to become mobile and combine with nitrogen impurities, thereby forming NV centers [95]. The initial vertical distribution of vacancies is determined by the acceleration voltage.

3.2.1. CHARGE STATES

Two distinct forms of the NV defect have been distinguished, the neutrally charged NV_0 center and the negatively charged NV_- center. When there are five electrons associated with the NV defect, two originating from dangling bonds of the nitrogen atom, and three from the dangling bonds of the vacancy, the neutral nitrogen-vacancy center NV_0 is formed with spin $S = 1/2$. If an additional electron is captured by the defect from lattice donors, a negatively charged NV_- center forms with spin $S = 1$ [96, 97], as depicted in Fig. 3.3b. For magnetometry applications, only the negatively charged form of the defect is of interest, as it possesses a spin triplet ground state that can be effectively initialized, manipulated, and optically read out[45]. Throughout the remainder of this thesis, we will therefore refer to the NV_- as the NV center.

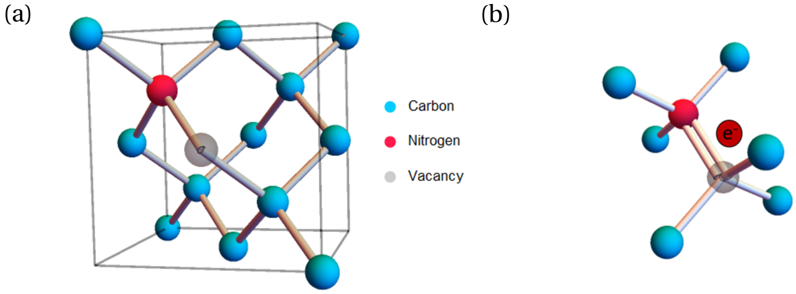

Figure 3.3.: (a) Atomic structure of the NV center in diamond (b) Negatively charged NV center. The electronic structure is composed of six electrons: two from the nitrogen, three from the dangling bonds of the carbon atoms adjacent to the vacancy, and one captured from the lattice, resulting in a $S = 1$ quasi-particle.

3.2.2. ELECTRONIC STRUCTURE

The discussion of this section roughly follows [45]. The NV center energy level scheme consists of ground ($^3A_2$) and excited (^3E) state spin triplets ($S = 1$), as well as intermediate singlet states (^1E,$^1A_1$), depicted in Fig. 3.4a. The ground and excited triplet states are both split in energy due to spin-spin interaction, resulting in a singlet state with $m_s = |0\rangle$ and a doublet with $m_s = \pm|1\rangle$, where m_s is the spin projection along the NV quantization axis. These singlet and doublet states of the ground (excited) states are separated by $D = 2.87$ GHz, ($D_{\text{ex}} = 1.42$ GHz) in the absence of a magnetic field. An external field splits the degenerate $m_s = \pm|1\rangle$ energy levels due to the Zeeman interaction.

The NV center can undergo optical excitation via spin-conserving transitions to the excited state. Following optical excitation, relaxation of the NV defect can occur either through the same radiative transition, leading to broadband red photoluminescence, or via an alternative pathway involving non-radiative intersystem crossing (ISC) to the

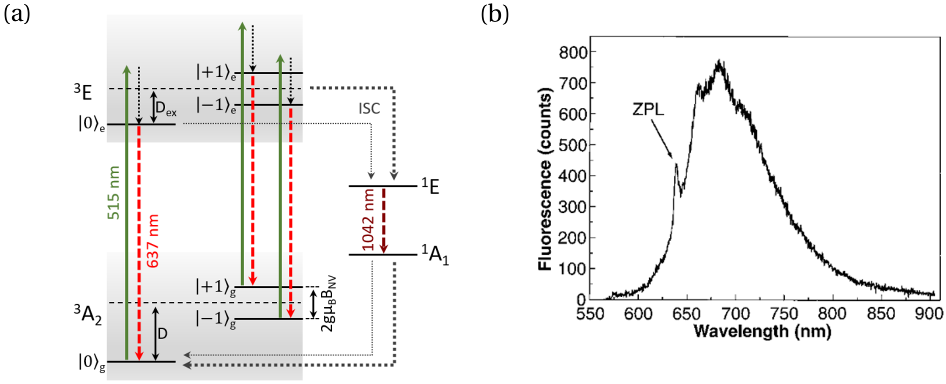

Figure 3.4.: (a) Energy level scheme consisting of a triplet ground state $^3A_2$, a triplet excited state ^3E, as well as intermediate singlet states ^1E and $^1A_1$. The green arrows represent spin-conserving non-resonant optical excitation using a green laser (515 nm) from the ground states to the phonon sideband (gray area). Light red dashed arrows represent decay through spin-conserving optical transitions, dark red dashed arrows indicate the infrared transition at 1042 nm between the singlet states. Furthermore, gray dashed lines represent non-radiative relaxation paths via intersystem crossing (ISC). The thickness of these lines reflects the relative strength of the transition. (b) Fluorescence spectrum of a single NV showing a zero-phonon line at 637 nm and a broad phonon sideband between 600 nm and 800 nm. Adapted from [98].

singlet states. The photoluminescence emission spectrum exhibits a zero-phonon line (ZPL) at 637 nm and a broad phonon sideband (PSB), shown in Fig. 3.4b. The PSB arises from transitions where a photon at the ZPL is accompanied by the excitation/absorption of one phonon. Consequently, the PSB enables non-resonant optical excitation using a green laser.

The $m_s = |0\rangle$ state demonstrates a slower ISC shelving rate to the singlet states compared to the $m_s = \pm|1\rangle$ state. Furthermore, the singlet states preferentially decay towards the $m_s = |0\rangle$ state. These spin-selective mechanisms lead to a significant population of the $m_s = |0\rangle$ state upon optical pumping, enabling optical initialization into the $m_s = |0\rangle$ state. Consequently, the optical transition becomes considerably brighter when the spin resides in the $m_s = |0\rangle$ state. This spin-dependent photoluminescence allows to optically detect the NV spin state.

3.2.3. NV CENTER HAMILTONIAN

The behavior of the NV ground state in an external magnetic field is described by its Hamiltonian $\hat{H} = h \cdot \hat{\mathscr{H}}$, where h is the Planck constant. As we want to calculate the resonance frequencies of a transition, we will use units of frequency for our Hamiltonian. By neglecting the hyperfine interaction with nearby nuclear spins in the diamond as well as second order terms due to strain in the diamond, which are not significant in this thesis, $\hat{\mathcal{H}}$ is given by [45]

$$\hat{\mathcal{H}} = D\hat{S}_z^2 + \gamma \mathbf{B} \cdot \mathbf{S}. \tag{3.1}$$

Here, z is the quantization axis of the NV defect, $\gamma = 2\pi \cdot 28$ MHZ/mT the gyromagnetic ratio, and $\mathbf{S} = (\hat{S}_x, \hat{S}_y, \hat{S}_z)$ denotes the vector of Pauli spin operators for a spin-1 system

$$\hat{S}_x = \frac{1}{\sqrt{2}} \begin{pmatrix} 0 & 1 & 0 \\ 1 & 0 & 1 \\ 0 & 1 & 0 \end{pmatrix}, \quad \hat{S}_y = \frac{1}{\sqrt{2}} \begin{pmatrix} 0 & -i & 0 \\ i & 0 & -i \\ 0 & i & 0 \end{pmatrix}, \quad \hat{S}_z = \begin{pmatrix} 1 & 0 & 0 \\ 0 & 0 & 0 \\ 0 & 0 & -1 \end{pmatrix}. \tag{3.2}$$

By plugging the Pauli matrices into Eq. 3.1 we find

$$\hat{\mathcal{H}} = \begin{pmatrix} D + \gamma B_z & \frac{\gamma}{\sqrt{2}}(B_x - iB_y) & 0 \\ \frac{\gamma}{\sqrt{2}}(B_x + iB_y) & 0 & \frac{\gamma}{\sqrt{2}}(B_x - iB_y) \\ 0 & \frac{\gamma}{\sqrt{2}}(B_x + iB_y) & D - \gamma B_z. \end{pmatrix} \tag{3.3}$$

By diagonalizing the Hamiltonian given in Eq. 3.3, its eigenvalues λ_i can be calculated from the characteristic equation $||\hat{\mathcal{H}} - \lambda_i \mathbb{1}|| = 0$, where $\mathbb{1}$ is the identity matrix. The resonance condition is then obtained by

$$\omega_{+(-)} = \lambda_{3(2)} - \lambda_1, \tag{3.4}$$

with $\lambda_3 > \lambda_2 > \lambda_1$. In the following sections, we will use Eq. 3.4 to calculate the resonance frequencies for an NV center in a static external (DC) field as well as to describe the spin dynamics of an NV center in a oscillating (AC) external magnetic field.

3.3. DETECTION OF DC FIELDS

If a static external field $\mathbf{B} = B_z\hat{\mathbf{z}}$ is applied along the NV center axis (z-direction), Eq. 3.3 simplifies to

$$\hat{\mathcal{H}}_{DC} = \begin{pmatrix} D + \gamma B_z & 0 & 0 \\ 0 & 0 & 0 \\ 0 & 0 & D - \gamma B_z \end{pmatrix}. \tag{3.5}$$

We find that it causes a linear shift of the two ESR frequencies

$$\omega_{\pm} = D \pm \gamma B_z. \tag{3.6}$$

Since we are using an ensemble of NV centers, we will not only measure the transitions of the aligned NVs but also those of the three remaining NV families. The resonance frequencies of these NVs can be calculated in a similar manner. When the field is aligned with one NV direction, the projection of the field along the other three NV directions will result in B_x and B_y components of the same magnitude, while $B_z = 0$, as the field is not aligned with any of the three remaining axes. Thus, solving the Hamiltonian in Eq. 3.3 for $\mathbf{B} = (B_x, B_y, 0)$ will yield the same transition frequencies for the three remaining NV families. Consequently, in an experiment where the external field is aligned along one NV axis, we will measure only four resonances. The outer two resonances correspond to the aligned NV centers, while the inner two resonances are the superposition of the three pairs of resonances from the remaining NV families.

In Fig. 3.5a, we show the calculated ODMR frequencies for an ensemble of NV centers, where the external magnetic field is applied along one of the four possible quantization axes of the NVs. NV centers not aligned with the external field experience a transverse field of the same magnitude for the remaining three quantization axes directions, resulting in a non-linear field dependence.

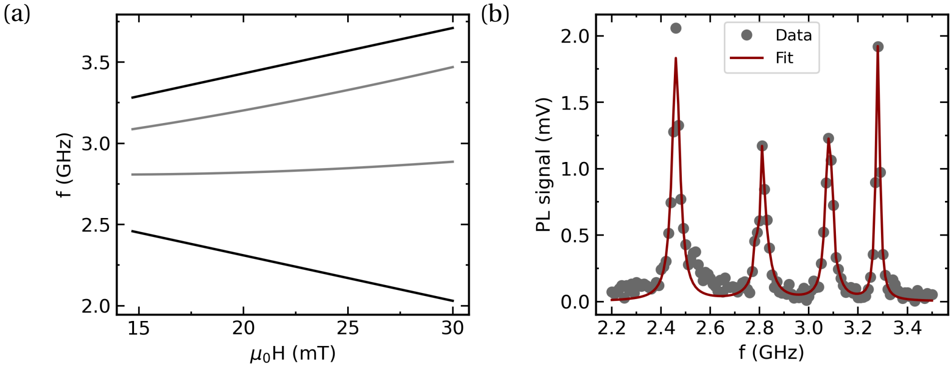

Figure 3.5.: ODMR spectrum of an ensemble of NV centers when the magnetic field is aligned along one of the four possible NV quantization axes. (a) Field dependence of the transition frequencies. For aligned NVs, the frequency dependence on the field is linear (black lines). The resonance frequencies of the remaining NVs are degenerate as they experience the same magnitude of the field projection on their quantization direction (grey lines). (b) ODMR spectrum (grey dots) and fit (red line) for an ensemble of NVs. The dips in the intensity of the PL signal appear as peaks in the lock-in detected PL signal. The external magnetic field components with respect to the aligned NV centers are $B_\parallel = 14.6\,\mathrm{mT}$ and $B_\perp = 1.1\,\mathrm{mT}$, corresponding to a field misalignment of $\theta = 4°$.

In a real experiment there will be a small misalignment between the external field and the NV center axis. To calculate the parallel ($B_\parallel$) and perpendicular ($B_\perp$) components of the field, we can rewrite Eq. 3.1 as $\hat{\mathscr{H}} = D\hat{S}_z^2 + \gamma B_\parallel \hat{S}_z + \gamma B_\perp \hat{S}_x$. Using Eq. 3.4 and solving for the field components, we find [83]:

$$B_\parallel = \frac{\sqrt{-(D+\omega_+ - 2\omega_-)(D+\omega_- - 2\omega_+)(D+\omega_+ + \omega_-)}}{3\gamma\sqrt{3D}}, \tag{3.7}$$

$$B_\perp = \frac{\sqrt{-(2D-\omega_+ - \omega_-)(2D-\omega_+ + 2\omega_-)(2D-\omega_- + 2\omega_+)}}{3\gamma\sqrt{3D}}. \tag{3.8}$$

The angle between the NV axis and the magnetic field can then be calculated by $\theta = \arctan(B_\perp / B_\parallel)$. A typical ODMR spectrum of an ensemble of NVs with the external magnetic field approximately aligned along one of the four possible NV quantization axes is shown in Fig. 3.5b. Since the PL signal is detected by a lock-in amplifier the dips in the intensity of the PL signal appear as peaks in the lock-in detected signal. The lock-in amplifier only detects signals that vary with a reference frequency. In our case, the MW frequency is modulated by a reference frequency in the MHz range. Therefore, if the MW is in resonance with an NV transition, the lock-in detects a signal, resulting in a peak. By fitting the PL signal with eight Lorentzians simultaneously, we obtain the resonance frequencies of the transitions. Using Eqs. 3.7 and 3.8, we find $B_\parallel = 14.6\,\mathrm{mT}$ and $B_\perp = 1.1\,\mathrm{mT}$, with respect to the aligned NV centers, corresponding to a field misalignment of $\theta = 4°$.

3.4. DETECTION OF AC FIELDS

In this section, we discuss the effect of an oscillating magnetic field on the NV center. We begin by simplifying the three-level NV Hamiltonian into a two-level Hamiltonian and establish the Bloch sphere representation of its wave function. By transforming the Hamiltonian into a rotating reference frame, following [70], we show that the two NV ESR transitions are driven by circularly-polarized magnetic fields with opposite handedness. Finally, we discuss the coherent spin state precession of the NV center due to the ac-field, referred to Rabi oscillation, as well as decoherence effects, resulting in a reduced life time of the coherent spin state.

3.4.1. BLOCH SPHERE

As a transition between the states $m_s = \pm|1\rangle$ is dipole-forbidden, we can treat the three-level system of the NV center, aligned with the z axis and described be Eq. 3.1, as an effective two-level system consisting of two orthogonal states $|0\rangle = |z+\rangle$ and $|1\rangle = |z-\rangle$, representing either the pair of states $\{|0\rangle, |1\rangle\}$ or $\{|0\rangle, |-1\rangle\}$. Consequently, the Pauli spin operators $S_{x,y,z}$ can be reduced to the Pauli matrices

$$\hat{\sigma}_x = \begin{pmatrix} 0 & 1 \\ 1 & 0 \end{pmatrix}, \quad \hat{\sigma}_y = \begin{pmatrix} 0 & -i \\ i & 0 \end{pmatrix}, \quad \hat{\sigma}_z = \begin{pmatrix} 1 & 0 \\ 0 & -1 \end{pmatrix}, \tag{3.9}$$

with $|0\rangle$ and $|1\rangle$ being eigenstates of $\hat{\sigma}_z$ with eigenvalues 1 and -1, respectively. The wave function $|\psi\rangle$ of a two level system can be expressed as the superposition of the states $|0\rangle$ and $|1\rangle$ given by [99]

$$|\psi\rangle = \cos\left(\frac{\theta}{2}\right)|0\rangle + \sin\left(\frac{\theta}{2}\right)e^{i\phi}|1\rangle\,. \tag{3.10}$$

Setting $0 \le \theta \le \pi$ and $0 \le \phi < 2\pi$, we obtain all possible states. The absolute squares of the coefficients of $|\psi\rangle$ can be interpreted as probabilities, summing up to one. The coefficient associated with $|0\rangle$ is constrained to real values to eliminate the physically non-existent degree of freedom represented by a common complex phase of both components. A geometrical representation of $|\psi\rangle$ is given by the Bloch sphere shown in Fig. 3.6.

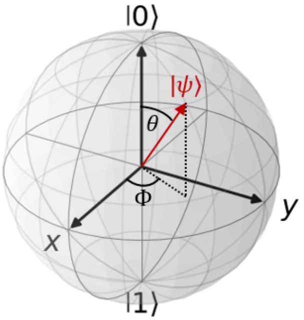

Figure 3.6.: In a two-level system the wave vector $|\psi\rangle$ can be represented as a superposition of the $|0\rangle$ and $|1\rangle$ states, with coefficients determined by the angles θ and ϕ.

3.4.2. ROTATING FRAME

To account for oscillating magnetic fields, we rewrite the three-level system Hamiltonian given in Eq. 3.3 as a two-level system Hamiltonian by selecting the upper-left or bottom-right corners of the matrix given in Eq. 3.3

$$\hat{\mathscr{H}}_\pm = \frac{\omega_\pm}{2}(\mathbb{1} \pm \hat{\sigma}_z) + \frac{\gamma}{\sqrt{2}}(B_x\hat{\sigma}_x + B_y\hat{\sigma}_y) = \hat{\mathscr{H}}_0 + \hat{\mathscr{H}}_{\text{ac}}, \tag{3.11}$$

where $\mathbb{1}$ is the identity matrix. Furthermore, to discuss the time evolution of the two-level system, we transform the Hamiltonian into a rotating frame, oscillating at frequency ω. We define a rotating wave function as $|\psi_R\rangle_\pm = \hat{U}_\pm|\psi\rangle$, with $\hat{U}_\pm = e^{\pm\frac{i\omega t}{2}\hat{\sigma}_z}$. To obtain the time evolution of $|\psi_R\rangle_\pm$, we use the time-dependent Schrödinger's equation $i\frac{\partial|\psi\rangle}{\partial t} = \frac{1}{h}\hat{H}|\psi\rangle = \hat{\mathscr{H}}|\psi\rangle$, which yields

$$\frac{\partial|\psi\rangle}{\partial t} = \frac{\partial}{\partial t}\left(\hat{U}_\pm^\dagger|\psi_R\rangle_\pm\right) = \hat{U}_\pm^\dagger\frac{\partial|\psi_R\rangle_\pm}{\partial t} \mp i\omega\frac{\hat{\sigma}_z}{2}\hat{U}_\pm^\dagger|\psi_R\rangle_\pm = -i\hat{\mathscr{H}}\hat{U}_\pm^\dagger|\psi_R\rangle_\pm . \tag{3.12}$$

Rewriting this, we can derive the Schrödinger equation for the rotating wave function

$$\frac{\partial|\psi_R\rangle_\pm}{\partial t} = -i(\hat{U}_\pm\hat{\mathscr{H}}_\pm\hat{U}_\pm^\dagger \mp \omega\frac{\hat{\sigma}_z}{2})|\psi_R\rangle_\pm = -i\hat{\mathscr{H}}_{\pm R}|\psi_R\rangle_\pm , \tag{3.13}$$

with the new Hamiltonian in the rotating frame

$$\hat{\mathscr{H}}_{\pm R} = \hat{U}_\pm\mathscr{H}_\pm\hat{U}_\pm^\dagger \mp \omega\frac{\hat{\sigma}_z}{2}. \tag{3.14}$$

The oscillating field $\mathbf{B_{ac}}$ can generally be elliptically polarized, which can be represented as the sum of two counter-rotating circular components of amplitude B_R and B'_R. Thus,

$\hat{\mathscr{H}}_{\text{ac}}$ is given by

$$\hat{\mathscr{H}}_{\text{ac}} = \frac{\gamma}{2\sqrt{2}} B_R(\cos(\omega t)\hat{\sigma}_x + \sin(\omega t)\hat{\sigma}_y) + \frac{\gamma}{2\sqrt{2}} B'_R(\cos(\omega t)\hat{\sigma}_x - \sin(\omega t)\hat{\sigma}_y) \tag{3.15}$$

$$= \frac{\gamma}{2\sqrt{2}} \cos(\omega t)\hat{\sigma}_x(B_R + B'_R) + \frac{\gamma}{2\sqrt{2}} \sin(\omega t)\hat{\sigma}_y(B_R - B'_R). \tag{3.16}$$

By transforming the two-level Hamiltonian in the rotating frame by using Eq. 3.11 and Eq. 3.14 and calculating the matrix products, we find

$$\hat{\mathscr{H}}_{+R} = \frac{\omega_+}{2}\mathbb{1} + \frac{1}{2\sqrt{2}}\gamma B_R \hat{\sigma}_x + \frac{1}{2\sqrt{2}}\gamma B'_R\big(\hat{\sigma}_x \cos(2\omega t) - \hat{\sigma}_y \sin(2\omega t)\big) - \frac{\Delta_+}{2}\hat{\sigma}_z, \tag{3.17}$$

$$\hat{\mathscr{H}}_{-R} = \frac{\omega_-}{2}\mathbb{1} + \frac{1}{2\sqrt{2}}\gamma B'_R \hat{\sigma}_x + \frac{1}{2\sqrt{2}}\gamma B_R\big(\hat{\sigma}_x \cos(2\omega t) + \hat{\sigma}_y \sin(2\omega t)\big) + \frac{\Delta_-}{2}\hat{\sigma}_z, \tag{3.18}$$

with the detuning $\Delta_\pm = \omega - \omega_\pm$ between the NV transition and the drive field $\mathbf{B_{ac}}$. In the Eqs. 3.17 and 3.18, the terms oscillating fast at $2\omega t$ can be dropped, as they will average to zero [100]. These equations show that the NV transitions are driven by circularly-polarized magnetic fields of opposite handedness. Thus, we find that the spin dynamics in the rotating frame picture is driven by the constant fields $B_{R,R'}$. In the following section, we will calculate the frequency at which the spin population is oscillating.

3.4.3. RABI OSCILLATIONS

Using a Rabi sequence offers an approach to sense magnetic fields oscillating near GHz frequencies. The NV spin state is first initialized in the $|0\rangle$ ground state by using green laser light. After initialization an oscillating magnetic field $\mathbf{B_{ac}}$ is applied for varying times. If the drive field is in resonance with the NV spin state transition, the spin population oscillates between these spin states. The frequency Ω_R at which the NV is driven is proportional to the strength of $\mathbf{B_{ac}}$, as depicted in Fig. 3.7a, and scales with the square root of the microwave power [101]. It is referred to as Rabi frequency. To calculate Ω_R we use Eq. 3.4 and find [70, 102] $\Omega_\pm = \sqrt{\Omega_R^2 + \Delta_\pm^2}$, with the Rabi frequency

$$\Omega_{R,R'} = \gamma B_{R,R'}/\sqrt{2}. \tag{3.19}$$

3.4.4. T_1 RELAXOMETRY

Another way to detect ac magnetic fields in the GHz frequency range, is to measure the longitudinal, or spin-lattice, relaxation time T_1 of the NV center, as the presence of magnetic noise at the resonance frequency of the NV center spin transitions reduces its spin lifetime. When the NV center is initially polarized into the $|0\rangle$ or $\pm|1\rangle$ ground state using green light, T_1 represents the characteristic time during which the spin population returns to a thermally mixed state. It can extend up to 6 ms, especially when dominated by phonon interactions at room temperature [101, 103]. However, the presence of magnetic frequency noise or other paramagnetic spins at the NV resonance frequency can decrease T_1, as shown in Fig. 3.7b. To determine T_1, the evolution time τ between the

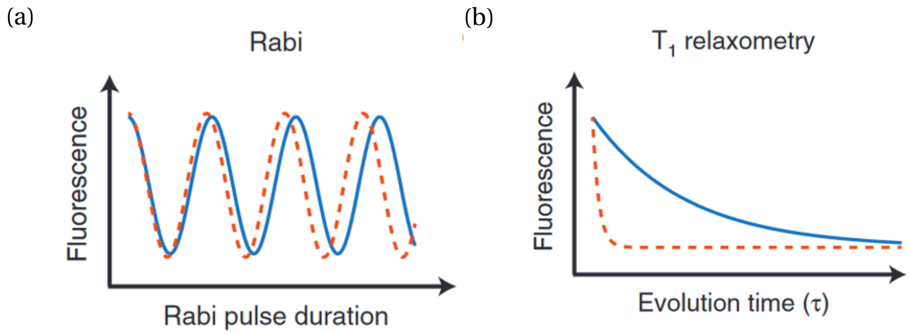

Figure 3.7.: Detection of ac magnetic fields. (a) Rabi oscillations: A higher amplitude of the microwave field results in an increased Rabi frequency (red curve). (b) T_1 relaxometry: The phonon-limited T_1 decay rate (blue curve) is amplified by high-frequency magnetic noise near the NV resonance frequency (red curve). (Fig. adapted from [101].)

initialization and readout laser pulses is varied. T_1 can then be obtained from a fit to an exponential decay of the contrast of the photoluminescence signal [60, 104]

$$C(\tau) = C_0 \cdot \exp(-\tau/T_1). \tag{3.20}$$

3.5. IMAGING OF SPIN WAVES

In Section 2.7.1, we discussed that the stray field of a DE spin wave $B_{\text{sw}}(t)$ is either left- or right-handed circular polarized, depending on the propagation direction of the spin wave. Consequently, it will drive either ω_- or ω_+ transitions of the NV center, allowing us to detect spin waves via their magnetic stray field. However, we do not gain any information about the phase of the propagating spin wave, which is necessary to image individual spin wave fronts. To gain this phase sensitivity, a microwave field $B_{\text{mw}}(t)$ oscillating at the same frequency as $B_{\text{sw}}(t)$ needs to be superimposed on $B_{\text{sw}}(t)$. This superposition of the two ac-fields results in a standing wave pattern of the total magnetic field, that drives the NV ESR with a spatial periodicity equal to the spin wave wavelength [57].

3.5.1. STANDING WAVE MODEL

To phenomenologically model the resulting PL signal, we calculate the time-averaged magnitude of the perpendicular time-dependent magnetic field $< |B_{\text{tot}_\perp}| >_t$ relative to the NV axis, where $B_{\text{tot}_\perp}$ is given by

$$B_{\text{tot}_\perp}(t) = B_{\text{sw}}(t) + B_{\text{mw}}(t). \tag{3.21}$$

$B_{\text{sw}}(t)$ and $B_{\text{mw}}(t)$ are given in the Eqs. 2.40 and 2.41, respectively. Thereby, we take into account that ESR transitions can only be driven by rf-fields perpendicular to the NV quantization axis. Furthermore, we average over time, as we measure a time independent PL signal at a fixed position on the sample, which is proportional to the magnitude of the standing wave of the total perpendicular magnetic field.

4

EXPERIMENTAL TECHNIQUES

In this chapter, we will introduce sensing and imaging techniques relying on ensembles of NV centers, which were used to obtain the results of this thesis. Two common methods exist in far-field optical microscopy for imaging: confocal microscopy and widefield microscopy, as shown in Fig. 4.1.

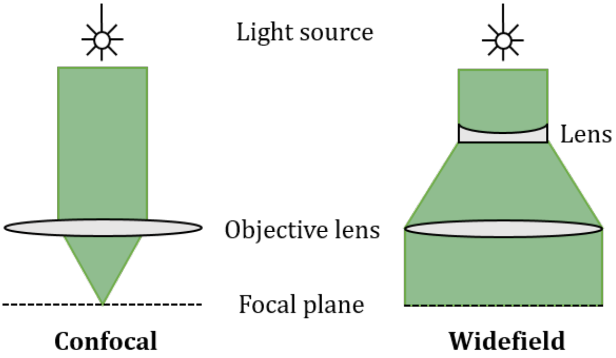

Figure 4.1.: Confocal vs widefield illumination. (a) In the confocal configuration, the light source is focused onto a diffraction-limited spot at the focal plane. To capture an image, the sample is scanned. (b) In the widefield configuration, the sample is uniformly illuminated by the light source, and the image is captured by a camera.

These techniques differ in the method of sample illumination and signal detection. In confocal microscopy, a high numerical aperture (NA) objective focuses the coherent light of a laser into a diffraction-limited spot. The measurement signal, for example, photoluminescence (PL), is collected by the same objective. Typically, an avalanche photodiode (APD) characterized by low dark current and efficient quantum yield at the single-photon level detects the signal. In confocal NV center microscopy, high spatial resolution can be attained through super-resolution techniques [105–107] or by using a single NV center instead of an ensemble of NV centers for imaging [108, 109]. Additionally, sensitivity to weak magnetic fields can be enhanced via lock-in amplified detection.

Nonetheless, a major drawback of confocal microscopy is the relatively slow measurement process, as scanning the sample point-by-point is necessary to obtain images over large areas.

In contrast, widefield imaging captures large areas by uniformly illuminating the entire sample. This is achieved by focusing the laser towards the back focal plane of the objective lens to generate a broad, parallel beam illuminating the sample completely. The resultant signal is recorded by a camera. Widefield fluorescence microscopy facilitates rapid imaging, which is the main benefit over confocal imaging.

During this work, three different NV center microscopes were assembled, each varying in its capabilities. In the following sections, we will explain their working principles and discuss the benefits of each method. We will start with a discussion of the spatial resolution of optical microscopes in Sec.4.1 and define the resolution limit according to Rayleigh's principle. In Sec.4.2, we will introduce a confocal NV center microscope acquiring data by lock-in amplified detection of the PL. We then continue in Sec.4.3 with the discussion of a confocal NV center setup that is integrated into a time-resolved MOKE setup. We finish this chapter in Sec.4.4 with the discussion of the implementation of a widefield NV center microscope.

4.1. SPACIAL RESOLUTION

In optical imaging, an important parameter is the resolution limit that can be achieved using a microscope. It is limited by diffraction, which occurs when light passes through any aperture. In our case, the aperture is the microscope's objective lens and the light source is a laser, as indicated in Fig. 4.2.

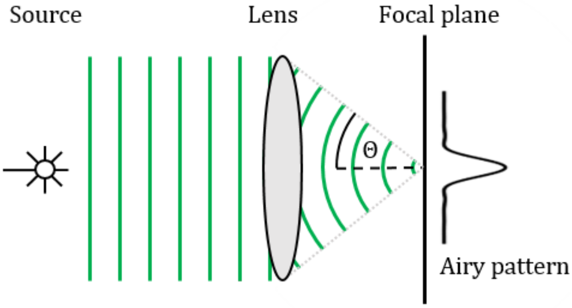

Figure 4.2.: Coherent laser light (green lines) passing through an objective lens is focused to a diffraction-limited spot, forming an Airy pattern at the focal plane. The spot size depends on the laser wavelength and the numerical aperture, which is determined by the medium's refractive index and the lens's maximum cone half-angle θ.

The minimal spot size that the laser can be focused down to depends on the wavelength λ of the laser light and the numerical aperture $\mathrm{NA} = \sin(\theta) \cdot n$ of the lens. Here, n

is the index of refraction of the medium in which the lens is working, in our case $n_{\text{air}} = 1$, and θ is the half-angle of the maximum cone of light that can enter or exit the lens. The resulting diffraction pattern, shown in Fig. 4.3a, is called the Airy pattern. It has radial symmetry and consists of a bright central circle called the Airy disc that contains 84% of the total light intensity. In Fig. 4.3b, the profile of the Airy pattern taken along the dashed red line in Fig. 4.3a is shown. The diameter of the Airy disc is defined as the distance between the first minima in the diffraction pattern, as indicated by the red vertical lines in Fig. 4.3b.

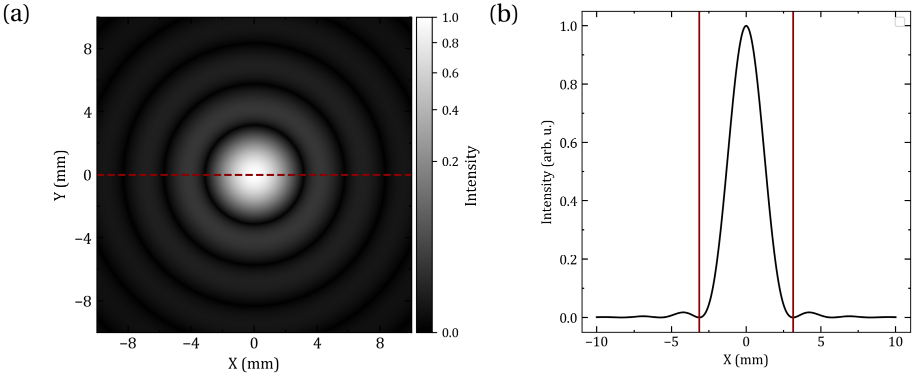

Figure 4.3.: (a) Airy pattern of a single light source. 84% of the total light intensity is contained in the central maximum of the Airy pattern referred to as the Airy disc. (b) Profile of the Airy pattern taken along the red dashed line in (a). The diameter of the Airy disc is indicated by the vertical red lines.

According to the Rayleigh criterion [110, 111], two light sources can still be resolved if the central maximum of the Airy pattern of the first light source lies on the first minimum in the diffraction pattern of the second light source. Thus, the lateral spatial resolution limit is defined by the Airy radius given by

$$r_{\text{Airy}} = \frac{0.61\lambda}{\text{NA}}. \tag{4.1}$$

In Fig. 4.4a, the Airy pattern of two light sources that can still be resolved according to the Rayleigh criterion is shown. Fig. 4.4b shows the profile of this Airy pattern taken along the dashed red line. The Airy radius is indicated by the red vertical lines.

4.2. Lock-In Amplified Confocal NV Center Microscopy

To achieve a high signal-to-noise ratio in our magnetometry measurements, we implemented a confocal NV center microscope that uses an APD as a PL detector in combination with a lock-in amplifier. The phase-sensitive lock-in amplifier operates by detecting signals precisely at a specified reference frequency, with the capability to narrow the

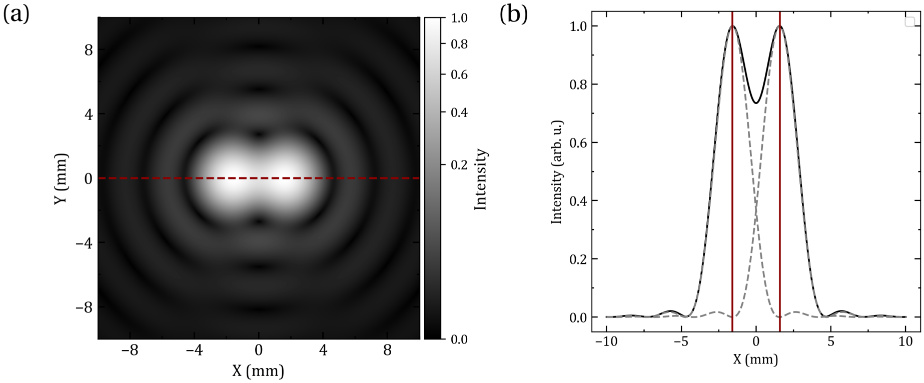

Figure 4.4.: (a) Airy pattern of two light sources that can still be resolved as the central maximum of the Airy pattern of the first light source lies on the first minimum in the diffraction pattern of the second light source. (b) Profile of the Airy pattern taken along the red dashed line in (a). The lateral spatial resolution limit defined by the Airy radius in Eq. 4.1 is indicated by the vertical red lines.

bandwidth down to 0.01 Hz, if desired [112, 113], while also capturing the phase relationship between the measured signal and the reference signal. When a signal is modulated at this reference frequency, the lock-in amplifier can effectively isolate it from background noise and signals at other frequencies or with different phase relation, resulting in a favorable signal-to-noise ratio. In NV center magnetometry experiments, where a MW source resonantly manipulates the spin states, the lock-in amplifier can isolate the spin signal by modulating the MW field's frequency at the reference frequency [112].

4.2.1. SETUP

A schematic of the setup is shown in Fig. 4.5. The NV centers are optically excited by a 515 nm laser (iBeam-smart-515s, Toptica), focused to a diffraction-limited spot by an objective with a numerical aperture of 0.9 and a magnification of 63. Using Eq. 4.1, the maximal achievable resolution is 350 nm. In front of the objective, a polarizer and a $\lambda/2$-plate are employed to rotate the polarization of the laser light. This allows to maximize the contrast in the $\omega_\pm$ transitions of NV centers aligned with an external bias field. Furthermore, a beam splitter splits the green excitation light, partially reflecting and partially transmitting it, while fully transmitting the red PL light, as indicated in Fig. 4.5. The transmitted green light is detected by an additional photodiode for imaging the topography of the sample. The NV PL is collected by the same objective, separated from the excitation light by a short-pass dichroic mirror (SP DM cut-off wavelength 600 nm, Edmund Optics) and a long-pass (LP) filter (cut-on wavelength 590 nm, Edmund Optics). A lens (L) in combination with a mirror (M) is used to focus the PL light on the avalanche photodiode (APD, Hamamatsu, S5344). Additionally, a blue light-emitting diode (LED), a camera, and a flip mirror (FM) are used for widefield illumination to provide a live image

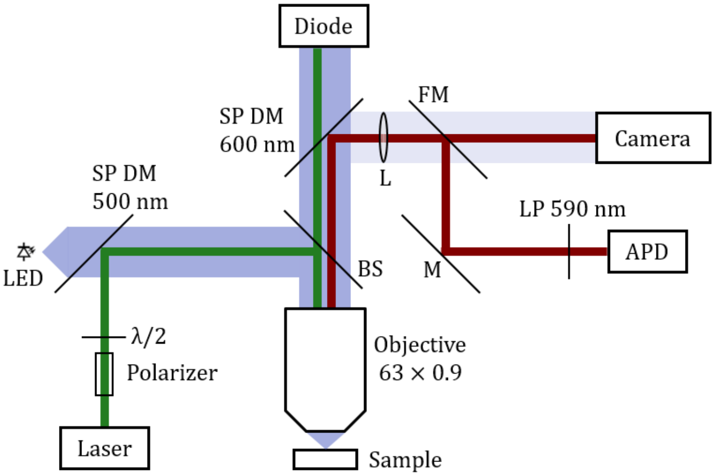

Figure 4.5.: Sketch of the optical setup. A green laser excites NV centers. A polarizer and $\lambda/2$-plate rotate the polarization of the green light. A beam splitter partially transmits and reflects the green light, allowing for detection of the topography image by a photodiode (diode). NV PL, separated from the green light by a dichroic short-pass mirror (SP DM 600 nm), passes a long-pass (LP) filter and is focused on an avalanche photodiode (APD) by a lens (L) and mirror (M). Blue light-emitting diode (LED) light, a camera, and a flip mirror (FM) are used for widefield illumination. A DM SP 500 nm couples the blue LED light into the green light beam path.

of the sample. The SP DM 600 nm transmits approximately 95% of the light with wavelengths below 600 nm. The small fraction of blue light that is still reflected by the SP DM 600 nm is sufficient to image the sample with the camera. During the PL measurements, the LED was always turned off. A SP DM 500 nm (cut-off wavelength 500 nm, Edmund Optics) couples the blue LED light into the green light beam path. For simplification, only the relevant path of the blue light is indicated in Fig. 4.5.

4.2.2. MEASUREMENT METHOD

Microwaves for driving the NVs were generated using a microwave generator (N5183A MXG, Agilent). To measure the PL signal with a lock-in amplifier (SR830, Stanford Research Systems), the microwave signal was modulated by a coaxial switch (139-ZASWA-2-50DRA, Mouser Electronics). The reference signal needed for modulation was generated by a function generator (SFG-2110, GW Instek). The PL signal detected by the APD passed through a voltage amplifier and was then measured by the lock-in amplifier. Each data point was measured for 1 s at the 3rd filter order. To acquire an image, the sample was scanned using a piezo stage (Tritor 102, Piezosystem Jena) on which the sample was mounted. The step size in such a scan determined the resolution of the image. Furthermore, an external bias field was applied by a permanent magnet mounted on a programmable translation stage. The stray field of the permanent magnet was aligned with an NV center axis. This setup was used for the spin wave experiments in Chapter 6.

4.3. COMBINED CONFOCAL NV CENTER / TR-MOKE MICROSCOPY

With the aim of imaging spin waves simultaneously using both NV based microscopy and time-resolved magneto-optical Kerr effect (TR-MOKE) microscopy, a setup combining both techniques was established. The implementation of this setup was carried out as part of a master's thesis project conducted by Lukas Colombo [114]. Before discussing the implementation of the setup, we will give an introduction to TR-MOKE microscopy.

4.3.1. TR-MOKE

Time-resolved scanning Kerr microscopy is commonly employed for investigating magnetization dynamics, particularly spin waves [115–119]. TR-MOKE operates as an optical pump-probe technique. In our configuration, the pump is a microwave generator used to excite coherent spin waves at frequency f_{pump} in the gigahertz (GHz) range. The probe is a pulsed laser with a repetition rate f_{probe} that maintains a constant phase relationship with respect to f_{pump}, fulfilling $f_{\text{pump}} = n \cdot f_{\text{probe}}$, where n is an integer. Using PMOKE, the out-of-plane (OOP) component of the magnetization is examined to capture a stroboscopic image of the spin wave. Since the duration of each laser pulse is significantly shorter than one period of the excitation, the magnetization is sampled at a distinct phase. Consequently, detecting the propagating spin wave over time at a single sample location yields a constant signal with a specific amplitude and phase, as indicated by the blue dots in Fig. 4.6. Scanning along the spin wave's propagation direction over the sample results in a signal oscillating at the spin wave's wavelength.

To overcome the constraint of probing spin waves only at frequencies that are multiples of the laser's repetition rate, a technique known as super-Nyquist sampling (SNS) MOKE can be employed [120]. In this approach, the pump frequency is tuned to any intermediate frequency $f_{\text{pump}} = n \cdot f_{\text{probe}} + f_{\text{dif}}$, where f_{dif} is set such that the pump frequency is not a multiple of the probe frequency. Since the magnetization precesses at $f_{\text{pump}} \neq n f_{\text{probe}}$, detecting the OOP component at a repetition rate f_{probe} results in an alias oscillating at $f_{\text{dif}} < f_{\text{probe}}$, as shown in Fig. 4.6. However, detecting the signal at a single spot with a lock-in amplifier locked to f_{dif} produces a constant signal with a specific phase and amplitude of the alias. Scanning over the sample along the propagation direction of the spin wave also resolves its wavelength in the SNS approach.

4.3.2. SETUP

The optical part of the combined NV center / TR-MOKE setup is shown in Fig. 4.7. The description of the setup follows [114]. In the TR-MOKE part, Fig. 4.7a, a pulsed 800 nm Ti:Sa-Laser (Mira 900, Coherent) is employed, which is first attenuated and polarized using a half-wave plate and a polarizer. The beam then passes through a pellicle beam splitter with 92% transmission. To combine the beams coming from the MOKE- and

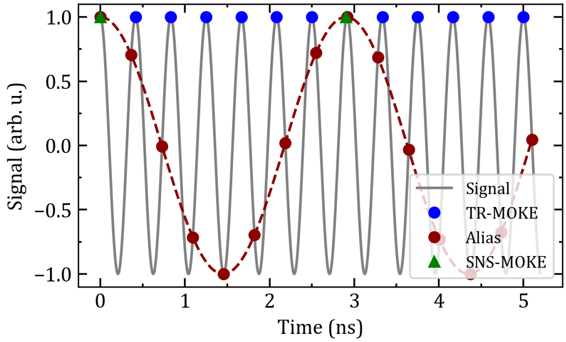

Figure 4.6.: TR-MOKE vs SNS-MOKE: A signal (gray line) oscillating at f_{pump} can be sampled with a frequency f_{probe} that is that is an integer fraction of f_{pump}, as done in TR-MOKE (blue points). Alternatively, it can be sampled with a frequency that satisfies $f_{\text{pump}} = n \cdot f_{\text{probe}} + f_{\text{dif}}$ (red dots), as done in SNS-MOKE, resulting in an alias of the signal (red dashed line). In that case, locking to the difference frequency f_{dif} (green dots) as well resolves the amplitude and phase of the signal.

NV-parts of the setup, a 750 nm LP DM is used. The beams are then sent to a galvo-galvo scanning system (LSKGG4/M, Thorlabs) and a telecentric lens system, enabling lateral movement of the beam with respect to the sample. The laser light is then focused by an objective with a numerical aperture of 0.7 and a magnification of 63 to a diffraction-limited spot with an Airy radius of 450 nm. A camera and blue LED are installed to acquire a live-image of the sample, as well as to optically stabilize the image with a piezo-stage below the sample. A Wollaston prism splits the returning beam into two linearly polarized components with perpendicular polarization orientation. Each beam is directed towards a differential detector with two photodiodes. A change in the magnetization of the sample results in a complementary change of the intensities of the beams, which provides the contrast in a measurement.

To keep the repetition rate of the laser constant, the laser's cavity length is actively adjusted to match the repetition rate with a global frequency reference by a control loop (PhaseLock, TEM). The control loop incorporates a photodiode, a mixer, and a proportional-integral-derivative (PID) controller. The photodiode detects the generated pulses. This signal is mixed with the reference signal to produce a down-converted signal for use by the PID controller. The reference signal, derived from a 10 MHz rubidium atomic clock (FS725, SRS), undergoes frequency multiplication to achieve the desired 80 MHz value. The 10 MHz reference signal is also utilized for an arbitrary waveform generator (AWG) (AWG70001A, Tektronix) producing MW signals for the spin wave excitation, as shown in Fig. 4.8. The output of the lock-in, which is the differential signal generated by the rotation in polarization and obtained by taking the difference of the outputs of the detectors, is referred to as the Kerr signal S_{Kerr}, while the summed signal of the two photodiodes is referred to as the topographic signal S_{Topo}.

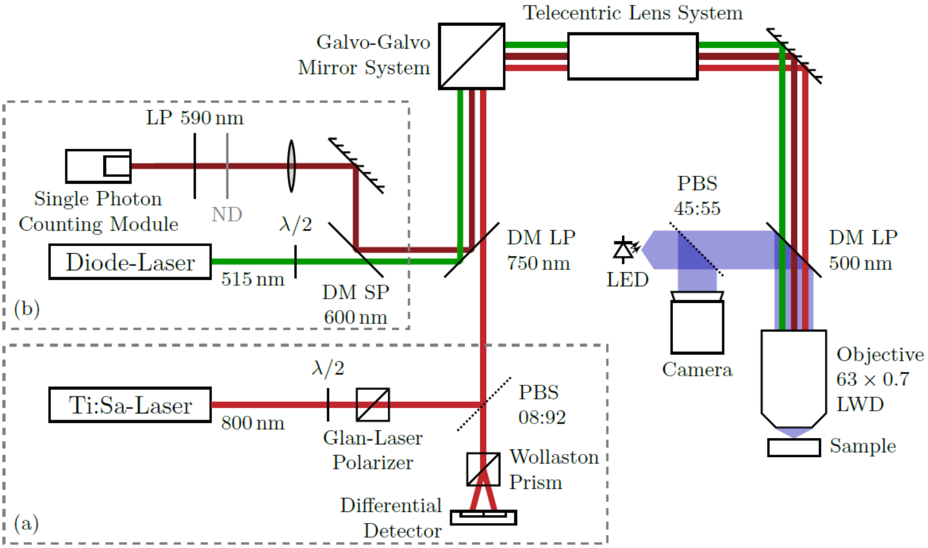

Figure 4.7.: Combined NV center / TR-MOKE setup using a Galvo-Galvo Mirror system in combination with a telecentric lens system to scan over the sample. A detailed description of all parts is given in Sec. 4.3.2. (a) Components of the TR-MOKE part. (b) Components of the NV part. Legend: DM: dichroic mirror. LP/SP: longpass/shortpass. PBS: pellicle beam splitter. ND: neutral-density filter. LWD: long working distance. Fig. adapted from [114].

In Fig. 4.7b the NV specific parts of the setup are shown. It uses a 515 nm diode-laser (06-MLD, Cobolt) to excite NV centers. A 600 nm SP DM is used to split the PL from the green laser light. After passing a neutral-density (ND) filter and a 590 nm LP filter, the PL is detected by a single photon count module (SPCM) (ARQH-14-TR, Excelitas). The ND filter is needed to attenuate the signal such that the SPCM is not saturated. Furthermore, a metal box encloses the SPCM in order to reduce the photon background further. A permanent magnet mounted on a translation stage is used to generate a magnetic bias field.

4.3.3. SINGLE PHOTON DETECTION

The PL signal is measured using an SPCM, which outputs a single voltage pulse for every detected photon. A time-to-digital converter (TDC) (Time Tagger 20, Swabian Instruments) is used to count these voltage pulses. This is done by using a trigger assigned to a start time t_{start}. Additionally, a time interval Δt is defined during which the pulses are measured with respect to t_{start}, such that the counting stops at $t_{\mathrm{end}} = t_{\mathrm{start}} + \Delta t$. The TDC assignes a timestamp t_{pulse} to each pulse from the SPCM. The number of pulses is counted as long as $t_{\mathrm{start}} < t_{\mathrm{pulse}} < t_{\mathrm{end}}$. This sequence is repeated and the counts are summed up according to their time stamp until enough photons are counted to achieve

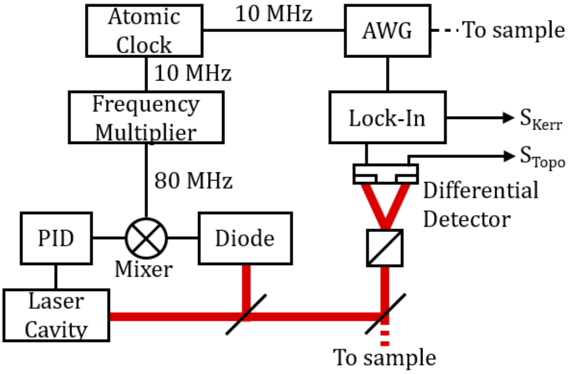

Figure 4.8.: Components of the TR-MOKE setup. An atomic clock generates a 10 MHz reference signal used for the stabilization of the laser cavity through a phase-locked loop (PLL) as well as for the synchronization of the pulsed laser and AWG. The PLL consists of a photodiode detecting the laser pulses, a proportional-integral-derivative (PID) controller connected to the laser cavity, and a mixer. A differential detector acquires the signal. The differential signal S_{Kerr} is measured by a lock-in amplifier, resulting in the Kerr signal S_{Kerr}. The sum signal S_{Sum} detects the topography of the sample.

a reasonable signal.

A programmable, multi-channel pulse generator (PBESR-PRO-500-PCI, SpinCore) is used to generate the trigger signals. The pulse generator is also used to control the laser and the MW signal. Furthermore, the MW generator is connected to a programmable attenuator, an amplifier with a fixed amplification of roughly 20 dBm, and a high-speed, solid-state switch (ZASWA-2-50DRA+, Mini-Circuits) that is connected to one channel of the pulse generator.

4.4. WIDEFIELD NV CENTER MICROSCOPY

In this section, we describe a widefield NV center microscope, which was built with the aim of fast data acquisition. The implementation of this setup was carried out as part of a master's thesis project conducted by Ankita Nayak [121]. In the following, we will first introduce the setup and then discuss how the measurement data was processed.

4.4.1. SETUP

For optical excitation of an ensemble of NV centers, a 532nm green laser (L1C-532S, Oxxius) was used. A polarizer in combination with a $\lambda/2$-plate adjusted the polarization direction of the linearly polarized green light. The collimated beam was then expanded by a lens and focused into the back focal plane of the objective lens to generate a broad beam illuminating the sample over a wide area, as schematically shown in Fig. 4.9. A removable LP DM with a cutoff wavelength of 590 nm separated the green laser light from the red PL. The PL was then recorded by a scientific camera (Prime BSI, Teledyne Photometrics). If the LP DM was removed, the green laser light together with the PL light was recorded by the camera. A microwave generator (SynthHD (v2), Windfreak) in combination with an amplifier were used to drive the NV spin state transitions, and a permanent magnet mounted on a translation stage and oriented along one of the NV axes was installed to generate a bias field.

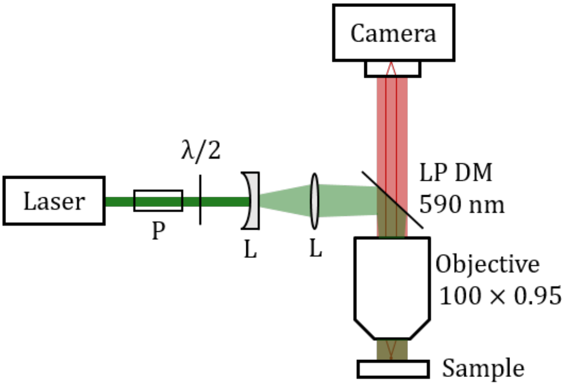

Figure 4.9.: Optical setup of the widefield NV center microscope. NV center excitation is achieved using a 532 nm green laser. Polarization adjustment is performed by a polarizer (P) and a $\lambda/2$-plate. The collimated beam is expanded by a lens (L). A removable 590 nm long pass dichroic mirror (LP DM) separates the green laser from the red PL, which is captured by a camera.

4.4.2. DATA COLLECTION

To collect data with the widefield setup, the camera captures an image during a specified exposure time. To measure an ODMR signal in N frequency steps, N images are acquired. To enhance the signal-to-noise ratio, this measurement sequence is repeated M times and that data is averaged, as depicted in Fig. 4.10a. For background correction, an image at a reference frequency far away from the ODMR dips is taken immediately after the signal image is captured, resulting in a total of $2 \times N \times M$ recorded frames.

To analyze the collected data, the acquired images are divided into a grid of X and Y pixels, as illustrated at the top of Fig.4.10b. The minimal pixel size is limited by Rayleigh's criterion given in Eq. 4.1. However, if maximal image resolution is not crucial, the signal-to-noise ratio is improved by averaging the signal over multiple pixels. In the top figure of Fig.4.10b, the signal stays constant over the area indicated by the red square, which allows for averaging over this area. Finally, the averaged data of the readout area is plotted, as shown at the bottom of Fig.4.10b.

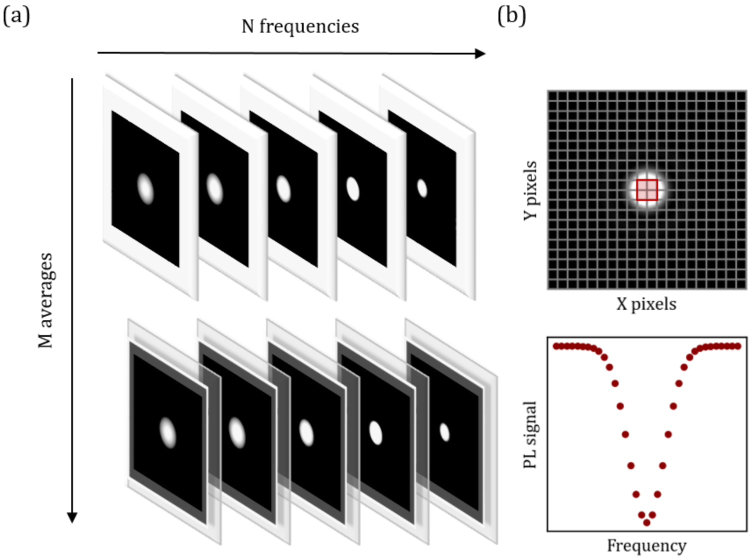

Figure 4.10.: Measurement principle of the widefield setup. (a) For experiments dependent on N frequencies, N frames are recorded. To enhance the signal-to-noise ratio, the sequence is repeated M times and averaged. (b) Top: Each frame is divided into a grid of pixels. The red rectangle, consisting of four minimal-sized pixels, represents an area where the signal remains constant. Bottom: Signal comprising N data points obtained by averaging the signal of each frame over a specified number of pixels (red rectangle in the top figure) and over the M repeated frames.

5

DIAMOND CHARACTERIZATION

In this chapter, we present the characterization measurements of the diamonds used in this thesis. We begin by introducing the parameters of the diamond substrate in Sec. 5.1. Following this, we discuss the dependence of the photoluminescence (PL) signal on the microwave power through optically detected magnetic resonance (ODMR) measurements. In Sec. 5.2, we determine the magnitude of an external bias field. Furthermore, by changing the polarization direction of the excitation laser light, we tune the ODMR contrast in the PL signal. The measurements in these sections are all conducted with the Lock-in setup presented in Sec. 4.2. We then demonstrate coherent NV center measurements in Sec. 5.3. These measurements were conducted as part of a master's thesis by Lukas Colombo [114] using the setup described in Sec. 4.3.2. We first discuss our results on the lifetime measurements of the NV states, followed by AC magnetic field sensing experiments, where we demonstrate the dependence of the Rabi frequency on the strength of the driving field. We close this chapter with a short summary in Sec. 5.4.

5.1. INITIAL MEASUREMENTS

5.1.1. SAMPLES

The diamond samples used in this thesis were fabricated from 2 mm × 2 mm type IIa single-crystal diamond plates grown by chemical vapour deposition (CVD). They had a thickness of 100 μm, Nitrogen content < 1 ppm, surface roughness < 2 nm Ra, and were (100)-oriented (purchased from Applied Diamond). These diamonds where implanted with $^{15}N^{+}$ ions at an energy of 4 keV, a dose of 1.2×10^{13} ions/cm^2, and a tilt angle of 7° (performed by CuttingEdge Ions). This corresponds to a implantation depth of 6.4 nm with a longitudinal straggling of 2.6 nm. Subsequently, marks were etched on the surface adjacent to the NV layer to facilitate its identification when observed under a microscope (conducted by MiDiaTec). Following this, the samples underwent annealing in a vacuum environment of $\sim 10^{-6}$ mbar. The annealing process involved a 45-minute ramp to 900°C, followed by 3 hours at (900 ± 10)°C and a 2 h ramp to room temperature, as shown in Fig. 5.1a.

To remove the graphitic layer that formed during the annealing, the samples were acid cleaned during 4 h by a boiling 3-acid mix consisting of 3 ml sulfuric acid (H_2SO_4), 3 ml nitric acid (HNO_3), and 3 ml perchloric acid ($HClO_4$). Finally, one diamond chip was

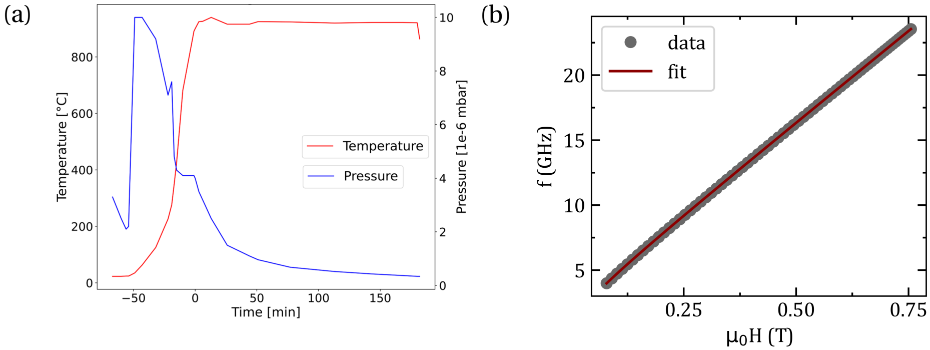

Figure 5.1.: (a) Temperature (red) and pressure (blue) profile during the annealing process of the diamond substrates. (b) FMR resonance frequencies (grey dots) of the 110 nm thick YIG thin film in dependence of the external magnetic field. The data was fitted with Eq. 2.35 (red line), resulting in a saturation magnetization of $\mu_0 M_S = 180$ mT.

then laser cut into pieces of 1 mm × 1 mm, 0.5 mm × 1 mm, and 0.5 mm × 0.5 mm (conducted by MiDiaTec). The purpose of the small surface area of these diamond pieces was to reduce the distance between the sample and the NV centers, as there was a lower chance of dirt being trapped between the sample and the diamond. The diamond chip was then placed on the sample to be measured, with the NV centers facing the sample surface.

The following results were measured on a Silicon substrate and two YIG substrates. The YIG samples were fabricated with the intention to measure spin waves as presented in Chapter 6. In this chapter however, both samples were used to drive the NV centers for first characterization measurements. The first sample was a Silicon (Si) substrate with two parallel microstrip lines fabricated on its surface by optical lithography and electron beam evaporation. The microstrip lines consisted of a 5 nm thick titanium buffer layer, which increased the adhesion to the Si substrate, and a 100 nm gold layer. The widths of the microstrip lines were $d_1 = 8$ µm and $d_2 = 5$ µm.

The YIG samples were a 110 nm and a 200 nm thick YIG thin film grown on a gadolinium gallium garnet substrate via liquid phase epitaxy. The 110 nm thin film possesses a saturation magnetization $\mu_0 M_S = 180$ mT, as determined from fitting the FMR measurements shown in Fig. 5.1b to Eq. 2.35. The 200 nm thick YIG thin film possesses a saturation magnetization $\mu_0 M_S = 185$ mT, as determined in Chapter 6. Similar to the Si substrate, microstrip lines for NV center excitation were fabricated on the YIG films using optical lithography and electron beam evaporation. Additionally, gold rectangles were fabricated on the YIG surface, which were not utilized in the experiments of this chapter. Perpendicular to these microstrip lines, Ti (5nm)/Au (200nm) modulation microstrip lines of varying widths, separated from the excitation microstrip lines by a 150 nm thick SiO_2 layer (red), were fabricated using the same techniques. Although not employed in the subsequent experiments, these modulation microstrip lines increased the distance between the NV centers and the sample surface. The excitation microstrip lines have the

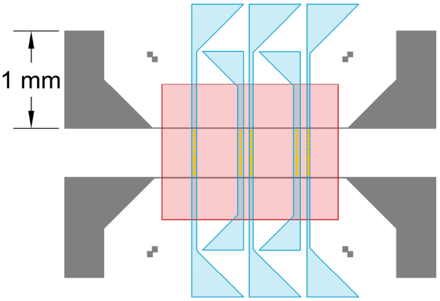

Figure 5.2.: Sample design, consisting of two excitation microstrip lines (grey), an insulating SiO_2 layer (red), modulation microstrip lines (blue), and gold squares fabricated directly on the sample surface.

same dimensions in both the Si and the YIG sample. A sketch of the samples design is shown in Fig. 5.2.

5.1.2. OPTICALLY DETECTED MAGNETIC RESONANCE

ODMR spectroscopy is the optical detection of resonance lines, which is based on the linear relation between the resonance frequency of the electron spin and the static external magnetic field. In continuous-wave-ODMR (cw-ODMR), the NV center is continuously irradiated with green laser light, resulting in a spin polarization of the NVs into the $m_S = |0\rangle$ ground state. At the same time, a MW field in the GHz range is applied. Its frequency is varied and the PL signal is detected. If the MW frequency hits the resonance frequency of the NV center, spin transitions occur into the $m_S = \pm|1\rangle$ states, which result in a decreased PL signal at the resonance frequency. At room temperature and without the application of an external magnetic field, the NV resonance frequency lies at 2.87 GHz, as shown in Fig. 5.3.

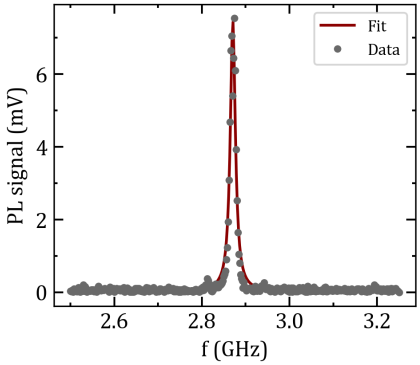

Figure 5.3.: ODMR spectrum (grey dots) of an ensemble of NVs showing a zero-field dip at 2.87 GHz, as determined by the Lorentzian fit to the data (red line).

5.1.3. MICROWAVE POWER DEPENDENCE

In the following, we investigate how the zero-field PL signal in cw-ODMR measurements depends on the MW power used to drive the NV transitions. To that end, the zero field dip (ZFD) of the ensemble of NVs was measured for MW power levels from -10 dBm to 14 dBm, as shown in Fig. 5.4.

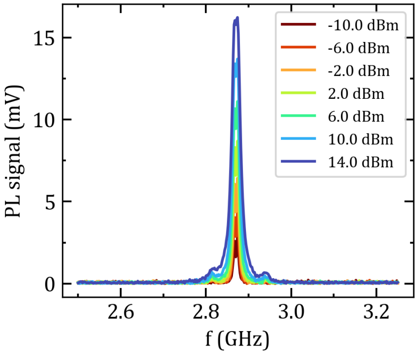

Figure 5.4.: Dependence of the zero field ODMR dip on the MW power. At high MW power levels the linewidth of the signal increases due to inhomogenous line broadening.

For a quantitative analysis, the ODMR signal I was fitted by a Lorentzian for each MW power using the equation

$$I = A\frac{\Delta f^2}{(f-f_0)^2+\Delta f^2}, \tag{5.1}$$

where A is the ODMR peak amplitude, Δf the linewidth, and f_0 the resonance frequency.

The extracted amplitude and linewidth of these fits are presented in Figs. 5.5a and 5.5b. We find that with increasing MW field strength, the amplitude of the ZFD increases. Furthermore, the linewidth also increases with increasing MW field strength. The ODMR linewidth is primarily determined by the inhomogeneous dephasing rate Γ_2^* of the NV electron spin, influenced by magnetic interactions with spin impurities in the diamond matrix. In high-purity CVD-grown diamonds, these impurities are mainly ^{13}C nuclear spins. The fluctuating magnetic field from these spins causes a Gaussian distribution of the effective field. Furthermore, power broadening from laser light and microwave fields also affects the linewidth [122]. Reducing MW power narrows the linewidth but decreases ESR signal amplitude. In the following measurements an MW power of 10 dBm was used. A more precise determination of the most suitable MW power level would require measuring a single transition by applying a bias field and accounting for hyperfine splitting.

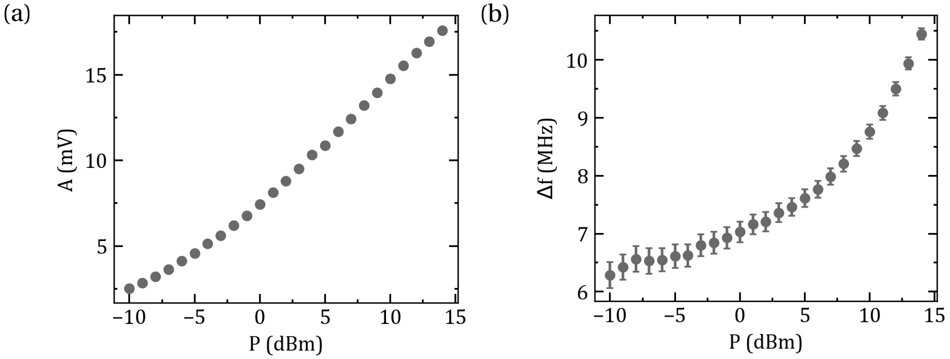

Figure 5.5.: (a) ODMR amplitude as a function of the applied MW power. (b) ODMR linewidth dependence on the MW power. The linewidth increases for stronger MW fields due to power broadening.

5.2. STATIC MAGNETIC FIELD SENSING

In magnetometry measurements a bias field is usually applied to gain a higher field sensitivity, as the zero field splitting due to strain in the diamond matrix as well as the degeneracy in the energy levels is lifted, resulting in a sharper linewidth of the resonances. In the following, we use ODMR measurements to detect NV transitions in the presence of a static external magnetic field. We define our coordinate system such, that the (100)-oriented diamond chip lies in the xy-plane, with the normal of the chip surface aligned parallel to the z-axis. One NV center, $\mathbf{NV_1}$, lies in the xz-plane. The polar angle between the $\mathbf{NV_1}$ direction and the z-axis is 55°. Furthermore, an external field $\mathbf{B_{ext}}$ is applied at a polar angle $\theta = 55°$ relative to the z-axis and an azimuthal angle $\phi = 15°$ relative to the x-axis. The orientation of the external field and the four NV center directions are depicted in Fig. 5.6. $\mathbf{NV_1}$, $\mathbf{NV_2}$, and $\mathbf{B_{ext}}$ all lie on the surface of a cone with an opening angle of 55°, as indicated by the grey points in Fig. 5.6. $\mathbf{NV_3}$ and $\mathbf{NV_4}$ on the other hand lie on the surface of the cone with an angle of 135° between its surface and the z-axis, indicated by the grey squares in Fig. 5.6. In this coordinate system the NV directions are given by

$$\mathbf{NV_{1,2,3,4}} = \begin{pmatrix} \sin(55°) \\ 0 \\ \cos(55°) \end{pmatrix}, \begin{pmatrix} -\sin(55°) \\ 0 \\ \cos(55°) \end{pmatrix}, \begin{pmatrix} 0 \\ \sin(55°) \\ -\cos(55°) \end{pmatrix}, \begin{pmatrix} 0 \\ -\sin(55°) \\ -\cos(55°) \end{pmatrix}. \tag{5.2}$$

Furthermore, the magnetic field vector $\mathbf{B}_{\text{ext}}$ is given by

$$\mathbf{B}_{\text{ext}} = B_{\text{mag}} \cdot \begin{pmatrix} \sin(\theta)\cos(\phi) \\ \sin(\theta)\sin(\phi) \\ \cos(\theta) \end{pmatrix}. \tag{5.3}$$

The parallel and perpendicular projections of $\mathbf{B}_{\mathrm{ext}}$ on the four NV directions can be calculated by

$$\begin{aligned} B_{\mathrm{ext}\|_{i},s} &= |(\mathbf{B}_{\mathrm{ext}} \cdot \mathbf{NV}_{i})\mathbf{NV}_{i}| := |\mathbf{B}_{\mathrm{ext}\|_{\mathbf{i},\mathbf{s}}}|, \\ B_{\mathrm{ext}\perp_{i},s} &= |\mathbf{B}_{\mathrm{ext}} - \mathbf{B}_{\mathbf{ext}\|_{\mathbf{i},\mathbf{s}}}|. \end{aligned} \tag{5.4}$$

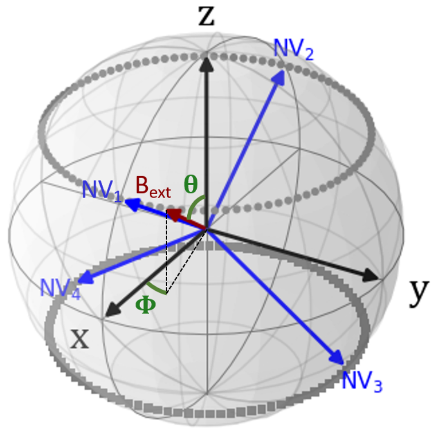

Figure 5.6.: Illustration of the NV center orientations $\mathbf{NV_1}$, $\mathbf{NV_2}$, $\mathbf{NV_3}$, $\mathbf{NV_4}$ and the external field direction $\mathbf{B}_{\mathrm{ext}}$. $\mathbf{NV_1}$ lies in the xz-plane, with a polar angle of 55° relative to the z-axis. The external magnetic field $\mathbf{B_{ext}}$ is applied at a polar angle $\theta = 55°$ relative to the z-axis and an azimuthal angle $\phi = 15°$ relative to the x-axis. $\mathbf{NV_1}$, $\mathbf{NV_2}$, and $\mathbf{B_{ext}}$ lie on the surface of a cone with an opening angle of 55°, as shown by the grey points. $\mathbf{NV_3}$ and $\mathbf{NV_4}$ lie on the surface of a cone with an angle of 135° between its surface and the z-axis, indicated by the grey squares.

5.2.1. MAGNETIC FIELD INDUCED SPLITTING

In Fig. 5.7a, the ODMR spectrum for this orientation of the external magnetic field is shown. As the projection of this field on the NV center axes has not the same magnitude, a total of eight distinguishable peaks is measured. To determine the field strength of the applied bias field, the ODMR spectrum is fitted by eight Lorentzian peaks. The fit result is indicated as the red line in Fig. 5.7a.

Using Eqs. 3.7 and 3.8, as well as the fitted resonance frequencies, we calculate the parallel ($B_{\mathrm{ext}\|,m}$) and perpendicular ($B_{\mathrm{ext}\perp,m}$) projections of the external field on the four NV directions. From these projections we can determine the external field magnitude by

$$B_{\mathrm{mag}} = \sqrt{B^2_{\mathrm{ext}\|,m} + B^2_{\mathrm{ext}\perp,m}}. \tag{5.5}$$

The obtained values are listed in Table 5.1. Averaging over all calculated magnitudes re-

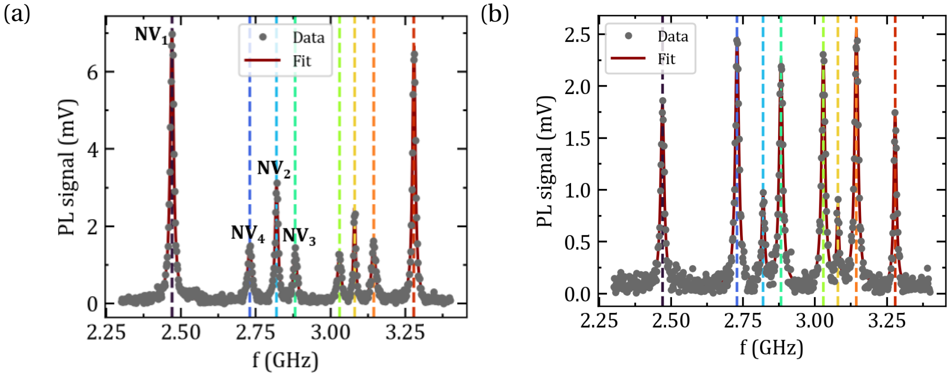

Figure 5.7.: ODMR spectrum of an NV ensemble with the magnetic field aligned along a polar angle $\theta = 55°$ relative to the z-axis and an azimuthal angle $\phi = 15°$ relative to the x-axis (See Fig.5.6). (a) Fitting the data with eight Lorentzians (red line) yields the resonance frequencies of each NV family $\mathbf{NV_i}$ located at the positions of the dashed lines. With the Eqs. 3.7, 3.8, and 5.5 we find $B_\text{mag} = (14.8 \pm 0.01)$ mT. (b) Varying the amplitudes of the ODMR peaks is achieved by rotating the polarization angle α of the laser light. The spectrum is fitted (red line) to gain the resonance frequencies of the eight peaks indicated by the dashed vertical lines.

sults in $B_\text{mag} = (14.8 \pm 0.01)$ mT. By using the NV vectors defined in Eq. 5.2, the external

	f_+ (GHz)	f_- (GHz)	$B_{\text{ext}\parallel,m}$ (mT)	$B_{\text{ext}\perp,m}$ (mT)	B_mag (mT)
$\mathbf{NV_1}$	$3.28 \pm 0.05 \cdot 10^{-3}$	$2.47 \pm 0.05 \cdot 10^{-3}$	14.46 ± 0.0	3.15 ± 0.02	14.8 ± 0.0
$\mathbf{NV_2}$	$3.08 \pm 0.11 \cdot 10^{-3}$	$2.82 \pm 0.10 \cdot 10^{-3}$	4.58 ± 0.0	14.08 ± 0.01	14.8 ± 0.01
$\mathbf{NV_3}$	$3.03 \pm 0.28 \cdot 10^{-3}$	$2.88 \pm 0.26 \cdot 10^{-3}$	2.45 ± 0.01	14.58 ± 0.02	14.79 ± 0.02
$\mathbf{NV_4}$	$3.14 \pm 0.24 \cdot 10^{-3}$	$2.73 \pm 0.25 \cdot 10^{-3}$	7.42 ± 0.01	12.81 ± 0.02	14.81 ± 0.02

Table 5.1.: Fitted frequencies together with the parallel ($B_{\text{ext}\parallel,m}$) and perpendicular ($B_{\text{ext}\perp,m}$) projections of the external field on the four NV directions as well as the determined magnitude of the external field B_mag.

field vector defined in Eq. 5.3, as well as Eq. 5.4, we find for the angles $\theta = 55°$ and $\phi = 15°$ the values of $B_{\text{ext}\parallel_{i},s}$ and $B_{\text{ext}\perp_{i},s}$, which are listed in Table 5.2. These values are in good agreement with the measured values in Table 5.1. The small deviation of the experimentally determined field projections on the NV axes from the theoretical values results from a not perfect alignment of the external field direction with the angles θ and ϕ.

5.2.2. POLARIZATION DEPENDENCE

To calibrate the external bias field, it is often beneficial to enhance the amplitudes of the peaks of the ODMR spectrum corresponding to a specific family of NV centers. This can be achieved by adjusting the polarization direction of the coherent laser light using

	$B_{\mathrm{ext}\parallel,s}$ (mT)	$B_{\mathrm{ext}\perp,s}$ (mT)
NV$_1$	14.46	3.15
NV$_2$	4.72	14.03
NV$_3$	2.3	14.62
NV$_4$	7.44	12.79

Table 5.2.: Calculated parallel ($B_{\mathrm{ext}\parallel,s}$) and perpendicular ($B_{\mathrm{ext}\perp,s}$) projections of the external field vector on the four NV center directions, when the external field vector is applied along the direction $\theta = 55°$ and $\phi = 15°$.

a $\lambda/2$-wave plate. In Fig. 5.7b, the ODMR spectrum for the same external field as in Fig. 5.7a is shown, where the amplitude of the peaks was varied by changing α.

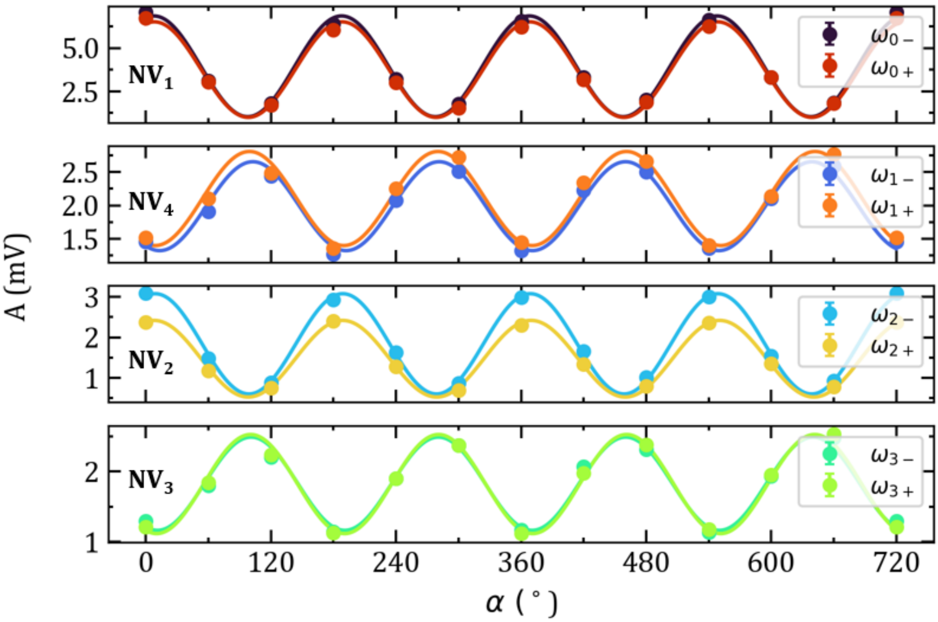

Figure 5.8.: Polarization dependence of the ODMR spectrum. As the NV$_1$ and NV$_2$ families lie in a plane perpendicular to the plane of the NV$_3$ and NV$_4$ families, their amplitudes of the resonance peaks is maximized if the amplitudes of the NV$_3$ and NV$_4$ peaks is minimized.

To obtain the dependence of the amplitudes of the eight peaks on the polarization angle α, we sweep α through 360° and fit the ODMR spectrum for each angle step. In Fig. 5.8, the fitted amplitudes of the eight resonances, highlighted in Fig. 5.7 by the vertical dashed lines, are presented. Furthermore, by fitting the amplitudes A with a sinusoidal function given by

$$A = A_0 + A_1 \sin(2\alpha + \alpha_0), \tag{5.6}$$

where A_0 is the offset, A_1 the amplitude of the oscillation, and α_0 the phase shift, we find that the amplitude dependence of the PL peaks on α of the NV_1 and NV_2 direction have a phase shift of 180° with respect to the NV_3 and NV_4 directions.

This can be explained by considering the orientations of the NVs. The NV_1 and NV_2 families lie in the xz-plane, while the NV_3 and NV_4 families lie in the yz-plane, which are orthogonal to each other. If the polarization of the laser light lies in the xz-plane, the amplitudes of the NV_1 and NV_2 peaks is maximized. However, the amplitudes of the NVs in the yz-plane is minimized, resulting in the 180° phase shift.

5.3. DYNAMIC MAGNETIC FIELD SENSING

Dynamic magnetic field sensing with NV centers often uses pulsed measurement techniques to study the spin dynamics of the NV centers. Two important experiments are T_1 relaxation measurements and Rabi oscillation experiments. The T_1 relaxation time, or longitudinal relaxation time, measures how long it takes for the spin system to return to thermal equilibrium after being disturbed. This measurement provides information on how NV centers interact with their environment, including dynamic magnetic fields [123, 124]. Rabi oscillation experiments involve driving coherent oscillations of the NV center spin states by applying a resonant MW field. The Rabi frequency, which is proportional to the strength of the applied microwave field, can be used to quantify the magnetic field strength at the NV center's location [57, 125].

5.3.1. PULSED MEASUREMENT SCHEMES

To measure Rabi oscillations and T_1 times the single photon counting setup described in section 4.3.2 is used. These measurements were conducted as part of a master's thesis by Lukas Colombo [114].

CW-ODMR

As the recorded signal consists of the PL signal and the background light reaching the detector, and as the PL signal itself depends on the temperature, a background correction is needed. Thus, the signal normalization consist of two steps. First, the laser is modulated with a square wave at a fixed frequency and with a duty cycle of 50% to account for the background light. If the laser is turned on, the sum of the PL signal I_{PL} and the background signal I_{off} is measured $I_{on} = I_{PL} + I_{off}$. On the other hand, if the laser is turned off, only the background signal I_{off} is measured. Therefore, the PL signal is given by the difference of the two signals

$$\Delta I = I_{on} - I_{off}. \tag{5.7}$$

Second, to eliminate fluctuations in the PL signal due to temperature, for each frequency the PL signal is recorded at the excitation frequency, referred to as ΔI_{PL}, and at a fixed reference frequency, which is chosen to be far away from the resonance frequency of the NV. The reference signal ΔI_{ref} is recorded immediately after the excitation frequency. If the excitation frequency is far away from the resonance frequency of the NV, the two signals are similar, while they differ in intensity if the excitation frequency lies close to the resonance frequency. To normalize the signal, the ratio between the excitation and the reference signal is calculated

$$I_{\mathrm{norm}} = \frac{\Delta I_{\mathrm{PL}}}{\Delta I_{\mathrm{ref}}} = 1 - C, \tag{5.8}$$

where C is the contrast of the signal.

The laser is modulated with a frequency of 10 kHz and photons are collected during 1 s for I_{on} and I_{off}. The reference frequency is set to 2 GHz.

COHERENT CONTROL

To coherently control the NV centers, a pulsed measurement scheme is required. By separating the spin initialization, manipulation, and readout processes in time, the power broadening of the ODMR line is reduced, as both the readout laser and the driving MW field contribute to power broadening [45]. Pulsed sequences consist of three main steps. First, the NV spin is initialized into the $m_S = |0\rangle$ ground state using a green laser pulse. Second, microwave pulses are applied to manipulate the spin state as required. Third, the spin state is read out using a second laser pulse. This sequence is repeated as often as necessary to achieve a good signal-to-noise ratio. Additionally, the readout signal is normalized against the initialization signal to correct for background fluctuations or temperature effects. The contrast in the measurements is defined as

$$C = 1 - \frac{N_{\mathrm{meas}}}{N_{\mathrm{ref}}}, \tag{5.9}$$

where N_{meas} and N_{ref} are the integrated counts for the readout and initialization pulses within a specific readout window, respectively.

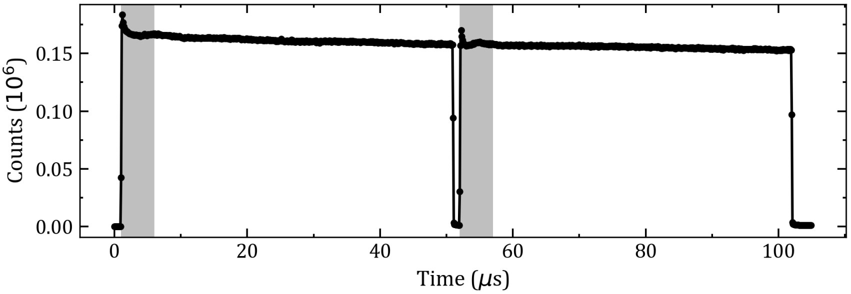

Figure 5.9.: PL signal of two consecutive laser pulses with durations of 50 µs each, separated by 1 µs. Following a 10 ms pause to allow thermalization of the system with the environment, the sequence repeats. The signal intensity of the second pulse is weaker than that of the first pulse, resulting in a negative contrast after normalization.

In Fig. 5.9, the counted photons in a sequence consisting of two pulses of length 50 µs, separated by 1 µs, are shown as a function of time. The first pulse initializes the NV centers into the $m_S = |0\rangle$ ground state, while the second pulse is used to read out the signal. The grey areas in the plot mark the time interval, during which the photons are counted, resulting in N_{ref} and N_{sig}. After a 10 ms waiting time, allowing the system to thermalize, the sequence is repeated and the signal is summed up. We find that the counts in the second pulse are decreased with respect to the first pulse. This might be explained by laser-induced heating of the NV environment during the first pulse, resulting in a reduction of the PL signal, as heating in the diamond reduces the PL signal [126]. In this case, the diamond cannot fully thermalize before the second pulse, and the signal remains decreased compared to the first pulse. Another explanation might be that the laser output itself is not constant during the two pulses, resulting in a change in the PL signal intensity, which depends on the laser power. However, the decreased PL signal in the second pulse results in a negative contrast in measurements with waiting times in the microsecond range. To account for this, the initialization and readout pulses are separated by a constant time interval, and their lengths are kept fixed for the following measurements, resulting in a constant offset of the measured contrast.

5.3.2. AMPLITUDE DAMPING

In a T_1 relaxation measurement, a sequence of optical pulses is used to initialize the NV center spin state, let it interact with its environment, and then monitor the return to equilibrium. In Fig. 5.10, a sketch of such a pulse sequence and the corresponding spin dynamics on the Bloch sphere is shown. First, a green laser pulse is used to initialize the system in the $m_S = |0\rangle$ ground state as depicted by the red arrow in the left Bloch sphere. After a waiting time τ during which the state decays, a second laser pulse is used to read out the state. By increasing the waiting time τ, indicated by the dashed pulses and the grey arrows in the sketch, the decay of the initialized state is detected.

After each readout pulse a waiting time is used to let the system fully return to thermal equilibrium before the sequence is repeated. To count the photons within a laser pulse a trigger signal is used as a time reference. Furthermore, the PL signal is read out only during the first microseconds of a green laser pulse, as indicated by the red pulses in the sketch.

In Fig. 5.11, a T_1 measurement is shown, where the reference and measurement signals are read out during 3 µs. To gain T_1, the data was fitted by an exponentially decaying function of the form

$$C = C_0 \cdot \exp(-\tau / T_1), \tag{5.10}$$

yielding $T_1 = (1.95 \pm 0.15)$ ms, which is in agreement with literature [112, 127].

5.3.3. RABI OSCILLATIONS

In a Rabi experiment, a series of microwave pulses with increasing duration is applied to drive coherent oscillations between the spin states, with the resulting oscillation frequency providing a direct measure of the magnetic field strength at the NV.

Fig. 5.12 shows the schematic sketch of a Rabi measurement. First, the spin population is initialized in the $m_S = |0\rangle$ ground state by a green laser pulse as indicated by the red arrow in the Bloch sphere on the very left. Next, a MW pulse of length τ is used to rotate the initialized state around the x-axis. The longer the pulse, the further the state

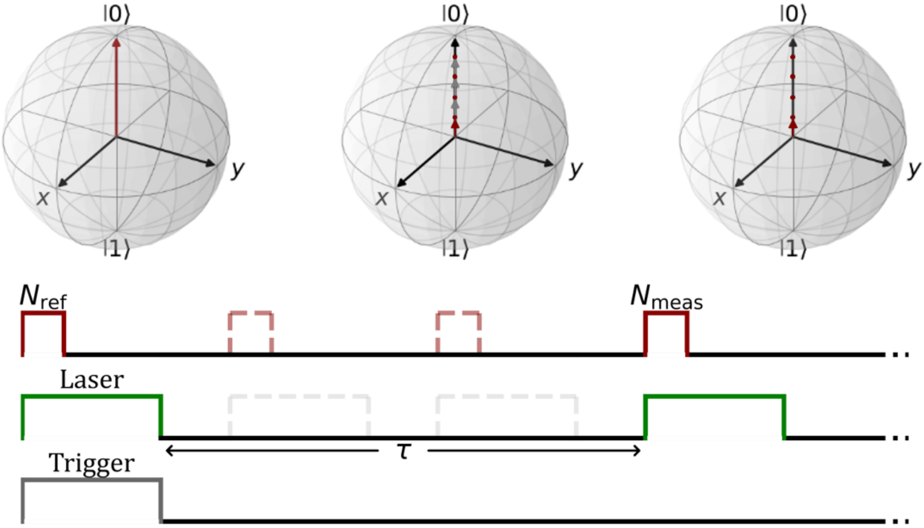

Figure 5.10.: Bloch representation (top) and pulse sequence (bottom) of a T_1 measurement. The NV center is initially prepared in the $m_S = |0\rangle$ state using a green laser pulse as indicated by the red arrow in the left Bloch sphere. Following a variable waiting time τ, the spin state is read out (red pulse) during the initial 3 µs of a laser pulse. A grey pulse serves as a time reference trigger signal. By adjusting τ (dashed pulses), the exponential decay of the initialized state amplitude is observed as indicated by the grey arrows in the middle Bloch sphere, reflecting the T_1 relaxation process towards equilibrium.

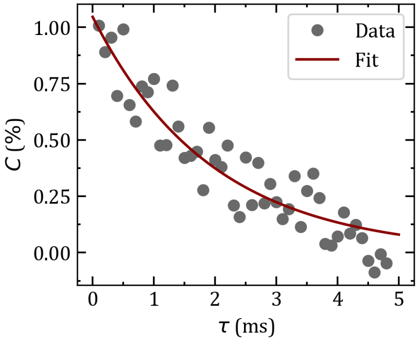

Figure 5.11.: Measurement of the T_1 time. By fitting the data with Eq. 5.10, we find $T_1 = (1.95 \pm 0.15)$ ms.

is rotated, as shown by the grey arrows in the middle Bloch sphere. Finally, a second green pulse is used to readout the state. A trigger pulse (black pulse) is used as a time reference in the sequence, and the signal is only read out during the first 3 µs of the laser pulses (red pulses). In such a measurement, the projection of the spin state onto the z-axis of the Bloch sphere oscillates sinusoidally between the $m_S = |0\rangle$ and $m_S = -|1\rangle$ or $m_S = +|1\rangle$ state. Thus, the measured signal will also oscillate sinusoidally due to the spin dependent PL signal of the NVs.

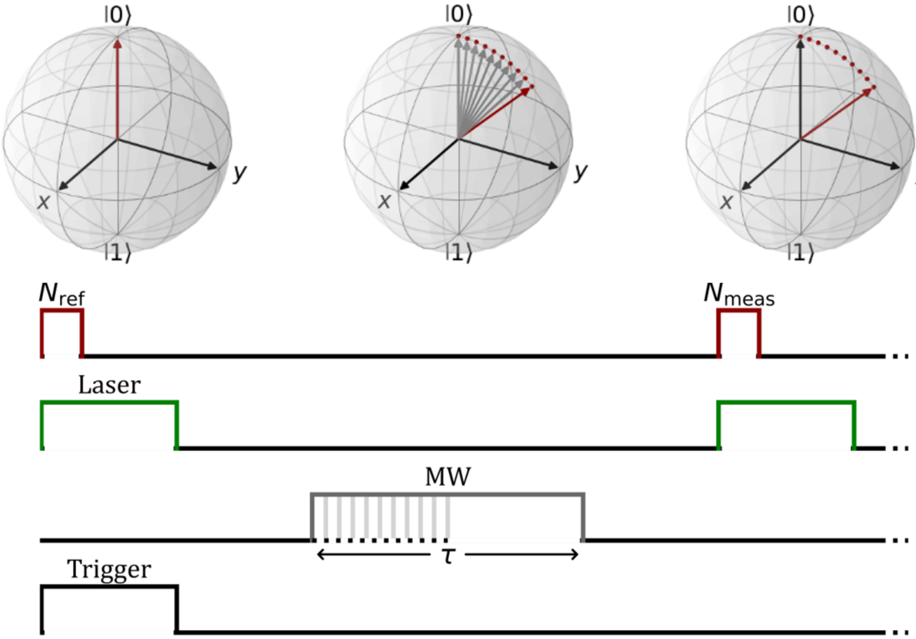

Figure 5.12.: Sketch of a Rabi sequence illustrating the spin evolution. The top Bloch spheres depict the spin state's evolution in response to the applied pulses shown at the bottom. A green laser pulse initializes the system into the $m_S = |0\rangle$ ground state (red arrow). Microwave (MW) pulses of variable duration τ, represented by the varying grey pulses, rotate the spin state along the x-axis. A second green laser pulse is used for state readout. A trigger pulse (black pulse) serves as a time reference for photon counting. The signal (red pulses) is detected only during the initial 3 µs of the green laser pulse, yielding the reference signal N_{ref} and the Rabi signal N_{meas}.

In Fig. 5.13, the Rabi experiment for transitions between the $|0\rangle$ and $|-1\rangle$ states is shown. To lift the degeneracy of the $\pm|1\rangle$ states, a bias field was applied, resulting in a resonance dip at 2.16 GHz, as presented in Fig. 5.13a, where the ODMR data was fitted by a Lorentzian. In Fig. 5.13b, the corresponding Rabi oscillations for varying power levels of the driving field are shown. For each data point, photons were collected during 60 s, making a complete measurement for a single power level take 5 h. Clearly, the frequency increases with stronger MW fields.

To examine the dependence of the Rabi frequency on the power level of the MW field,

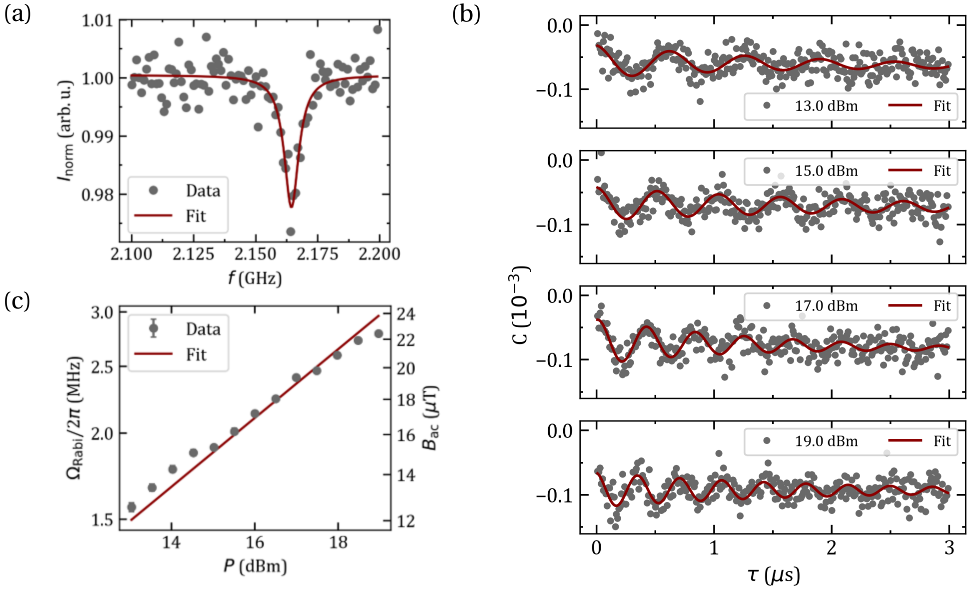

Figure 5.13.: Rabi oscillations. (a) ODMR dip of the ω_- transition (grey dots) and fit (red line) yielding a resonance frequency of 2.16 GHz. (b) Rabi oscillations in dependence of the MW pulse duration at different MW power levels. For higher power levels the Rabi frequency increases. The data was fitted by Eq. 5.11 to obtain the Rabi frequencies. (c) Dependence of the Rabi frequencies and the AC-field strength at the NV site on the applied MW power level P. The data was fitted by Eq. 5.12 demonstrating the proportionality of Ω_{Rabi} and B_{ac} on P.

the measurement data was fitted by an exponentially damped cosine function of the form

$$C(\tau) = A \cdot \cos\left(2\pi \frac{\tau}{T_{2\pi}} + \theta_0\right) \cdot \exp\left(-\frac{\tau}{T_{2_{\mathrm{Rabi}}}}\right)^2 + m \cdot \tau + C_0. \tag{5.11}$$

Here, $T_{2\pi}$ is the period of a Rabi oscillation, $T_{2_{\mathrm{Rabi}}}$ the dephasing time, m is a constant that accounts for the slope in the signal due to drifts in the temperature, and C_0 accounts for a constant offset in the contrast of the signal. In Fig. 5.13c, the power dependence of the Rabi frequencies $\Omega_{\mathrm{Rabi}} = 2\pi/T_{2\pi}$, obtained from the fit to Eq. 5.11, as well as the power dependence of the corresponding MW field strength B_{ac} at the NV site according to Eq. 3.19, is presented with a logarithmic scale on the left and right y-axis, respectively. Since the power is plotted in units of dBm, the x-axis is also plotted in a logarithmic scale.

To demonstrate the linear dependency of the Rabi frequency and the AC-field on the square root of the MW power level, the data was fitted by

$$\Omega_{\mathrm{Rabi}}/2\pi(P) \propto c \cdot \sqrt{P}, \tag{5.12}$$

resulting in a slope of $c = (10.5 \pm 0.1)\ \mathrm{MHz}/\sqrt{\mathrm{W}}$. Furthermore, we find that the AC-field varies between 12 µT and 24 µT for the applied range of MW power strengths.

5.4. SUMMARY

In this chapter, we discussed the essential experiments for performing magnetometry using an ensemble of NV centers. We began with cw-ODMR measurements, where we investigated how the signal varies with the strength of the applied MW power. Furthermore, by conducting ODMR measurements, we determined the magnitude of an external magnetic field and we varied the amplitudes of the peaks in the ODMR spectrum by using a $\lambda/2$ wave plate.

Additionally, we demonstrated the coherent control of NV centers through T_1 measurements and Rabi experiments. By increasing the MW power in the Rabi experiments, we showed the proportionality of the Rabi frequency to the square root of the applied MW power and determined the field strength of the applied MW field.

6

SPIN WAVE MEASUREMENTS USING NV CENTERS

In this Chapter, we discuss the use of an ensemble of shallowly implanted NV centers to measure spin waves in a magnetic thin film, in this case the low-damping ferrimagnetic insulator yttrium iron garnet (YIG) [20, 128], building on the seminal work reported in [83]. Sec. 6.1 introduces the type of sample used throughout this chapter. We then proceed with the determination of the distance between the NV layer and the sample surface in Sec. 6.2, which is an important parameter for calculating the amplitude of spin waves from the detected field. In Sec. 6.3, we describe how spin waves can be detected through their stray fields using NV centers. We then discuss in Sec. 6.4, how NV centers can image individual wave fronts of spin waves by creating a standing wave in the total stray field at the NV layer. Furthermore, we determine the spin wave dispersion from these measurements. Sec. 6.5 compares these measurements to spin wave imaging done by TR-MOKE. In Sec. 6.6, we phenomenologically model the NV spin wave measurements to explain the features observed in the NV spin wave images. We conclude this chapter in Sec. 6.7 by a short summary.

6.1. SAMPLES

In the following measurements, we used two samples. The first sample was a 200 nm thick YIG thin film grown on a gadolinium gallium garnet substrate using liquid phase epitaxy. The thin film posses a saturation magnetization $\mu_0 M_S = 185$ mT, as determined from a fit to the dispersion measured by the NV centers. To excite spin waves, a microstrip line S1 with a width of 5 µm was fabricated on top of the YIG film using optical lithography and electron beam evaporation of Ti(5 nm)/Au(100 nm). A second microstrip line S2 of Ti(5 nm)/Au(200 nm) with a width of 30 µm, as well as a 150 µm thick SiO_2 layer, were fabricated on top of S1 by optical lithography and electron beam evaporation. For the spin wave measurements, the external field **B** is applied along an NV axis, with an angle $\phi = 35°$ between the YIG thin film and the field direction, such that the projection of the external field onto the YIG film is parallel to S1. A sketch of the sample is shown in Fig.6.1a.

The second sample consisted of the same YIG thin film. A microstrip line with a U-shape of Ti(5 nm)/Au(100 nm) was fabricated on top of the YIG film using optical lithography and electron beam evaporation, as depicted in Fig. 6.1b. It has a width of 10 µm in the horizontal part of the bending. This sample was only used for the results presented in Subsec. 6.3.2.

In both cases, the diamond chip was placed on the YIG sample with the NV layer facing towards the magnetic surface. We used the diamond chips discussed in Sec 5.1.1.

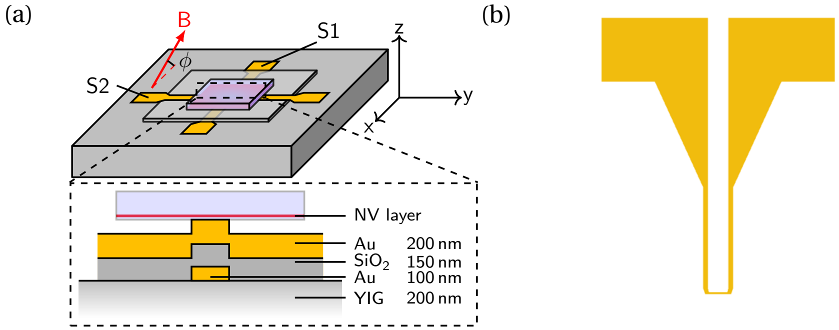

Figure 6.1.: Sample configurations. (a) A diamond chip containing a layer of NVs is positioned on a 200 nm thick YIG film grown on a gadolinium gallium garnet substrate. A microstrip line S1 excites spin waves in the sample. A second perpendicular microstrip line S2, separated from S1 by a SiO$_2$ layer, is used to generate an Oersted field $\mathbf{B}_{\mathrm{oe}}$ that oscillates at the same frequency as the spin wave stray field. An external magnetic field **B** is applied along S1 at an angle of $\phi = 35°$ with respect to the sample plane. (b) A U-shaped microstrip line grown on a 200 nm YIG film is used to excite spin waves.

6.2. DETERMINATION OF THE NV-YIG DISTANCE

The distance z_0 between the NV layer and the YIG surface is an important parameter in NV magnetometry measurements. It determines the spacial magnetic resolution that can be achieved using a single NV center. Furthermore, we need this parameter to simulate the spacial PL signal of spin wave measurements. To determine z_0, we reconstruct the magnetic field of a DC current in the coordinate system defined in Fig. 5.6. The reconstruction of the DC field is done by evaluating NV ODMR measurements in dependence of the distance from the excitation microstrip line. To generate the DC field and to detect the NV transitions at the same time, we simultaneously send an AC and a DC current trough S2 using a bias tee.

6.2.1. DETERMINATION OF THE EXTERNAL FIELD

To facilitate the determination of the DC field, we apply an external magnetic bias field $\mathbf{B_0}$ to lift the degeneracy of the NV transitions. We then scan the sample parallel to S1 and detect the ODMR spectrum at each position X. In Fig. 6.2a, we show the measured ODMR spectrum in dependence of the distance from S2, whose center is located at $X \approx 40$ µm. Directly above S2 the AC field is strongest, resulting in an enhanced contrast in the ODMR spectrum. As we do not send a DC current through S2, the positions of the ODMR peaks are independent of the distance from S2 and the frequency splitting is only caused by the constant external field. To gain the external field strength, we fit the ODMR spectrum at each position X with eight Lorentzians. The resonance frequencies obtained from the fits are presented in Fig. 6.2b as red dots. As a guide to the eye, the ODMR spectrum is plotted as well. At positions far from S2, the weak driving field resulted in a poor signal-to-noise ratio, making it impossible to fit some of the ODMR peaks accurately.

As discussed in Sec. 5.2, we can determine the parallel and perpendicular external field projections on each NV axis from the positions of the resonance frequencies by using Eqs. 3.7 and 3.8. This results in four parallel field components $B_{0\parallel_i}$ and four perpendicular field components $B_{0\perp_i}$ for each position X. The magnitude of the external field vector can now be calculated by $B_{\mathrm{mag},i} = \sqrt{B_{0\parallel_i}^2 + B_{0\perp_i}^2}$. At the position $X = 40$ µm, the calculated magnitudes were for example $B_{\mathrm{mag},1,2,3,4} = [14.81, 14.81, 14.81, 14.79]$ mT. These magnitudes need to be similar for all NV axes as each NV senses the same external field. We averaged over all magnitudes obtained from all positions X to gain $B_{\mathrm{mag}} = (14.81 \pm 0.02)$ mT.

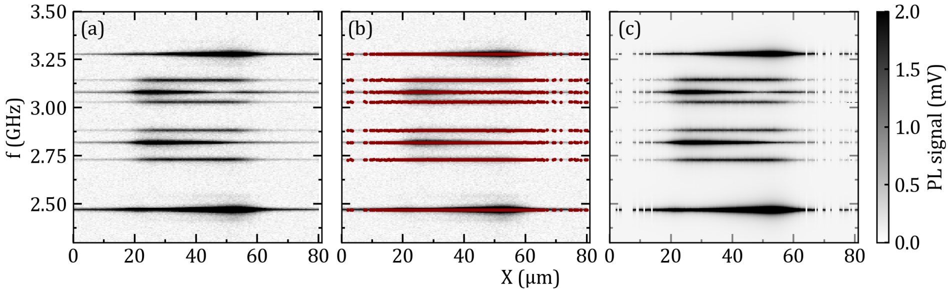

Figure 6.2.: (a) ODMR spectra plotted against the distance from the reference microstrip line S2. The center of S2 is located at $X \approx 40$ µm. An external magnetic field $\mathbf{B_0}$ is applied to split the NV transitions. (b) Fitted transition frequencies (red dots) plotted over the measured ODMR spectrum. For some positions far away from S2 the fits did not work, resulting in missing fitted frequencies. (c) Numerically reconstructed ODMR spectrum using the reconstructed resonance frequencies, the fitted amplitudes, and the fitted linewidths. The simulation is in good agreement with the measurement in (a). The reconstruction yields an external field of $\mathbf{B}_0 = (11.7, 3.1, 8.5)$ mT.

To reconstruct the external field vector, we define a magnetic field vector $\mathbf{B}_0$ in spherical coordinates

$$\mathbf{B}_0 = B_{\mathrm{mag}} \cdot \begin{pmatrix} \sin(\theta)\cos(\phi) \\ \sin(\theta)\sin(\phi) \\ \cos(\theta) \end{pmatrix}, \tag{6.1}$$

with the unknown polar and azimuthal angles θ and ϕ, respectively. Furthermore, we use the unit vectors of the four NV directions defined in Eq. 5.2. The parallel ($B^2_{0\parallel_i,s}$) and perpendicular ($B_{0\perp_i,s}$) projections of $\mathbf{B}_0$ on the four NV axes can be calculated by Eq. 5.4.

To gain the exact angles θ and ϕ, which determine the external field direction, the error between the measured and the simulated parallel and perpendicular field components, given by

$$\Delta B_0^2 = \Delta B^2_{\perp_i} + \Delta B^2_{\parallel,i}, \tag{6.2}$$

with

$$\begin{aligned} \Delta B^2_{\perp_i} &= (B_{0\perp_i,s} - B_{0\perp_i})^2, \\ \Delta B^2_{\parallel,i} &= (B_{0\parallel_i,s} - B_{0\parallel_i})^2, \end{aligned} \tag{6.3}$$

is numerically minimized for each position X. For the minimization we use an initial guess for the angles θ and ϕ, which was obtained from the known orientation of the external field in the experiment. The obtained angles where then averaged, resulting in $\theta = (54.75 \pm 0.04)^\circ$ and $\phi = (14.77 \pm 0.07)^\circ$.

Using these values we find $\mathbf{B}_0 = (11.7, 3.1, 8.5)$ mT. To check whether this value is correct, we numerically invert Eqs. 3.7 and 3.8 to gain the simulated transition frequencies $\omega_\pm(B_{0\perp_i,s}, B_{0\parallel_i,s})$. We can now reconstruct the measured ODMR spectra by calculating the eight ODMR dips using the fitted amplitudes and linewiths of Fig. 6.2a and the simulated transition frequencies. In Fig. 6.2c the reconstructed ODMR spectrum in dependence of the distance X is shown. We find, that the calculated external field vector correctly reproduces the measured ODMR spectrum.

6.2.2. 3D RECONSTRUCTION OF THE DC FIELD

In addition to the external field $\mathbf{B}_0$, we now send a DC-current of $I_{\mathrm{DC}} = 80$ mA through S2, which generates a magnetic DC-field at the position of the NV centers depending on the distance z_0 between the NV layer and the YIG surface. The NVs sense the total magnetic field $\mathbf{B}_{\mathrm{tot}} = \mathbf{B}_0 + \mathbf{B}_{\mathrm{DC}}$, so that spatially dependent shifts in the NV ODMR frequencies develop, as shown in Fig. 6.3a. The imaged area is the same as in Fig. 6.2. In Fig. 6.3b, we show the fitted resonance frequencies (red dots) plotted over the detected ODMR spectrum. The fits failed to work, if the signal to noise ratio was too low. Furthermore, at the edges of S2, where the ODMR dips overlap, the error in the fitted frequencies is biggest.

To reconstruct the ODMR spectrum and thereby $\mathbf{B}_{\mathrm{tot}}$, we use the same approach as in the determination of the external field. From the fits of the measured ODMR spectrum at each position X we calculate the projections of total field on the NV axes. Second, we calculate the angles $\theta(X)$ and $\phi(X)$ for each position X on the sample by minimizing the error between the measured total field amplitudes and the reconstructed total field amplitudes, that depend on $\theta(X)$ and $\phi(X)$. Thereby, we gain the total field vectors $\mathbf{B}_{\mathrm{tot}}(X)$. Fig. 6.3c shows the obtained reconstructed ODMR spectrum, which is in

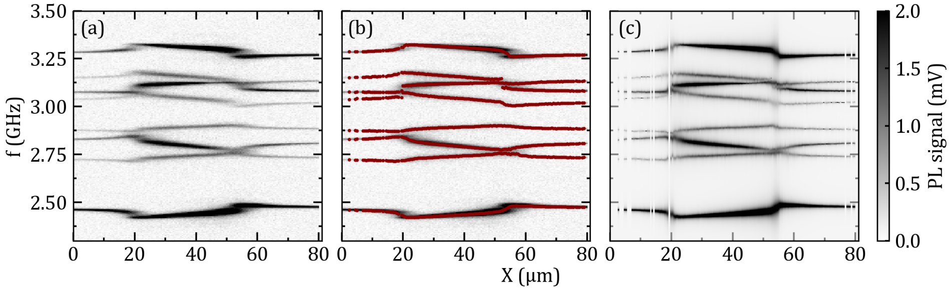

Figure 6.3.: (a) ODMR spectra plotted against the distance from the reference microstrip line S2, when a DC current of $I_{DC} = 80$ mA is sent through S2. The external magnetic field and measurement area are the same as in Fig. 6.2. The total field sensed by the NVs is $\mathbf{B}_{tot} = \mathbf{B}_0 + \mathbf{B}_{DC}$. (b) Fitted transition frequencies (red dots) of the data in (a). (c) Reconstructed ODMR spectrum in dependence of the distance X from S2. Overall, the reconstruction closely matches the measurement. The main discrepancies between the reconstruction and the measurement occur at the edges of S2, which are attributed to errors in the fitted frequencies.

good agreement with the measurement in Fig. 6.3a. The primary differences between the measurement and the reconstruction are found at the edges of S2, where the error in the fitted resonances is greatest.

The position dependent magnetic DC field is now obtained by $\mathbf{B}_{DC}(X) = \mathbf{B}_{tot}(X) - \mathbf{B}_0$ using the values for $\mathbf{B}_0$ measured in Sec. 6.2.1. In Fig. 6.4, the X-, Y-, and Z-components of the obtained DC magnetic field (blue, grey, and red dots) are plotted against the coordinate X. The Y-component (dark grey dots) shows an offset of $y_{off} = (0.215 \pm 0.002)$ mT. The green dots show the Y-component, when this offset was subtracted. The origin of this additional constant field contribution along the Y-axis, however, is unclear. If S2 is not perfectly aligned with the Y-axis, it would result in a Y-field component that depends on the distance X, rather than a constant Y-field component. Furthermore, every field contribution that is not stemming from the DC field of S2, such as the earth magnetic field, or stray fields other then the external magnetic field, should be included in $\mathbf{B_0}$ and should thus not show up in $\mathbf{B}_{DC}$. It is possible that the magnet generating the external field has drifted slightly over time, resulting in such a field offset. The deviation of B_y from zero in the vicinity of the edges of S2 results from the error of the fitted resonance frequencies in this region. To fit the obtained fields, we subtracted the offset from the Y-component of the DC field. The data was then fitted with Eq. 2.41 (solid lines).

In table 6.1, the expected and fitted parameters are listed, where I_{DC} is the DC current sent through S2, x_0 is the offset of center of S2 from $X = 0$, w is the width of the microstrip line, and z_0 is the unknown NV-YIG distance. We find a good agreement between these values. From this fit we extract a NV-YIG distance of $z_0 = (1.4 \pm 0.1)$ μm.

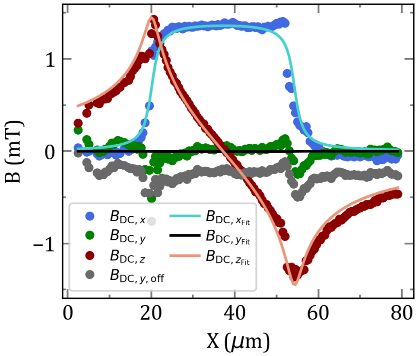

Figure 6.4.: Reconstructed DC magnetic field in dependence of the distance X from S2. The center of S2 is located at $X \approx 40$ µm. The Y-component of the reconstructed DC field shows a constant offset of $y_{\mathrm{off}} = (0.215 \pm 0.002)$ mT (grey dots). To fit the data this offset was subtracted resulting in the green dots. The deviation of B_y from zero in the vicinity of the edges of S2 result from the error of the fitted resonance frequencies in this region. From the fit we gain a NV-YIG distance of $z_0 = (1.4 \pm 0.1)$ µm

	I_{DC} (mA)	x_0 (µm)	w (µm)	z_0 (µm)
Expected value	80	40	30	-
Fitted value	78.2 ± 0.7	37.2 ± 0.7	34.2 ± 0.2	1.4 ± 0.1

Table 6.1.: Comparison of the expected and fitted values used to determine the NV-YIG distance by fitting the reconstructed DC magnetic field using Eq. 2.41.

6.3. NV-based Spin Wave Detection

To detect spin waves using NV centers, two conditions must be met. First, the NV centers must be in close proximity to the YIG surface, as the amplitude of the spin wave stray field decays exponentially with distance from the surface as can be seen in Eq. 2.40. To minimize the distance between the NV centers and the YIG surface, small diamond chips were used to reduce the likelihood of dirt particles being located between the diamond chip and the YIG sample. Second, the spin wave must be excited at the transition frequency of the NV center. For DE spin waves, the stray field is left- and right-handed circularly polarized and has only on one side of the microstrip line a strong stray field on top of the YIG surface [57, 83, 129]. Thus, it only drives ω_- transitions effectively, resulting in a spin-dependent photoluminescence (PL) signal. Consequently, the spin wave must be excited at a frequency corresponding to the $m_S = |0\rangle$ to $m_S = |-1\rangle$ transition.

6.3.1. ODMR Spectra

In Fig. 6.5, the NV photoluminescence signal, obtained via lock-in detection and measured approximately ±10 µm away from the center of S1, is shown in dependence of the external magnetic field $\mathbf{B_0}$ and the microwave current frequency. Here, $\mathbf{B_0}$ is applied along S1 at an angle of $\phi = 35°$ relative to the sample plane, aligning it with one of the four possible orientations of the NV axes. The peaks in the PL signal belong to the ESR transitions in the ground ($\omega_\pm, \omega_\perp$) and excited states (ω_{ex}), where only the PL signal of NV centers aligned with $\mathbf{B_0}$ result in a linear dependence on $\mathbf{B_0}$. A small mismatch in the alignment of the external field results in the splitting of the inner peaks. In Fig. 6.5a, the spectrum was detected on the left side of S1. The NVs are mainly driven by the Oerstedfield of the microstrip line, as the spin wave propagates on the bottom side of the YIG film. In Fig. 6.5b the spectrum was detected on the right side of S1. We find an enhanced contrast in the ω_- transitions for frequencies above the ferromagnetic resonance (FMR) limit, as the NVs are not only driven by the microwave field of S1 but additionally also by the spin wave stray field $\mathbf{B}_{\mathrm{sw}}$.

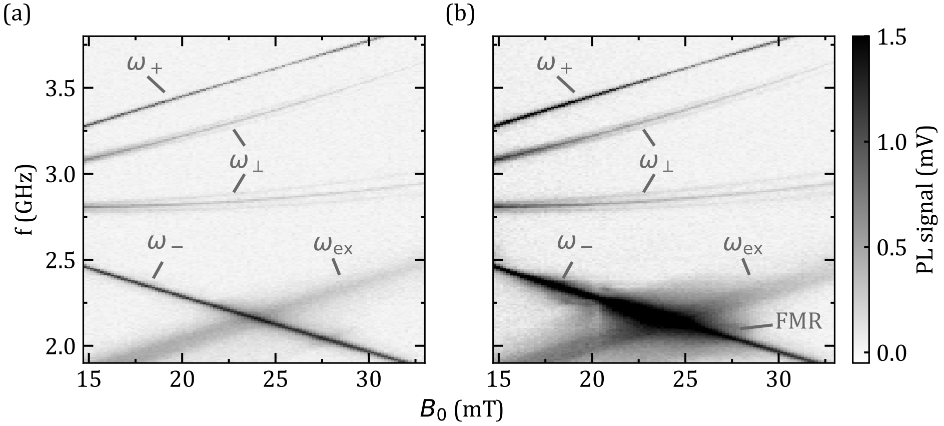

Figure 6.5.: Photoluminescence spectrum of the NV centers as a function of the external magnetic field $\mathbf{B_0}$ and the driving frequency f. Transitions in the ground state ($\omega_\pm, \omega_\perp$) and excited state (ω_{ex}) appear as peaks in the signal. The signal is detected at +10 µm (a) and −10 µm (b) away from the center of S1. Due to the handedness of the circularly polarized spin wave stray field, the ω_- transitions in (b) are enhanced for frequencies above the ferromagnetic resonance (FMR) limit.

6.3.2. NON-PHASE-RESOLVED IMAGING

NV centers can be used to image DE spin waves by continuously exciting them at the ω_- transition frequency while scanning the sample. This measurement is demonstrated in Fig. 6.6a, where a MW current of 2.49 GHz was applied for spin wave excitation. The U-shaped microstrip line and the direction of the external magnetic field $\mathbf{B_0}$ are indicated by the dashed black lines and the white arrow, respectively. We find that the NV centers are effectively driven above the microstrip line due to the Oersted field, as can be seen from the enhanced contrast in this region marked by the dashed black lines. Additionally, the NVs are driven by the stray field of the spin waves traveling in the $-\mathbf{Y}$ direction, as expected for DE spin waves. Within the area containing the contrast induced by the spin waves stray field, we observe regions that have a stronger contrast than others, which can be explained by spin wave caustics. Furthermore, we find some dots in the image, which stem from dirt on the sample surface. In Appendix A, the measurement is shown for a reversed external magnetic field direction, resulting in a reversed traveling direction of the excited DE spin waves.

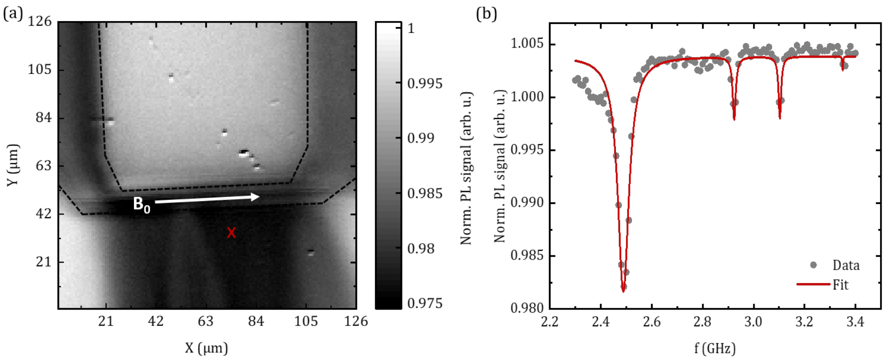

Figure 6.6.: (a) DE spin wave excited at 2.49 GHz by an U-shaped microstrip line (dashed black lines). A strong spin wave stray field on top of the YIG surface is detected only on the bottom side of the microstrip line. The direction of the external field $\mathbf{B_0}$ is indicated by the white arrow. (b) ODMR spectrum (grey dots) measured at the position marked by the red cross in (a), reveals an enhanced contrast at the $\omega_- = 2.49$ GHz transition due to the left-handed circularly polarized spin wave stray field. The data was fitted using four Lorentzian functions (red line).

Fig. 6.6b displays the ODMR spectrum recorded at the position marked by the red cross in Fig. 6.6a, along with a fit using four Lorentzian functions. In this spectrum, the dip at $\omega_- = 2.49$ GHz is significantly enhanced due to the left-handed circularly polarized stray field of the DE spin wave. Conversely, the $\omega_+ = 3.35$ GHz transition is barely visible. The observed dip at ω_+ might result from a weak contribution of the MW field from the microstrip line or an imperfect circular polarization of the spin wave's stray field. We conclude, that this technique allows to efficiently image the propagation of spin waves, however, it does not reveal the individual wavefronts of the spin waves.

6.4. PHASE-RESOLVED SPIN WAVE IMAGING

In order to gain the phase sensitivity to image individual wave fronts of the spin waves, a standing wave in the total magnetic field with a spatial periodicity equal to the wavelength of the spin wave is needed above the YIG sample. We accomplish that by using a second perpendicular reference microstrip line (S2), isolated from S1 by an insulating

SiO_2 layer, as indicated in Fig. 6.1a. A microwave current that generates an Oersted field $\mathbf{B}_{oe}$ oscillating at the same frequency as $\mathbf{B}_{sw}$ is sent through S2 by using a power splitter. The superposition of $\mathbf{B}_{oe}$ with the spin wave stray field $\mathbf{B}_{sw}$ results in a standing wave pattern in the total magnetic field that drives the NV ESR with a spatial periodicity equal to the wavelength of the spin wave [57].

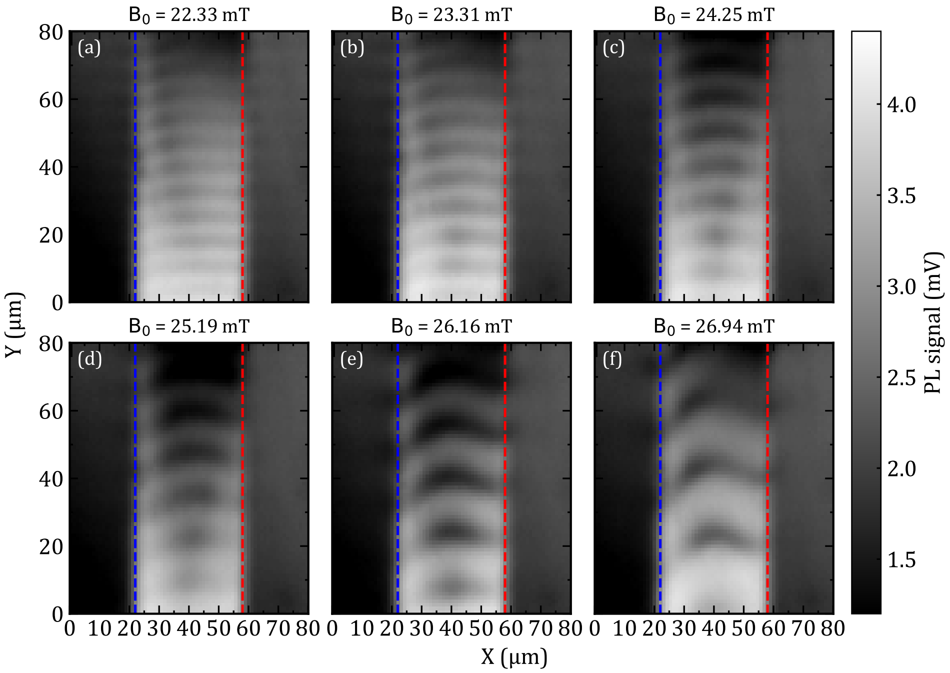

Figure 6.7.: Spatially resolved PL signal measured above the YIG film for spin waves excited with varying frequencies by S1. The edges of S2 are indicated by the vertical dashed lines. The X-axis is located 10 µm away from the center of S1, and the center of S2 is at $X = 40$ µm. The magnetic field $\mathbf{B_0}$ is applied along S1 at an angle of $\phi = 35°$ relative to the sample plane. In (a) to (f) the external field was increased, resulting in longer wavelengths of the detected wave fronts.

In Fig. 6.7, the PL signal for a spatial scan over the sample is shown for different external fields in the range of 22.33 mT to 26.94 mT increasing from (a) to (f). The measurements in this section were all taken with 30 mW laser power and 0 dBm MW power. As the scanning direction of the stage on which the sample is mounted is slightly misaligned with the Y-axis along which S2 is oriented, we rotated the images in Fig. 6.7 by an angle $\theta = -2.5°$. Thereby, we also transformed the X and Y axes by $X(Y) = X(Y)_m / \cos(\theta)$, where $X(Y)_m$ are the original, not rotated axes. The non-corrected data is shown in the appendix B. To gain an improved signal, each column in the plots was measured five times and averaged. The X-axis ($X = 0$) in each scan, aligned with S1, is located approximately 10 µm away from the center of S1. Furthermore, we scanned over S2, which is aligned with the Y-axis, with its center located at $X = 40$ µm. We find an enhanced contrast in the imaged spin wave amplitude directly above S2, as the superposition of the Oersted field of S2 and the spin wave stray field results in the strongest amplitude. Furthermore, the contrast in the PL signal decays with increasing distance from the X-axis. Close to the X-axis, the NVs are, in addition to the Oersted field of S2 and the spin wave stray field, driven by the Oersted field of S1. This signal weakens with increasing distance from the X-axis, resulting in decreasing contrast in the PL signal. Finally, we observe a phase shift of the wave fronts at the edges of S2, indicated by the vertical dashed lines, and a change of the wave lengths of the spin waves resulting in a light bending of the wave fronts towards the center of S2, which we will discuss in the following.

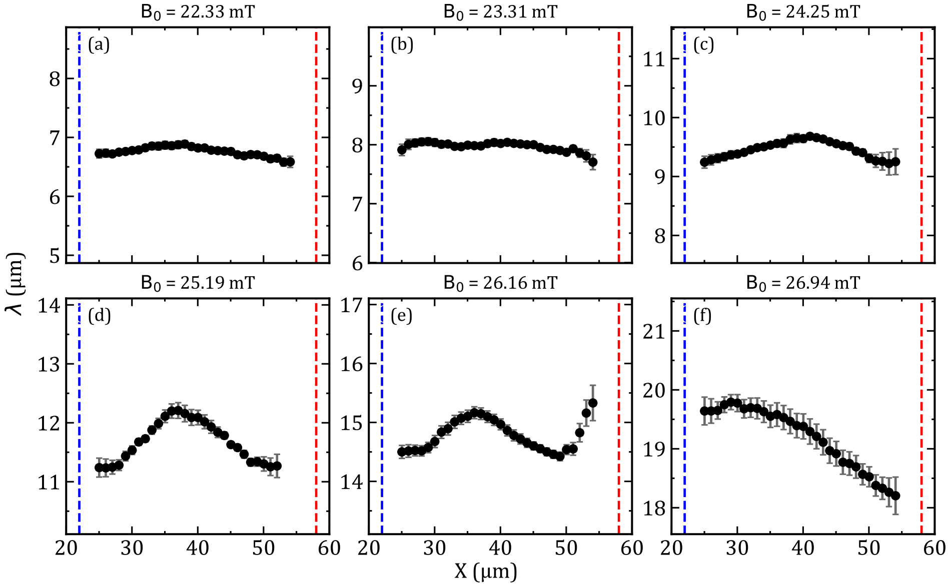

Figure 6.8.: Fitted wavelengths plotted against the position X on S2. The red and blue vertical dashed lines indicate the edges of S2. In (a) to (f) the external field was increased, resulting in longer wavelengths of the detected wave fronts. For higher fields the wavelengths increase towards the middle of S2. The signal was fitted using Eq.6.4.

To gain the wavelengths of the measured spin waves, we fit the PL signal in Fig. 6.7 for each position X within the red and blue dashed lines with the equation

$$I = Ae^{\alpha(x - x_{\text{off}})} \cdot \sin\left(\frac{2\pi}{\lambda} y + \phi\right) + c \cdot y + y_0. \tag{6.4}$$

Here, A is the amplitude of the signal, α the damping factor, $x_{\text{off}} = 40$ µm the location of the center of S2, λ the spin wave wavelength, ϕ the phase shift, c the signal slope, and y_0 the offset. The obtained wavelengths are plotted in Fig. 6.8. As the amplitude of the wave fronts vanishes towards the the edges of S2, it is impossible to fit the wavelength for line scans close to the edge of S2. We find that with increasing fields the fitted wavelength does not stay constant, which results in the bending of the spin wave wave fronts. It is not clear where this wavelength change stems from. A wavelength change of this manner would emerge if an additional time-independent external magnetic field parallel to the direction of S1 exists. As the wavelength increases towards the middle of S2 this field must be increasing towards the center of S2. A DC current in S2 could result in such a field. However, it is not clear why it should exist, as S2 was only connected to the MW generator. Due to the broad geometry of S2 eddy currents might occur. Eddy currents are loops of electrical current that are induced within a conductor when it is exposed to a changing magnetic field. According to Faraday's Law of Induction [130, 131], a changing magnetic field creates an electromotive force in the conductor, leading to circular currents within the material. These currents flow in closed loops and are typically confined to the surface layer of the conductor due to the skin effect. The magnetic field generated by eddy currents opposes the change in the magnetic field that caused them, according to Lenz's Law [132]. This opposition can affect the overall magnetic field in the vicinity, potentially altering the behavior of the original time-varying field. However, as these are time-dependent currents, the induced field component parallel to S1 should average to zero over time.

6.4.1. DETERMINATION OF THE WAVEFRONT PHASE SHIFT

To determine the phase shift in the wave fronts at the edge of S2, the line scans taken along the dashed vertical lines in Fig. 6.7 (a) to (f) are plotted in Fig. 6.9. The black data points are from the line scan at $X = 22$ µm, while the grey data points belong to the line scan at 58 µm. Furthermore, the inset shows the whole line scans and the dashed rectangle indicates the region of the data that is plotted.

The PL signal I of the plotted data was fitted with Eq.6.4, while the wavelength was kept constant for both line scans. In Fig. 6.10, the fitted phase shifts of the data in Fig. 6.9 (a) to (f) are shown in dependence of the external field $\mathbf{B_0}$. We find that the phase shifts are close to 150°. If only the Oersted field of S2 and the spin waves stray field is considered, a phase shift of 180° between the wave fronts on the left and right side of S2 is expected, as the Oersted field of S2 has an opposite sign on the left and right side of S2. The superposition of the Oersted field with the spin wave stray field, which has a constant sign at a given time t over the whole measurement area, should thus result in a phase shift of 180° at the edges of S2. In Fig. 6.10, 180° is indicated by the red dashed line. The deviation of the fitted phase shifts from 180° could result from different reasons. First, accurately identifying the edges of S2 is challenging. If the line scan is taken slightly shifted to the center of S2, it introduces an error. On the other hand, if the line scan is taken too far from the edge of S2, the wave fronts in the signal quickly disappear, resulting in a big uncertainty in the fits. To determine the phase shift, the wavelength needs to be kept constant. Thus, an error in the fitted wavelength also results in an error in the phase shift.

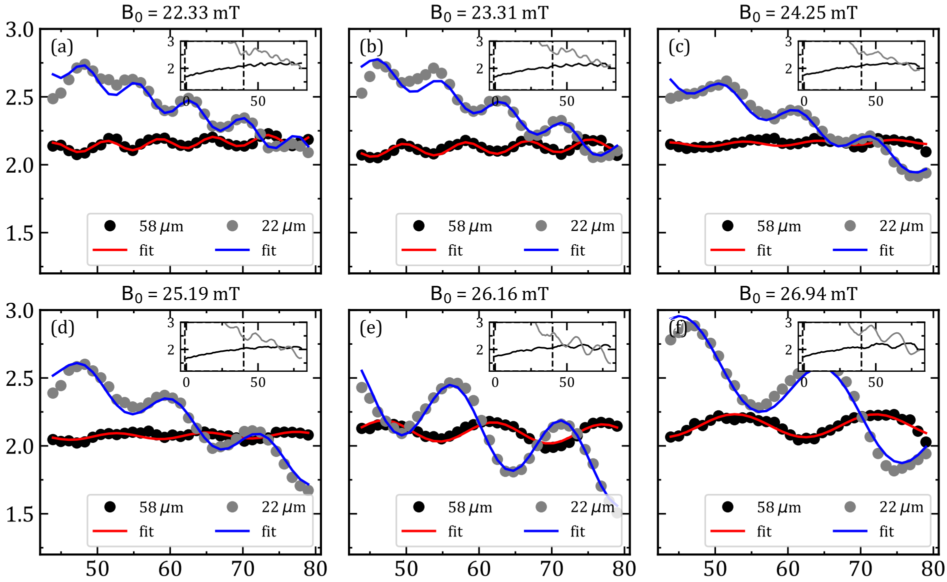

Figure 6.9.: Line scans of the PL signal that were taken at the left edge (black dots) and right edge (grey dots), indicated by the dashed lines in Fig.6.7, of S2. These line scans reveal a phase shift in the detected wave fronts between the two edges of S2. The inset shows the whole line scan, with the dashed rectangle highlighting the region of the plotted signal. For the fits, only the data between $Y = 40\,\mu\text{m}$ and $Y = 80\,\mu\text{m}$ is used, as the signal is clearest in this range.

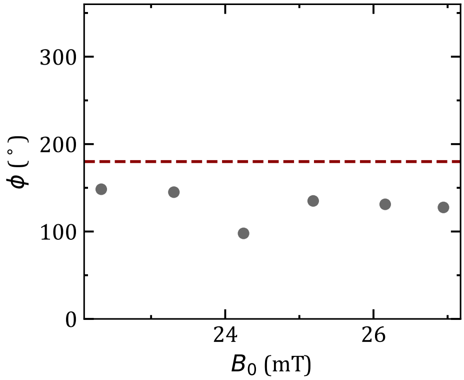

Figure 6.10.: Phase shift in the wave fronts between the left and right edges of S2. The fitted phase shifts are close to 180°, as indicated by the horizontal red dashed line.

6.4.2. DETERMINATION OF THE DISPERSION

To determine the spin wave dispersion, line scans of the PL signal at X = 40 µm were taken for external fields varying in small steps. Each line scan was repeated three times and averaged. In Fig. 6.11, six examplary scans are plotted against the position on the sample. The data was fitted by Eq. 6.4 to gain the wavelength of the excited spin waves. As expected, the wavelength increases with increasing external field.

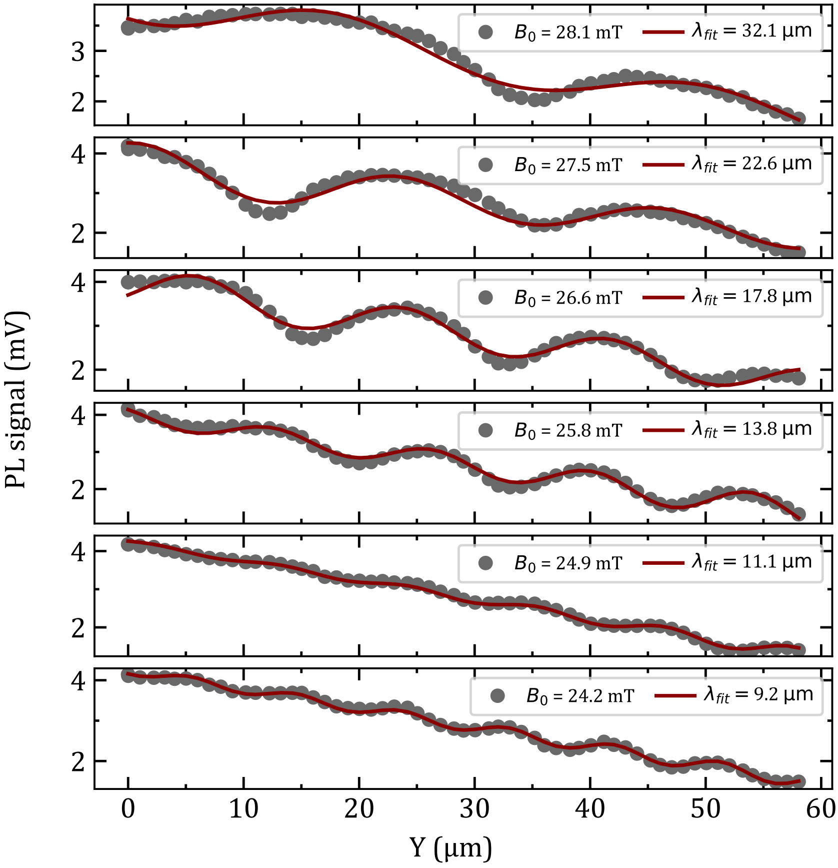

Figure 6.11.: Line scans of the PL signal showing spin waves with varying wavelengths taken at X = 40 µm and parallel to S2. The data was fitted by Eq. 6.4 to gain the dispersion.

In Fig. 6.12a, the fitted wavelengths λ of the line scans are shown in dependence of the external field (grey dots). To estimate the error in the wavelength, we additionally plotted the fitted wavelengths at X = 40 µm of Fig. 6.8 (a) to (f). These are the blue data points labeled as $\lambda_{\mathrm{NV}_{2\mathrm{D}}}$. The blue shaded area around these data points indicates the maximum deviation of the wavelengths in Fig. 6.8 (a) to (f) for each external field. This deviation was obtained by taking the minimum and maximum fitted wavelength for each external field. From this comparison, we conclude that even though the wavelengths do not remain constant, the variation does not significantly affect the measured dispersion.

To correct for the angle θ between the scanning direction and the Y-axis, the fitted wavelengths were divided by $\cos(\theta)$. As θ is small this correction resulted a wavelength change $\Delta\lambda < 31$ nm, which is a lot smaller than the resolution limit of the setup, as well as the step size of the scans. The correction is thus negligible. To obtain the red theory curve, the spin wave dispersion at the resonance frequency of the ω_- transition was calculated using the Eqs. 2.37 and 2.38 with the angles $\theta = 35°$ and $\phi = 90°$. This is illustrated in Fig. 6.12b, where the spin wave dispersion at a field B_0 is shown as the gray line, while the ω_- frequency of the NV transition is plotted as a red dot. The NV centers can only measure spin waves with the k-vector corresponding ω_-. We find that the fitted wavelengths are in good agreement with the theory curve.

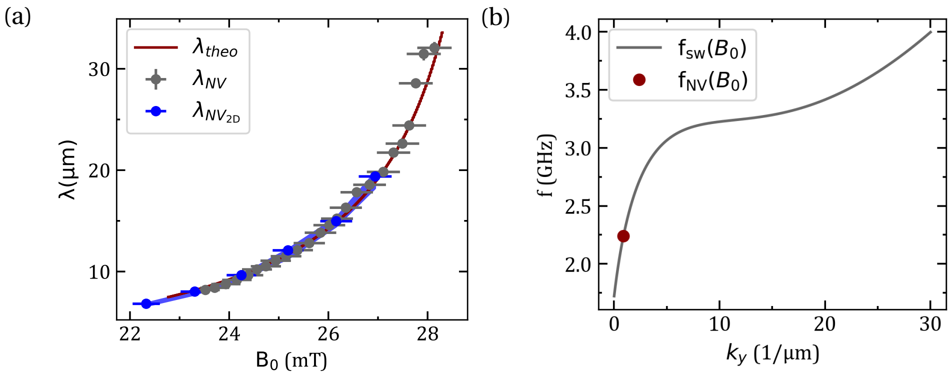

Figure 6.12.: (a) Spin wave dispersion obtained from NV spin wave measurements. The grey dots are the obtained wavelengths of the fitted line scans. The blue data points represent the fitted wavelengths at $X = 40$ μm of Fig.6.8 (a) to (f). The blue shaded area around these points indicates the maximum deviation of the fitted wavelengths for each external field. The fitted wavelength align well with the theory curve (red line). (b) Spin wave dispersion (grey line) for a constant external field $\mathbf{B_0}$ plotted against the k-vector and the excitation frequency. NV centers can only detect spin waves oscillating at the transition frequency f_{NV} (red dot) determined by Eq. 3.6.

6.5. COMPARISON TO TR-MOKE

In the following, we compare our NV measurements to TR-MOKE measurements. To do so, we adjust the external static magnetic field $\mathbf{B_0}$ in the TR-MOKE measurements such that the spin wave frequency coincides with the transition frequency ω_- of the NV centers. This allows us to probe spin waves with varying wavelength, detectable by both measurement techniques.

Fig. 6.13 shows propagating spin waves detected by TR-MOKE measurements in the DE-configuration for increasing external fields from (a) to (d) with an excitation fre-

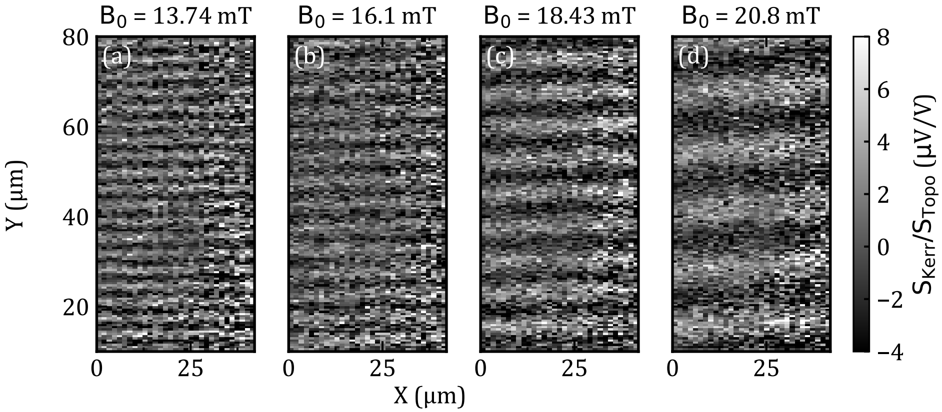

Figure 6.13.: TR-MOKE measurements of spin waves for different frequencies and fields. The excitation microstrip line is located about 10 μm away from the X-axis ($X = 0$). (a) to (d) show spin waves excited using increasing external fields.

quency equal to the ω_- transition of the NVs. In the NV measurements, the field is applied along S1 and one of the NV quantization axes. Given that the external field is always less than 30 mT, significantly smaller than the saturation magnetization of YIG, $\mu_0 M_S \approx 185$ mT, the static magnetization of the YIG film tilts only slightly out of plane, at an angle $B\sin(\phi)/(\mu_0 M_S) \leq 5.3°$ [57]. Hence, direct comparison between the NV measurements and the in-plane MOKE measurements is feasible. In Fig. 6.14a, we show the dispersion obtained from fitting the data of the TR-MOKE measurements by Eq. 6.4 for two orientations of the external field, alongside the theoretical dispersion curve (red line). To gain more data points in the same wavelength range as the NV data, we also used SNS-MOKE, allowing us to detect spin waves that are not excited at integer multiples of the laser pump frequency $f_{\text{pump}} = 80$ MHz. The dark blue data points were obtained for spin waves excited in DE-configuration, $\theta = 0°$ and $\phi = 90°$, while the light blue data was obtained for spin waves where the external field was applied along the NV axis, $\theta = 35°$ and $\phi = 90°$. To facilitate a direct comparison of the two data sets, we transpose the in plane fields of the DE TR-MOKE measurements into the direction of the NV center axis by dividing them by $\cos(\theta)$. The deviation in the fitted wavelengths arises from errors in the magnetic field calibration, which was done separately for the DE- and NV-configuration. However, within the bounds of this errors, the measurements closely match the expected theoretical curve, demonstrating the negligible effect of the perpendicular component of the external field with respect to the thin film plane.

In Fig. 6.14b, the theoretical dispersion curve (red line), alongside the fitted wavelength of the NV measurements (grey dots) and the MOKE measurements (dark blue dots) are shown. The data sets are in good agreement with each other. This consistency demonstrates the reliability and equivalence of the two measurement techniques.

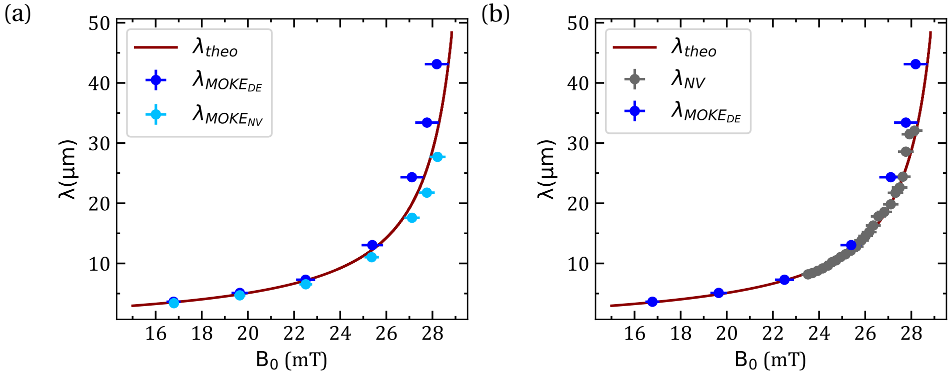

Figure 6.14.: (a) Dispersion of the excited spin waves, if the external magnetic field is applied in DE-configuration (dark blue dots) and along S1 at an angle of $\phi = 35°$ relative to the sample plane aligning it with a NV axis (light blue dots). The DE-fields were transposed into the direction of the NV center axis by dividing them by $\cos(\theta)$. The theoretical dispersion curve (red line) is in good agreement with the fitted wavelengths. (b) Comparison of the dispersion measured with NV centers (grey dots) and with TR-MOKE (blue dots), together with the theory curve (red line). The determined wavelengths are in good agreement with the theoretical dispersion curve.

6.6. SIMULATION

To phenomenologically model the magnetic stray field above the YIG film which drives the NV transitions, we calculate the magnitude of the perpendicular time-dependent total magnetic field $B_{\text{tot},\perp}$ at the NV site and relative to the NV axis. Thereby, we take into account that ESR transitions can only be driven by AC-fields perpendicular to their quantization axis. We use a coordinate system where the X-axis is aligned with S1, the Y-axis with S2, and the Z-axis with the normal vector of the sample plane, as indicated in Fig. 6.1a. The total field $\mathbf{B}_{\text{tot}}$is a superposition of the spin wave stray field above the film $\mathbf{B}_{\text{sw}}$, as well as the Oersted field $\mathbf{B}_{\text{oe}}$ of S2

$$\mathbf{B}_{\text{tot}}(t) = \mathbf{B}_{\text{sw}}(t) + \mathbf{B}_{\text{oe}}(t). \tag{6.5}$$

Fig. 6.15a shows the Y- and Z-components of the spin wave stray field at a time t given by Eq. 2.40, while Fig. 6.15b shows the X- and Z-components of the Oersted field given by Eq. 2.41. We used the parameters $z_0 = 1.4$ µm for the NV-YIG distance, $\mu_0 M_S = 185$ mT for the saturation magnetization, $d_{\text{YIG}} = 200$ nm for the YIG thickness, $d_{\text{Diamond}} = 100$ µm for the diamond thickness, $w = 30$ µm for the width of S2, and $I = I_0 \cos(\omega t)$ with $I_0 = 0.8$ A for the current in S2. Furthermore, for the amplitude of the spin wave stray field we used $m_0 = 0.1 M_S/\mu_0$. This parameter was chosen to be smaller than the saturation magnetization. However, we did not experimentally determine it.

The magnitude of the total time-dependent magnetic field perpendicular to the NV axis is shown in dependence of the location on the sample for the times $t = 0$ ns and $t =$

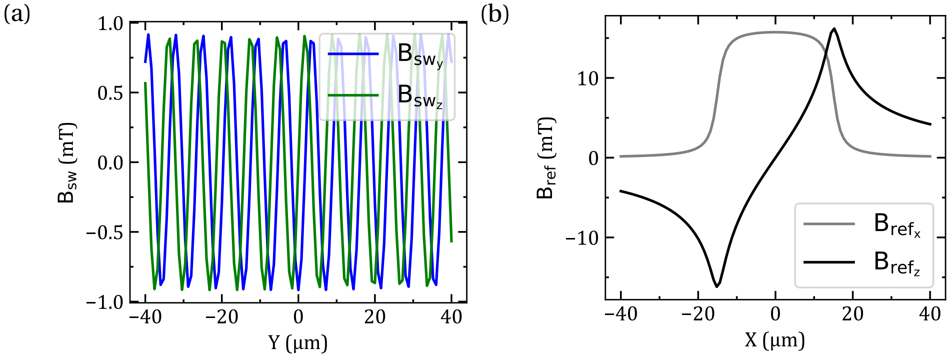

Figure 6.15.: (a) Spin wave stray field determined by Eq. 2.40 above the YIG film oscillating in the YZ-plane. (b) Oersted field of S2 defined by Eq. 2.41 oscillating in the XZ-plane.

0.6 ns in the Figs. 6.16a and 6.16b, respectively. In the simulation, S1 is oriented parallel to the X-axis with its center located outside of the simulated are area. S2 is oriented parallel to the Y-axis with its center at $X = 0$ μm. The simulated amplitude of $|B_{\text{tot},\perp}|$ is strongest directly above S2, as already observed in the measurement, since the stray field of S2 is strongest there. Furthermore, we find that the simulated magnitude of the total perpendicular field forms a standing wave, which only drives the NVs efficiently at the location of antinodes.

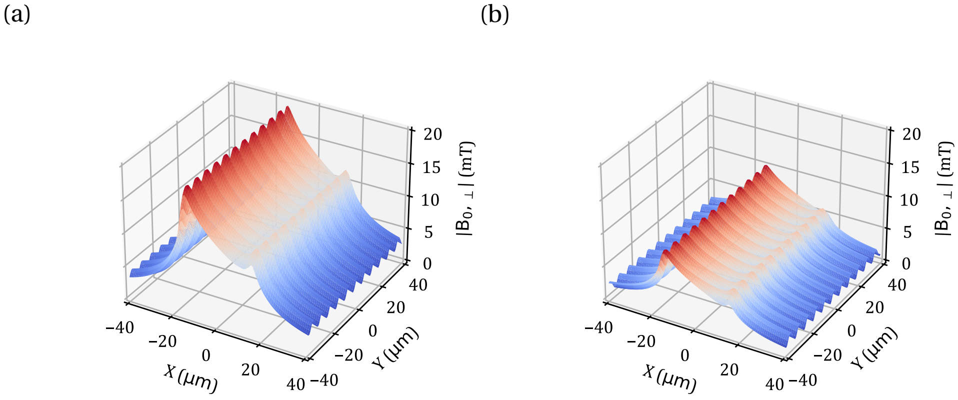

Figure 6.16.: Simulated standing wave magnitude of the total perpendicular stray field $|B_{\text{tot},\perp}|$ at the NV site at the time $t = 0$ ns (a) and $t = 0.6$ ns (b). The center of S2 is located at $X = 0$ μm. Above S2 the amplitude is increased, as the contribution from the Oersted field is strongest there.

To simulate the characteristics observed in the NV spin wave measurements, we average $|B_{\mathrm{tot},\perp}|$ over time, as we measure a time-independent PL signal at a fixed position on the sample, which scales with the magnitude of the standing wave in the total perpendicular magnetic field. In Fig. 6.17a, the simulated PL signal corresponding to the same spatial position on the sample as the measurement depicted in Fig. 6.7 is shown. The simulation reproduces the measured wave fronts in the signal and we find an enhanced contrast in the PL signal above S2, which is in agreement with the measurement. Furthermore, we find a phase shift in the wave front on the left and right side of S2. However, reproducing the bending of the wave fronts towards the center of S2 requires a more advanced model. In Fig. 6.17b, the line scans taken along the red and blue dashed vertical lines in Fig. 6.17a, are presented. We find a phase shift of 180°. The observed phase shift is attributed to the change in sign of B_{oe} from the left side to the right side of S2.

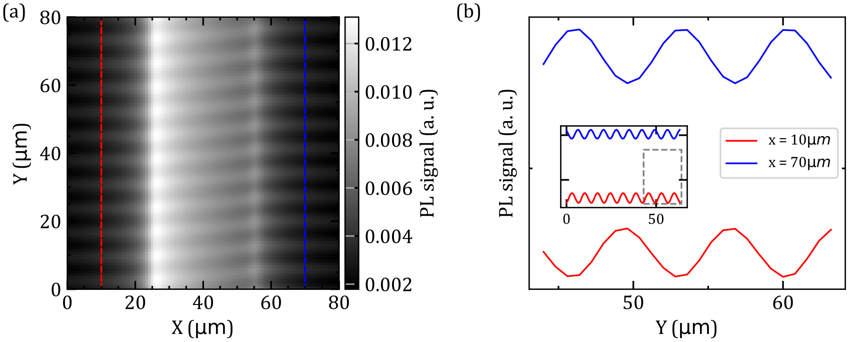

Figure 6.17.: (a) Simulated PL signal of the NVs, detecting a spin wave with frequency $f_{\mathrm{sw}} = 2.24$ GHz, corresponding to the external field $B = 22.5$ mT excited by S1. (b) Line scans taken along the vertical dashed lines in (a). The simulated phase shift between the red and blue wave front is 180°. The inset shows the whole line scan, where the dashed rectangle indicates the area of the plotted data.

6.7. CONCLUSION

In order to summarize the chapter we show a comparison of the spin wave measurement using NV centers, the simulated PL signal, and the spin wave measurement done by TR-MOKE in Fig. 6.18. The simulated PL signal in Fig. 6.18b is in good agreement with the NV spin wave measurement in Fig. 6.18a. It shows an enhanced contrast above S2 with the phase shift in the wave fronts on the left and right side of S2. Furthermore, the NV spin wave measurement is in qualitative good agreement with the TR-MOKE experiment in Fig. 6.18c, as we obtain from both experiments a similar spin wave dispersion.

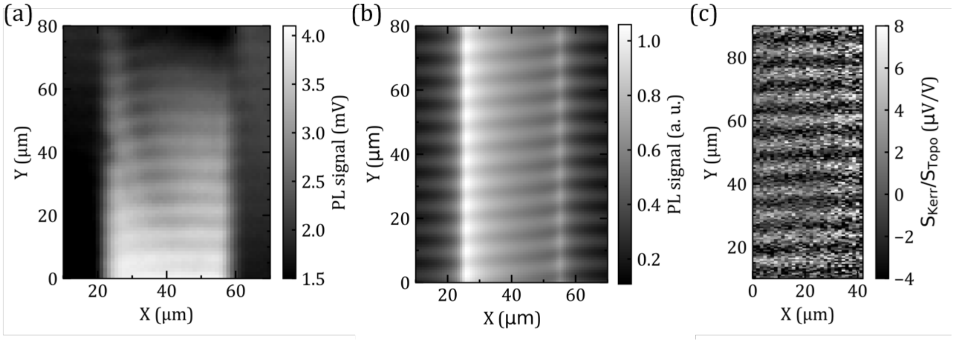

Figure 6.18.: Comparison of the spin wave measurements done with NV centers (a), the PL signal simulation (b), and the TR-MOKE measurement (c).

7

Widefield Imaging of Domains

In this chapter we investigate magnetic domains in Permalloy (Py) squares using NV center widefield imaging. These measurements were conducted as part of a master's thesis by Ankita Nayak [121] using the setup discussed in Sec. 4.4. We begin the chapter in Sec. 7.1 by introducing the sample used. In Sec. 7.2, we discuss the application of antireflection coatings to enhance the signal quality by reducing interference patterns in the imaged photoluminescence. We then continue in Sec. 7.3 to discuss the impact of strong field gradients on the magnetic resolution in NV widefield experiments. Subsequently, we present the results of imaging magnetic domains in both demagnetized and uniformly magnetized Py squares, and compare these findings with L-MOKE widefield microscopy. In Sec. 7.4, we conclude the chapter with a brief summary.

7.1. Sample

The sample used in this chapter consists of a silicon substrate with a coplanar waveguide (CPW) fabricated on it by using optical lithography and electron beam evaporation of Ti(5 nm)/Au(100 nm).

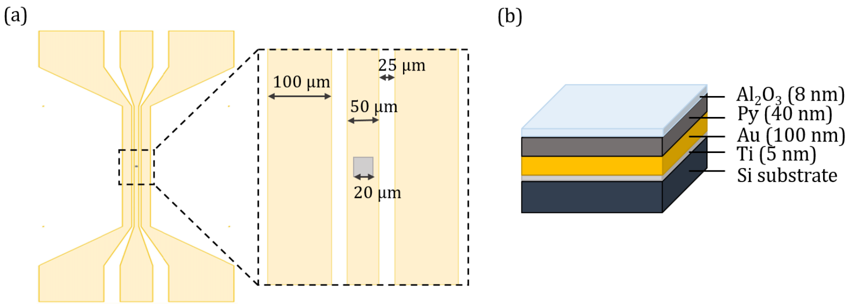

Figure 7.1.: (a) Sketch of the coplanar waveguide (CPW) fabricated on a silicon substrate. A Py square of dimensions (20 × 20 × 0.04) µm is fabricated on the 50 µm wide center strip, as depicted in the inset. (b) Layer structure of the sample, including the Py square.

The center strip of the CPW has a width of 50 µm. Additional dimensions of the CPW are shown in Fig. 7.1a. A Py square, with dimensions $(20 \times 20 \times 0.04)$ µm and an 8 nm thick Al_2O_3 capping layer, was fabricated on top of the center strip. The layers of the sample are illustrated in Fig.7.1b. For widefield imaging, the diamond chip was placed on top of the CPW with the NV layer facing towards the Py square.

7.2. ANTI-REFLECTION COATING

Improving the signal quality in widefield experiments involving ensembles of NV centers in diamond is important for enhancing the resolution and accuracy of these measurements. One factor affecting the image quality are reflections of the coherent excitation laser beam from the diamond surfaces, as shown in Fig. 7.2a. These reflections create interference patterns resulting in transverse spatial intensity variations of the excitation light at the NV layer, which induce corresponding transverse spatial variations in the NV fluorescence.

7.2.1. INTERFERENCE PATTERN

The intensity distribution of the excitation laser light I within the diamond sample resulting in the interference pattern can be modeled by considering the incident light and the effect of two internal reflections within the diamond sample [133]

$$I(r) = I_0 \left| E(r, z_1) + r_{\text{ref}}^2 E(r, z_2) + r_{\text{ref}}^4 E(r, z_3) \right|^2 . \tag{7.1}$$

Here, I_0 is a constant scaling factor, E is the electric field amplitude of a Gaussian beam, r_{ref} is the amplitude reflectivity of the air-diamond interface, r the radial distance from the center of the incident beam, and z_1, z_2, and z_3 are the longitudinal distances of the NV layer from the waist of the incident beam and the second and third reflected beams, respectively. In Fig. 7.2b, the intensity distribution simulated with Eq. 7.1 shows the characteristic interference rings, which significantly reduce the image quality in widefield measurements using coherent laser light to excite the NVs.

7.2.2. SIGNAL ENHANCEMENT USING AR COATING

In order to eliminate this interference pattern, an anti-reflection (AR) coating consisting of a thin coating layer on the top diamond surface can be used. The optimal refractive index of such a coating is given by [133]

$$n_c = \sqrt{n_d n_i}, \tag{7.2}$$

where $n_d = 2.42$ is the refractive index of diamond, and n_i is the refractive index of the medium in which the diamond/AR coating sample is placed. In our case, $n_i = 1$, as we consider a diamond-air interface. Using these values, we find that the refractive index of the AR coating should be close to $n_c = 1.56$. We chose silica (SiO_2) as the coating material because its refractive index $n_s = 1.46$ is approximately equal the desired value of n_c, and it can be easily fabricated in our lab.

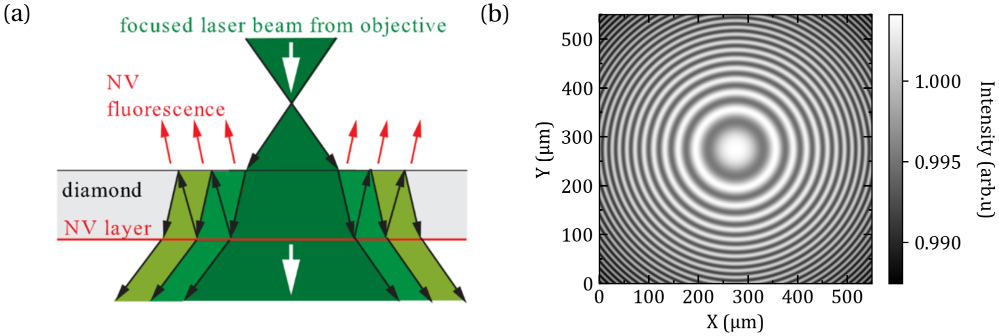

Figure 7.2.: (a) Reflections of the focused laser beam from the diamond surfaces create interference patterns, resulting in transverse spatial intensity variations of the excitation light at the thin layer of NV centers. Fig. adapted from [133]. (b) Simulated excitation profile using Eq. 7.1, showing interference rings.

To reduce the interference pattern, the fraction of light reflected from the AR-coated diamond surface at normal incidence needs to be minimized. It is given by [133]

$$R_{\mathrm{AR}} = R_{\mathrm{as}} + R_{\mathrm{sd}} + 2\sqrt{R_{\mathrm{as}} R_{\mathrm{sd}}} \cos\left(\frac{4\pi t n_s}{\lambda}\right), \tag{7.3}$$

with the Fresnel reflection coefficients at the air-silica and silica-diamond interfaces R_{as} and R_{sd}, respectively. These are given by

$$R_{\mathrm{as}} = \left(\frac{n_{\mathrm{air}} - n_{\mathrm{s}}}{n_{\mathrm{air}} + n_{\mathrm{s}}}\right)^2, \quad R_{\mathrm{sd}} = \left(\frac{n_{\mathrm{s}} - n_{\mathrm{d}}}{n_{\mathrm{s}} + n_{\mathrm{d}}}\right)^2. \tag{7.4}$$

Furthermore, t is the thickness of the silica layer and λ is the wavelength of the light. Minimizing Eq. 7.3 results in the condition $\frac{4\pi t n_s}{\lambda} = m\pi$, with m being an integer. For our AR coating layer we used the thinnest possible layer thickness given by $t = \frac{\lambda}{4n_s} = 91$ nm.

Fig. 7.3a presents the imaged PL distribution before fabricating an AR coating on the diamond and Fig. 7.3b, shows the line scan of the PL signal taken along the dashed red line in Fig. 7.3a. Clearly, the PL signal shows strong interference rings. In the Figs. 7.3c and 7.3d, we show the imaged PL spectrum and the line scan along the red dashed line, respectively, after fabricating the AR coating layer on the top diamond surface. The AR coating layer completely removed the interference pattern.

7.3. DOMAIN IMAGING

In this section, we will present our results on imaging magnetic domains in a permalloy square. The magnetic resolution of NV widefield measurements is mainly limited by the distance between the NV layer and the magnetic surface as well as by diffraction. We will first discuss the effect of strong field gradients on the magnetic resolution in NV widefield experiments and then present the measurements of a demagnetized and a

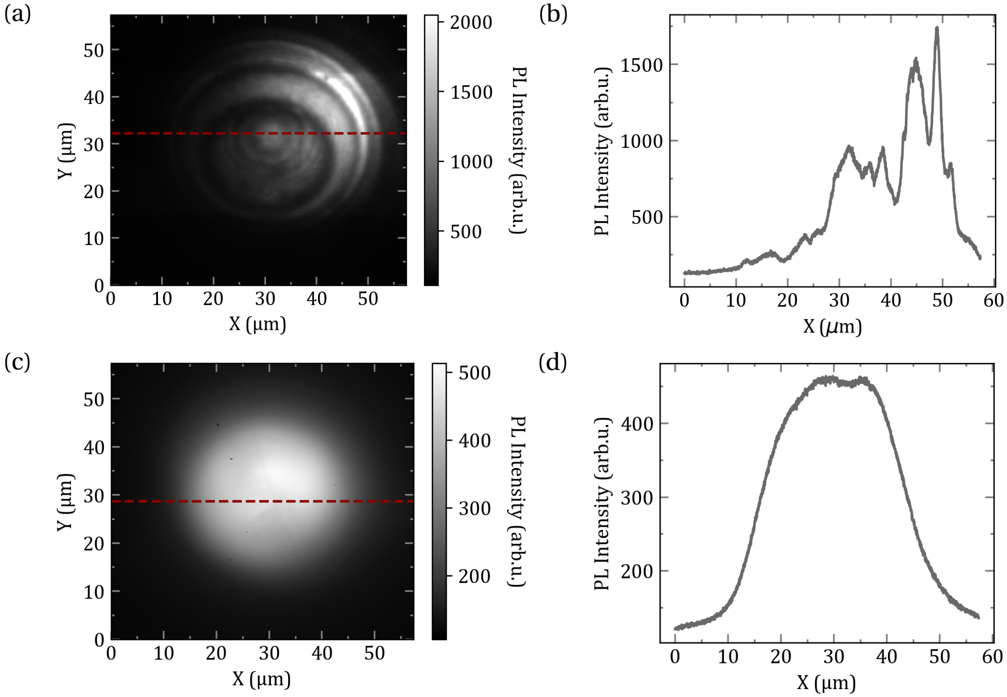

Figure 7.3.: (a) Imaged NV fluorescence distribution and line scan (b) along the red dashed line of the uncoated diamond sample, showing a characteristic interference pattern. (c) NV fluorescence distribution and line scan (d) along the red dashed line after fabricating a 91 nm thick SiO_2 layer on the top surface of the diamond. The interference pattern is completely suppressed.

uniformly magnetized Py square.

7.3.1. FIELD-AVERAGING EFFECT

In the collective measurement with an ensemble of NV centers in a diffraction-limited laser spot, a field-averaging effect can occur, if a strong field gradient exists within the laser spot. This is illustrated in Fig. 7.4a, where a magnetic sample generates magnetic fields with a large field gradient. An NV center located at the origin of the orange arrow senses a weaker field compared to an NV center located at the origin of the blue arrow. This results in two different ODMR spectra (orange and blue curves). In general, NV centers within a diffraction limited spot can thus experience a variety of fields, resulting in a broad distribution of ODMR resonances. Since it is not possible to distinguish the data from each NV center within the diffraction-limited laser spot, the PL signals from all the NV centers are simultaneously collected, producing an averaged single ODMR resonance. This is shown in Fig. 7.4b, where the dashed resonances represent the different resonance frequencies sensed within the laser spot and the blue solid line depicts the detected averaged signal. Due to the averaging effect, the magnetic field obtained from the averaged ODMR resonance is significantly reduced compared to the actual field magnitude [134]. Fig. 7.4c shows the simulated image of the measurement of a Landau domain in a magnetic square of size (1 × 1 × 0.05) µm. The simulation was conducted by Yoon et al. [134]. The magnetic square is indicated by the black dashed lines and the scale bar length is 2 µm. In the simulation the spatial resolution is assumed to be determined by the diffraction-limited laser spot size, which is approximately 1 µm and the depth of the NV centers from the diamond surface is set to 15 nm [134]. The strong field gradients result in a reduction of the measured stray fields, preventing imaging the stray fields in the center of the magnetic square.

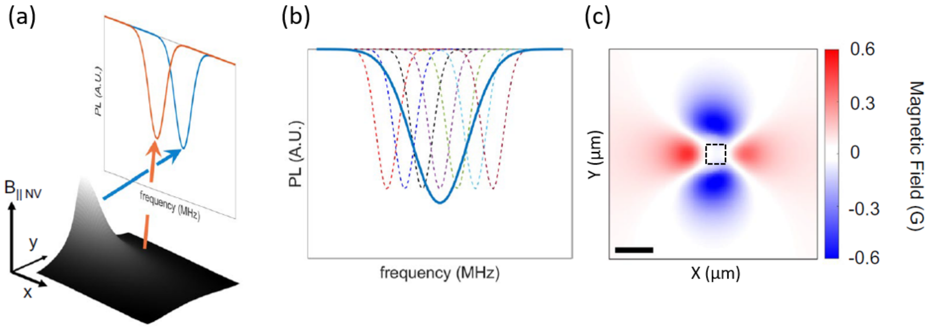

Figure 7.4.: (a) A large field gradient causes two NV centers located at the origin of the arrows to sense varying fields, resulting in two different ODMR spectra (orange and blue curves). (b) PL signals of NV centers located in a strong field gradient and within a diffraction-limited laser spot (dashed lines). In an ODMR measurement these signals are averaged (solid blue line), resulting in a reduced detected magnetic field. (c) Simulated NV widefield measurement of a Landau domain in a magnetic square of size (1 × 1 × 0.05) µm (black dashed square). Due to strong magnetic field gradients, the magnetic stray field in the center of the Landau domain cannot be imaged. The scale bar length equals 2 µm. Figure adapted from [134].

7.3.2. PERMALLOY DOMAIN MEASUREMENTS

In this section, we present domain images of a Permalloy (Py) square acquired using NV center wide field imaging and L-MOKE wide field imaging. Fig. 7.5a, shows a sketch of the magnetization orientation in a demagnetized Py square exhibiting a Landau pattern, where the red arrows indicate the direction of magnetization. When a large external field $\mathbf{B_0}$ is applied, the magnetization in the Py square becomes uniformly aligned with the external field, as schematically presented in Fig. 7.5d.

To image the Landau pattern with the widefield NV setup, a small bias field $\mathbf{B_0}$ was applied along the direction of an NV axis that lies in the XZ-plane, forming an angle of $\theta = 35°$ with the X-axis, as indicated in Fig. 7.5a. The ODMR spectrum was recorded

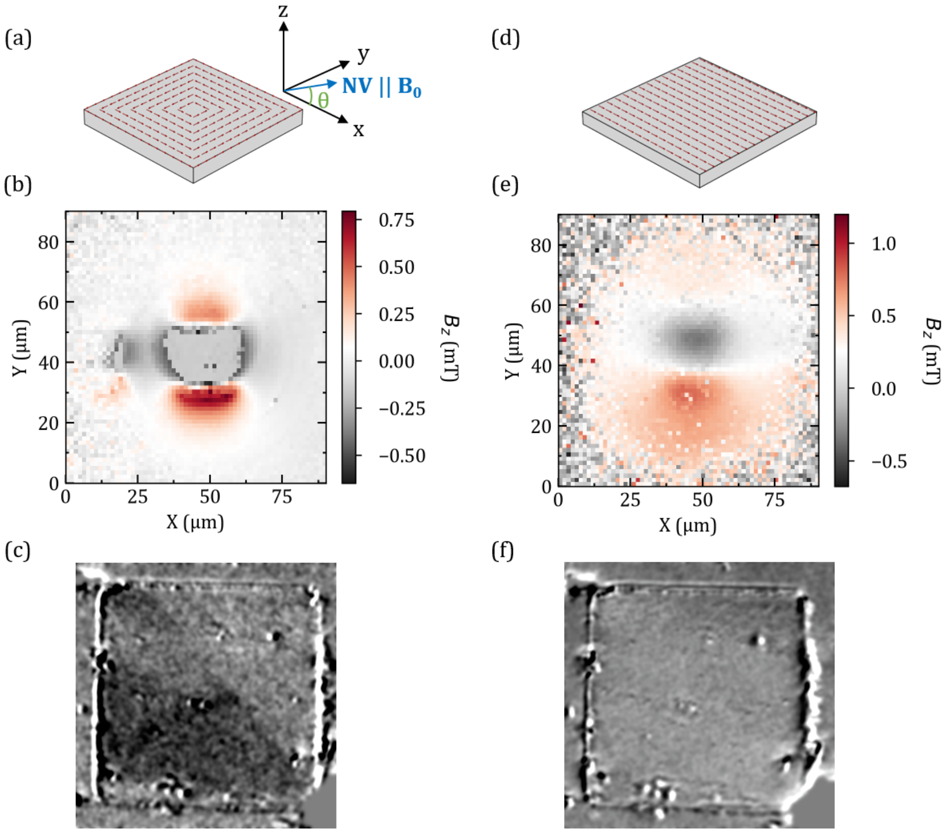

Figure 7.5.: Magnetic domains in a Py square with dimensions (20 × 20 × 0.04) µm. (a) Sketch of the magnetization orientation (red arrows) in a Landau pattern. (b) NV widefield imaging of the Landau pattern. Due to the field-averaging effect, the stray fields in the middle of the square cannot be resolved. (c) L-MOKE image of the Py square, showing a Landau domain state. (d) Sketch of the magnetization orientation (red arrows) in a uniformly magnetized Py square. (e) NV widefield imaging of a uniformly magnetized Py square. The stray field can be fully imaged, as there are no strong field gradients. (f) L-MOKE image of the uniformly magnetized Py square.

by sweeping the excitation frequency and capturing an image with the camera for each frequency. These images where then split into cells of size (1.4 × 1.4) μm. For each cell, the magnetic field magnitude along the NV-direction was calculated by fitting the outer dips of the ODMR spectrum to obtain the resonance frequencies. Using Eq. 3.6, the total magnetic field amplitude along the aligned NV center $B_{\mathrm{NV_{tot}}} = B_0 + B_{\mathrm{Py}}$ for each cell was calculated. To determine the amplitude of the external field along the aligned NV axis, the ODMR spectra at the left and right sides of the image, that are far away from the Py square, were fitted and the obtained fields were averaged. This resulted in $B_0 = 12.3$ mT. The stray field of the Py square along the NV axis was then calculated by subtracting the external field B_0 from the total field $B_{\mathrm{NV}_{\mathrm{tot}}}$.

In Fig. 7.5b, the obtained image is presented. Due to the field-averaging effect, the stray fields in the middle of the Py square cannot be resolved. Furthermore, the measurement was conducted using a diamond without an AR coating. Thus, the interference patterns in the emitted fluorescence appear as circular patterns in the background of the stray field image of the Py square. We find, that the obtained stray field image is in good agreement with the simulation in Fig. 7.4c. Fig. 7.5c displays an L-MOKE image of the Py square, where a bias field of $B_0 = 7$ mT was applied in the Py square plane, confirming the detected Landau domain structure.

To demonstrate the transition of the demagnetized Py square exhibiting the Landau pattern to a uniformly magnetized state, a stronger external field of $B_0 > 20$ mT was applied. The NV widefield imaging results for the uniformly magnetized Py square are shown in Fig. 7.5e. In this case, the stray field can be fully imaged because there are no strong field gradients caused by domains. Finally, Fig. 7.5f shows an L-MOKE image of the uniformly magnetized Py square. This image confirms the uniform magnetization state, with no visible domain structures.

7.4. SUMMARY

In summary, this chapter presented NV center and L-MOKE widefield imaging of magnetic domains in Py squares. To improve the signal quality in the NV measurements anti-reflection coatings consisting of thin SiO_2 layers were fabricated on the diamond surface. In the Landau domain imaging experiments using NV centers, strong field gradients caused significant reduction in the measured magnetic field magnitude and resolution due to the field-averaging effect. This effect did not appear in uniformly magnetized samples, where the stray field could be fully imaged. In contrast, L-MOKE imaging provided a detailed visualization of the magnetic domains. However, with NV centers it is technically possible to gain the 3D vector magnetic stray field of the sample, which is not feasible in L-MOKE measurements.

8

CONCLUSION

The aim of this thesis was to image spin waves with NV centers in diamond as well as to establish NV center sensing and imaging techniques within this research group. To achieve this, three distinct NV center setups were developed during the course of the project.

In Chapter 4, the implementation of these setups was discussed. The first setup was a confocal NV center microscope equipped with a lock-in amplifier to enhance the signal-to-noise ratio in magnetometry measurements. The second setup consisted of a combined confocal NV center and time-resolved magneto-optical Kerr effect (TR-MOKE) microscope. It was built with the long term goal of imaging spin waves with both techniques simultaneously. The third setup was a widefield NV center microscope, which was built for fast data acquisition.

In Chapter 5, preliminary measurements for the characterization of the diamond samples as well as the optimization of the measurement parameters were discussed. We began by introducing the details about the diamond substrate, including the parameters for ion implantation and the annealing process. We then investigated the dependence of the PL signal on the microwave power. Next, we conducted static magnetic field sensing experiments, examining how the ODMR signal splits under the influence of an external magnetic field and we determined the amplitude of this external field. By adjusting the polarization direction of the excitation laser light, we demonstrated the dependence of the contrast in the ODMR spectrum on the polarization direction. We also demonstrated the coherent control of NV centers through pulsed measurement techniques, including T_1 relaxation measurements and Rabi oscillation experiments. These findings layed the groundwork for the experimental techniques and results discussed in the subsequent chapters.

In Chapter 6, we used shallowly implanted NV centers to measure spin waves in yttrium iron garnet (YIG) thin films. We first determined the distance between the NV layer and the YIG surface, an important parameter for accurately calculating the amplitude of the spin waves stray field. This was achieved through the 3D vector field reconstruction of the magnetic field generated by a DC current. We then discussed the detection of spin waves through their stray fields using NV centers. By creating a standing wave in the total stray field at the NV layer, we demonstrated the imaging of individual wave fronts of spin waves. We also determined the spin wave dispersion from these measurements. A comparative analysis was conducted between the NV center spin wave measurements and spin wave imaging performed using TR-MOKE. The results from both techniques were found to be consistent, highlighting the reliability of NV center-based measurements. To further understand the observed features in the NV spin wave images, we simulated the NV spin wave measurements with a phenomenological model.

In Chapter 7, we explored the use of NV center widefield imaging to investigate magnetic domains in Permalloy (Py) squares. A significant challenge in these experiments was the interference pattern caused by reflections of the excitation laser beam within the diamond. To mitigate this, we applied a thin silica AR coating to the diamond surface, effectively reducing these reflections and enhancing the homogeneity of the illumination, which in turn improved the quality of the photoluminescence signal. We then examined the impact of strong field gradients on the magnetic resolution in NV widefield imaging. These gradients cause a field averaging effect, reducing the detected magnetic field magnitude. This effect was evident in our imaging of the Landau domain pattern in a demagnetized Py square, where the strong gradients made it difficult to resolve the stray fields at the center of the square. Our results were compared with longitudinal magneto-optic Kerr effect (L-MOKE) imaging. While NV widefield imaging struggled with strong field gradients, L-MOKE provided clear images of the magnetic domains. However, NV center imaging has the advantage of potentially capturing the 3D vector magnetic stray field, unlike L-MOKE which is limited to 2D surface measurements. Finally, we demonstrated the transition from demagnetized to uniformly magnetized states in the Py squares by applying an external magnetic field. In the uniformly magnetized state, the NV widefield imaging successfully resolved the stray fields without the interference of strong gradients, confirming the uniform magnetization seen in L-MOKE images.

To summarize, we find that the utilization of NV centers presents several advantages in the measurement of spin waves. Their ability to measure through opaque materials offers unique opportunities for non-invasive investigation [58, 59]. Additionally, NV centers exhibit remarkable sensitivity to magnetic fields, enhancing their utility in detecting subtle magnetic variations. Moreover, their high resolution capabilities extend beyond the diffraction limit, potentially enabling precise characterization of spin wave phenomena. However, it is worth noting some limitations of NV centers, including the lack of time resolution and the requirement of a standing wave for effectively imaging wave fronts. Additionally, NV centers are limited to probing only spin waves at the NV ESR frequencies. In comparison, Kerr microscopy offers high time resolution and the flexibility to probe a wide range of frequencies. However, TR-MOKE cannot image spin waves trough opaque materials thicker then the skin depth, and the spatial resolution is ultimately limited by diffraction.

To fully exploit the complementary strengths of both techniques, we initiated to implement a setup that combines both approaches. By integrating NV center measurements with time-resolved Kerr microscopy, it is possible to benefit from high-resolution imaging, probing through opaque materials, high sensitivity to magnetic fields, high time resolution, and flexibility in probing frequencies. This integrated approach promises to advance the capability to probe spin wave dynamics and enable new insights in the field. To do simultaneous spin wave imaging with both techniques, a few improvements may be employed. A better shielding of the setup from surrounding stray light and the use of an avalanche photodiode for the detection of the photoluminescence signal could be implemented to increase the contrast in the measurements. An improvement in measurement time may be realized by using the widefield setup for spin wave imaging. This might be accomplished by integrating a lock-in amplified camera in the widefield setup.

To conclude, NV center microscopy emerges as a powerful new technique for studying spin waves, providing valuable insights into magnon transport that are inaccessible through other experimental methods.

BIBLIOGRAPHY

[1] A. Mahmoud, F. Ciubotaru, F. Vanderveken, A. V. Chumak, S. Hamdioui, C. Adelmann, and S. Cotofana. "Introduction to spin wave computing". In: *Journal of Applied Physics* 128.16 (2020), p. 161101. ISSN: 0021-8979. DOI: 10.1063/5.0019328.

[2] R. L. Boylestad and L. Nashelsky. *Electronic Devices and Circuit Theory*. 11th. Pearson, Harlow, 2014.

[3] S. M. Sze and K. K. Ng. *Physics of Semiconductor Devices*. 3th. Wiley, Hoboken, 2006.

[4] B. Lojek. *History of Semiconductor Engineering*. Springer, Berlin, 2007.

[5] G. E. Moore. "Cramming More Components Onto Integrated Circuits". In: *Proceedings of the IEEE* 86.1 (1998), pp. 82–85. ISSN: 0018-9219. DOI: 10.1109/JPROC.1998.658762.

[6] K. Bernstein, R. K. Cavin, W. Porod, A. Seabaugh, and J. Welser. "Device and Architecture Outlook for Beyond CMOS Switches". In: *Proceedings of the IEEE* 98.12 (2010), pp. 2169–2184. ISSN: 0018-9219. DOI: 10.1109/JPROC.2010.2066530.

[7] G. Bourianoff. "The future of nanocomputing". In: *Computer* 36.8 (2003), pp. 44–53. ISSN: 0018-9162. DOI: 10.1109/MC.2003.1220581.

[8] G. I. Bourianoff, P. A. Gargini, and D. E. Nikonov. "Research directions in beyond CMOS computing". In: *Solid-State Electronics* 51.11-12 (2007), pp. 1426–1431. ISSN: 0038-1101. DOI: 10.1016/j.sse.2007.09.018.

[9] Feitelson D. G. *Optical Computing*. 1988.

[10] J. A. Hutchby, G. I. Bourianoff, V. V. Zhirnov, and J. E. Brewer. "Extending the road beyond CMOS". In: *IEEE Circuits and Devices Magazine* 18.2 (2002), pp. 28–41. ISSN: 8755-3996. DOI: 10.1109/101.994856.

[11] D. A. B. Miller. "Are optical transistors the logical next step?" In: *Nature Photonics* 4.1 (2010), pp. 3–5. ISSN: 1749-4885. DOI: 10.1038/nphoton.2009.240.

[12] D. E. Nikonov and I. A. Young. "Overview of Beyond-CMOS Devices and a Uniform Methodology for Their Benchmarking". In: *Proceedings of the IEEE* 101.12 (2013), pp. 2498–2533. ISSN: 0018-9219. DOI: 10.1109/JPROC.2013.2252317.

[13] D. E. Nikonov and I. A. Young. "Benchmarking spintronic logic devices based on magnetoelectric oxides". In: *Journal of Materials Research* 29.18 (2014), pp. 2109–2115. ISSN: 0884-2914. DOI: 10.1557/jmr.2014.243.

[14] D. E. Nikonov and I. A. Young. “Benchmarking of Beyond-CMOS Exploratory Devices for Logic Integrated Circuits”. In: *IEEE Journal on Exploratory Solid-State Computational Devices and Circuits* 1 (2015), pp. 3–11. ISSN: 2329-9231. DOI: `10.1109/JXCDC.2015.2418033`.

[15] N. Streibl, K.-H. Brenner, A. Huang, J. Jahns, J. Jewell, A. W. Lohmann, D. Miller, M. Murdocca, M. E. Prise, and T. Sizer. “Digital optics”. In: *Proceedings of the IEEE* 77.12 (1989), pp. 1954–1969. ISSN: 0018-9219. DOI: `10.1109/5.48834`.

[16] A. V. Chumak, V. I. Vasyuchka, A. A. Serga, and B. Hillebrands. “Magnon spintronics”. In: *Nature Physics* 11.6 (2015), pp. 453–461. ISSN: 1745-2473. DOI: `10.1038/nphys3347`.

[17] K.-S. Lee and S.-K. Kim. “Conceptual design of spin wave logic gates based on a Mach–Zehnder-type spin wave interferometer for universal logic functions”. In: *Journal of Applied Physics* 104.5 (2008), p. 053909. ISSN: 0021-8979. DOI: `10.1063/1.2975235`.

[18] A. V. Chumak, A. A. Serga, and B. Hillebrands. “Magnon transistor for all-magnon data processing”. In: *Nature communications* 5 (2014), p. 4700. DOI: `10.1038/ncomms5700`.

[19] S. Klingler, H. Maier-Flaig, C. Dubs, O. Surzhenko, R. Gross, H. Huebl, S. T. B. Goennenwein, and M. Weiler. “Gilbert damping of magnetostatic modes in a yttrium iron garnet sphere”. In: *Applied Physics Letters* 110.9 (2017), p. 092409. ISSN: 0003-6951. DOI: `10.1063/1.4977423`.

[20] A. A. Serga, A. V. Chumak, and B. Hillebrands. “YIG magnonics”. In: *Journal of Physics D: Applied Physics* 43.26 (2010), p. 264002. ISSN: 0022-3727. DOI: `10.1088/0022-3727/43/26/264002`.

[21] K. Ganzhorn, S. Klingler, T. Wimmer, S. Geprägs, R. Gross, H. Huebl, and S. T. B. Goennenwein. “Magnon-based logic in a multi-terminal YIG/Pt nanostructure”. In: *Applied Physics Letters* 109.2 (2016), p. 022405. ISSN: 0003-6951. DOI: `10.1063/1.4958893`.

[22] S. Klingler, P. Pirro, T. Brächer, B. Leven, B. Hillebrands, and A. V. Chumak. “Spin-wave logic devices based on isotropic forward volume magnetostatic waves”. In: *Applied Physics Letters* 106.21 (2015), p. 212406. ISSN: 0003-6951. DOI: `10.1063/1.4921850`.

[23] K. Uchida, S. Takahashi, K. Harii, J. Ieda, W. Koshibae, K. Ando, S. Maekawa, and E. Saitoh. “Observation of the spin Seebeck effect”. In: *Nature* 455.7214 (2008), pp. 778–781. DOI: `10.1038/nature07321`.

[24] V. V. Kruglyak, S. O. Demokritov, and D. Grundler. “Magnonics”. In: *Journal of Physics D: Applied Physics* 43.26 (2010), p. 264001. ISSN: 0022-3727. DOI: `10.1088/0022-3727/43/26/264001`.

[25] B. Lenk, H. Ulrichs, F. Garbs, and M. Münzenberg. “The building blocks of magnonics”. In: *Physics Reports* 507.4-5 (2011), pp. 107–136. ISSN: 03701573. DOI: `10.1016/j.physrep.2011.06.003`.

[26] L. Bonneviot and D. Olivier. “Ferromagnetic Resonance”. In: *Catalyst Characterization*. Ed. by M. V. Twigg, M. S. Spencer, B. Imelik, and J. C. Vedrine. Fundamental and Applied Catalysis. Boston, MA: Springer US, 1994, pp. 181–214. ISBN: 978-1-4757-9591-2. DOI: `10.1007/978-1-4757-9589-9{\textunderscore}7`.

[27] K. Ando, J. Ieda, K. Sasage, S. Takahashi, S. Maekawa, and E. Saitoh. “Electric detection of spin wave resonance using inverse spin-Hall effect”. In: *Applied Physics Letters* 94.26 (2009), p. 262505. ISSN: 0003-6951. DOI: `10.1063/1.3167826`.

[28] M. Balinskiy, H. Chiang, D. Gutierrez, and A. Khitun. “Spin wave interference detection via inverse spin Hall effect”. In: *Applied Physics Letters* 118.24 (2021), p. 242402. ISSN: 0003-6951. DOI: `10.1063/5.0055402`.

[29] S. V. Grigoriev, A. S. Sukhanov, E. V. Altynbaev, S.-A. Siegfried, A. Heinemann, P. Kizhe, and S. V. Maleyev. “Spin waves in full-polarized state of Dzyaloshinskii-Moriya helimagnets: Small-angle neutron scattering study”. In: *Phys. Rev. B* 92 (22 2015), p. 220415. DOI: `10.1103/PhysRevB.92.220415`.

[30] M. T. Hutchings and E. J. Samuelsen. “Measurement of Spin-Wave Dispersion in NiO by Inelastic Neutron Scattering and Its Relation to Magnetic Properties”. In: *Physical Review B* 6.9 (1972), pp. 3447–3461. ISSN: 1098-0121. DOI: `10.1103/PhysRevB.6.3447`.

[31] J. S. Plant. “Spinwave dispersion curves for yttrium iron garnet”. In: *Journal of Physics C: Solid State Physics* 10.23 (1977), pp. 4805–4814. ISSN: 0022-3719. DOI: `10.1088/0022-3719/10/23/014`.

[32] D. Betto, Y. Y. Peng, S. B. Porter, G. Berti, A. Calloni, G. Ghiringhelli, and N. B. Brookes. “Three-dimensional dispersion of spin waves measured in NiO by resonant inelastic x-ray scattering”. In: *Physical Review B* 96.2 (2017). ISSN: 1098-0121. DOI: `10.1103/PhysRevB.96.020409`.

[33] B. W. Lebert, M. P. M. Dean, A. Nicolaou, J. Pelliciari, M. Dantz, T. Schmitt, R. Yu, M. Azuma, J.-P. Castellan, H. Miao, A. Gauzzi, B. Baptiste, and M. d’Astuto. “Resonant inelastic x-ray scattering study of spin-wave excitations in the cuprate parent compound Ca2CuO2Cl2”. In: *Physical Review B* 95.15 (2017). ISSN: 1098-0121. DOI: `10.1103/PhysRevB.95.155110`.

[34] S. Tóth, B. Wehinger, K. Rolfs, T. Birol, U. Stuhr, H. Takatsu, K. Kimura, T. Kimura, H. M. Rønnow, and C. Rüegg. “Electromagnon dispersion probed by inelastic X-ray scattering in LiCrO2”. In: *Nature communications* 7 (2016), p. 13547. DOI: `10.1038/ncomms13547`.

[35] S. Demokritov. “Brillouin light scattering studies of confined spin waves: linear and nonlinear confinement”. In: *Physics Reports* 348.6 (2001), pp. 441–489. ISSN: 03701573. DOI: `10.1016/S0370-1573(00)00116-2`.

[36] T. Sebastian, K. Schultheiss, B. Obry, B. Hillebrands, and H. Schultheiss. “Microfocused Brillouin light scattering: imaging spin waves at the nanoscale”. In: *Frontiers in Physics* 3 (2015). DOI: `10.3389/fphy.2015.00035`.

[37] A. A. Serga, T. Schneider, B. Hillebrands, S. O. Demokritov, and M. P. Kostylev. "Phase-sensitive Brillouin light scattering spectroscopy from spin-wave packets". In: *Applied Physics Letters* 89.6 (2006), p. 063506. ISSN: 0003-6951. DOI: `10.1063/1.2335627`.

[38] J. L. Erskine and E. A. Stern. "Magneto-optic Kerr Effect in Ni, Co, and Fe". In: *Physical Review Letters* 30.26 (1973), pp. 1329–1332. ISSN: 0031-9007. DOI: `10.1103/PhysRevLett.30.1329`.

[39] Z. Q. Qiu and S. D. Bader. "Surface magneto-optic Kerr effect". In: *Review of Scientific Instruments* 71.3 (2000), pp. 1243–1255. ISSN: 0034-6748. DOI: `10.1063/1.1150496`.

[40] M. W. Doherty, N. B. Manson, P. Delaney, F. Jelezko, J. Wrachtrup, and L. C. Hollenberg. "The nitrogen-vacancy colour centre in diamond". In: *Physics Reports* 528.1 (2013), pp. 1–45. ISSN: 03701573. DOI: `10.1016/j.physrep.2013.02.001`.

[41] F. Jelezko and J. Wrachtrup. "Single defect centres in diamond: A review". In: *physica status solidi (a)* 203.13 (2006), pp. 3207–3225. ISSN: 18626300. DOI: `10.1002/pssa.200671403`.

[42] J. R. Maze, P. L. Stanwix, J. S. Hodges, S. Hong, J. M. Taylor, P. Cappellaro, L. Jiang, M. V. G. Dutt, E. Togan, A. S. Zibrov, A. Yacoby, R. L. Walsworth, and M. D. Lukin. "Nanoscale magnetic sensing with an individual electronic spin in diamond". In: *Nature* 455.7213 (2008), pp. 644–647. DOI: `10.1038/nature07279`.

[43] F. Jelezko, T. Gaebel, I. Popa, A. Gruber, and J. Wrachtrup. "Observation of coherent oscillations in a single electron spin". In: *Physical Review Letters* 92.7 (2004), p. 076401. ISSN: 1079-7114. DOI: `10.1103/PhysRevLett.92.076401`.

[44] G. e. a. Balasubramanian. "Ultralong spin coherence time in isotopically engineered diamond". In: *Nature materials* 8.5 (2009), pp. 383–387. ISSN: 1476-4660. DOI: `10.1038/nmat2420`. URL: `https://pubmed.ncbi.nlm.nih.gov/19349970/`.

[45] L. Rondin, J.-P. Tetienne, T. Hingant, J.-F. Roch, P. Maletinsky, and V. Jacques. "Magnetometry with nitrogen-vacancy defects in diamond". In: *Reports on prog. in physics. Physical Society (Great Britain)* 77.5 (2014), p. 056503. DOI: `10.1088/0034-4885/77/5/056503`.

[46] G. Balasubramanian, I. Y. Chan, R. Kolesov, M. Al-Hmoud, J. Tisler, C. Shin, C. Kim, A. Wojcik, P. R. Hemmer, A. Krueger, T. Hanke, A. Leitenstorfer, R. Bratschitsch, F. Jelezko, and J. Wrachtrup. "Nanoscale imaging magnetometry with diamond spins under ambient conditions". In: *Nature* 455.7213 (2008), pp. 648–651. DOI: `10.1038/nature07278`.

[47] C. L. Degen. "Scanning magnetic field microscope with a diamond single-spin sensor". In: *Applied Physics Letters* 92.24 (2008), p. 243111. ISSN: 0003-6951. DOI: `10.1063/1.2943282`.

[48] J. M. Taylor, P. Cappellaro, L. Childress, L. Jiang, D. Budker, P. R. Hemmer, A. Yacoby, R. Walsworth, and M. D. Lukin. “Erratum: High-sensitivity diamond magnetometer with nanoscale resolution”. In: *Nature Physics* 7.3 (2011), p. 270. ISSN: 1745-2473. DOI: 10.1038/nphys1937.

[49] B. J. e. a. Maertz. “Vector magnetic field microscopy using nitrogen vacancy centers in diamond”. In: *Applied Physics Letters* 96.9 (2010), p. 092504. ISSN: 0003-6951. DOI: 10.1063/1.3337096.

[50] C. A. Meriles, L. Jiang, G. Goldstein, J. S. Hodges, J. Maze, M. D. Lukin, and P. Cappellaro. “Imaging mesoscopic nuclear spin noise with a diamond magnetometer”. In: *The Journal of Chemical Physics* 133.12 (2010), p. 124105. ISSN: 1089-7690. DOI: 10.1063/1.3483676.

[51] S. Steinert, F. Dolde, P. Neumann, A. Aird, B. Naydenov, G. Balasubramanian, F. Jelezko, and J. Wrachtrup. “High sensitivity magnetic imaging using an array of spins in diamond”. In: *Review of Scientific Instruments* 81.4 (2010), p. 043705. ISSN: 1089-7623. DOI: 10.1063/1.3385689.

[52] A. Laraoui, J. S. Hodges, and C. A. Meriles. “Magnetometry of random ac magnetic fields using a single nitrogen-vacancy center”. In: *Applied Physics Letters* 97.14 (2010), p. 143104. ISSN: 0003-6951. DOI: 10.1063/1.3497004.

[53] N. Zhao, J.-L. Hu, S.-W. Ho, J. T. K. Wan, and R. B. Liu. “Atomic-scale magnetometry of distant nuclear spin clusters via nitrogen-vacancy spin in diamond”. In: *Nature Nanotechnology* 6.4 (2011), pp. 242–246. ISSN: 1748-3395. DOI: 10.1038/nnano.2011.22.

[54] K. Hayashi, Y. Matsuzaki, T. Taniguchi, T. Shimo-Oka, I. Nakamura, S. Onoda, T. Ohshima, H. Morishita, M. Fujiwara, S. Saito, and N. Mizuochi. “Optimization of Temperature Sensitivity Using the Optically Detected Magnetic-Resonance Spectrum of a Nitrogen-Vacancy Center Ensemble”. In: *Physical Review Applied* 10.3 (2018). DOI: 10.1103/PhysRevApplied.10.034009.

[55] V. M. Acosta, E. Bauch, M. P. Ledbetter, A. Waxman, L.-S. Bouchard, and D. Budker. “Temperature dependence of the nitrogen-vacancy magnetic resonance in diamond”. In: *Physical Review Letters* 104.7 (2010), p. 070801. ISSN: 1079-7114. DOI: 10.1103/PhysRevLett.104.070801.

[56] C. M. Purser, V. P. Bhallamudi, F. Guo, M. R. Page, Q. Guo, G. D. Fuchs, and P. C. Hammel. “Spinwave detection by nitrogen-vacancy centers in diamond as a function of probe–sample separation”. In: *Applied Physics Letters* 116.20 (2020). ISSN: 0003-6951. DOI: 10.1063/1.5141921.

[57] I. Bertelli, J. J. Carmiggelt, T. Yu, B. G. Simon, C. C. Pothoven, G. E. W. Bauer, Y. M. Blanter, J. Aarts, and T. van der Sar. “Magnetic resonance imaging of spin-wave transport and interference in a magnetic insulator”. In: *Science advances* 6.46 (2020). DOI: 10.1126/sciadv.abd3556.

[58] I. Bertelli, B. G. Simon, T. Yu, J. Aarts, G. E. W. Bauer, Y. M. Blanter, and T. van der Sar. “Imaging Spin–Wave Damping Underneath Metals Using Electron Spins in Diamond”. In: *Advanced Quantum Technologies* 4.12 (2021). ISSN: 2511-9044. DOI: 10.1002/qute.202100094.

[59] M. Borst, P. H. Vree, A. Lowther, A. Teepe, S. Kurdi, I. Bertelli, B. G. Simon, Y. M. Blanter, and T. van der Sar. "Observation and control of hybrid spin-wave-Meissner-current transport modes". In: *Science (New York, N.Y.)* 382.6669 (2023), pp. 430–434. DOI: 10.1126/science.adj7576.

[60] A. Finco, A. Haykal, R. Tanos, F. Fabre, S. Chouaieb, W. Akhtar, I. Robert-Philip, W. Legrand, F. Ajejas, K. Bouzehouane, N. Reyren, T. Devolder, J.-P. Adam, J.-V. Kim, V. Cros, and V. Jacques. "Imaging non-collinear antiferromagnetic textures via single spin relaxometry". In: *Nature communications* 12.1 (2021), p. 767. DOI: 10.1038/s41467-021-20995-x.

[61] A. G. Gurevich and G. A. Melkov. *Magnetization Oscillations and Waves*. CRC Press, 2020. ISBN: 9780138748487. DOI: 10.1201/9780138748487.

[62] S. Blundell. *Magnetism in condensed matter*. Reprint. Vol. 4. Oxford master series in cond. matter physics. Oxford: Oxford Univ. Press, 2014. ISBN: 9780198505914.

[63] S. Chikazumi and C. D. Graham, eds. *Physics of ferromagnetism*. 2. ed., 1. publ. in paperback, Repr. with corrections. Vol. 94. International series of monographs on physics. Oxford: Oxford University Press, 2010. ISBN: 9780199564811.

[64] T. Miyazaki and H. Jin. *The Physics of Ferromagnetism*. Vol. 158. Berlin, Heidelberg: Springer Berlin Heidelberg, 2012. ISBN: 978-3-642-25582-3. DOI: 10.1007/978-3-642-25583-0.

[65] H. Haken and H. C. Wolf. *Atom- und Quantenphysik: Einführung in die experimentellen und theoretischen Grundlagen*. Achte, aktualisierte und erweiterte Auflage. Berlin and Heidelberg: Springer, 2004. ISBN: 9783540026211. DOI: 10.1007/978-3-642-18519-9.

[66] B. A. Kalinikos and A. N. Slavin. "Theory of dipole-exchange spin wave spectrum for ferromagnetic films with mixed exchange boundary conditions". In: *Journal of Physics C: Solid State Physics* 19.35 (1986), pp. 7013–7033. ISSN: 0022-3719. DOI: 10.1088/0022-3719/19/35/014.

[67] C. Kittel. "On the Theory of Ferromagnetic Resonance Absorption". In: *Physical Review* 73.2 (1948), pp. 155–161. ISSN: 0031-899X. DOI: 10.1103/PhysRev.73.155.

[68] T. L. Gilbert. "Classics in Magnetics A Phenomenological Theory of Damping in Ferromagnetic Materials". In: *IEEE Transactions on Magnetics* 40.6 (2004), pp. 3443–3449. ISSN: 0018-9464. DOI: 10.1109/TMAG.2004.836740.

[69] W. Heisenberg. "Zur Theorie des Ferromagnetismus". In: *Zeitschrift fr Physik* 49.9-10 (1928), pp. 619–636. ISSN: 1434-6001. DOI: 10.1007/BF01328601.

[70] I. Bertelli. "Magnetic imaging of spin waves and magnetic phase transitions with nitrogen-vacancy centers in diamond". PhD thesis. Technische Universität Leiden, 2021.

[71] L. Flacke. "Spin-wave transport and skyrmion formation in CoFe-based thin film heterostructures". PhD thesis. Technische Universität München, 2022.

[72] S. Klingler. "Magnetization dynamics in coupled magnetic systems". PhD thesis. Technische Universität München, 2019.

[73] M. Buess. “Pulsed Precessional Motion”. PhD thesis. Eidgenössische Technische Universität Zürich, 2005.

[74] R. Huber. “Control of Spin Waves on the Nanoscale in One-Dimensional Magnonic Crystals and Atomic Layer Deposition of Metallic Ferromagnets for Second Generation of Nanomaterials”. PhD thesis. Technische Universität München, 2013.

[75] P. Eib. “Magnetic domain wall motion in the presence of defects: Experiments and simulations”. PhD thesis. Eidgenössische Technische Universität Zürich, 2015.

[76] T. Meier. “Static and dynamic properties of chiral magnetic textures in systems with broken inversion symmetry”. PhD thesis. Universität Regensburg, 2018.

[77] J. M. D. Coey. *Magnetism and Magnetic Materials.* Cambridge University Press, 2012. ISBN: 9780521016766. DOI: `10.1017/CBO9780511845000`.

[78] K. Shinagawa. “Faraday and Kerr Effects in Ferromagnets”. In: *Magneto-Optics.* Ed. by S. Sugano and N. Kojima. Vol. 128. Springer Series in Solid-State Sciences. Berlin and Heidelberg: Springer, 2000, pp. 137–177. ISBN: 978-3-642-08523-9. DOI: `10.1007/978-3-662-04143-7{\textunderscore}5`.

[79] A. Hubert and R. Schäfer. *Magnetic domains: The analysis of magnetic microstructures.* Corr. print., [Nachdr.] Berlin: Springer, 2011. ISBN: 3540641084.

[80] L. LANDAU and E. LIFSHITZ. “On the theory of the dispersion of magnetic permeability in ferromagnetic bodies”. In: *Perspectives in Theoretical Physics.* Elsevier, 1992, pp. 51–65. ISBN: 9780080363646. DOI: `10.1016/B978-0-08-036364-6.50008-9`.

[81] D. Polder. “VIII. On the theory of ferromagnetic resonance”. In: *The London, Edinburgh, and Dublin Philosophical Magazine and Journal of Science* 40.300 (1949), pp. 99–115. ISSN: 1941-5982. DOI: `10.1080/14786444908561215`.

[82] J. R. Eshbach and R. W. Damon. “Surface Magnetostatic Modes and Surface Spin Waves”. In: *Physical Review* 118.5 (1960), pp. 1208–1210. ISSN: 0031-899X. DOI: `10.1103/PhysRev.118.1208`.

[83] T. van der Sar, F. Casola, R. Walsworth, and A. Yacoby. “Nanometre-scale probing of spin waves using single-electron spins”. In: *Nature communications* 6 (2015), p. 7886. DOI: `10.1038/ncomms8886`.

[84] S. Hong, M. S. Grinolds, L. M. Pham, D. Le Sage, L. Luan, R. L. Walsworth, and A. Yacoby. “Nanoscale magnetometry with NV centers in diamond”. In: *MRS Bulletin* 38.2 (2013), pp. 155–161. ISSN: 0883-7694. DOI: `10.1557/mrs.2013.23`.

[85] S. Shikata, T. Tanno, T. Teraji, H. Kanda, T. Yamada, and J.-i. Kushibiki. “Precise measurements of diamond lattice constant using Bond method”. In: *Japanese Journal of Applied Physics* 57.11 (2018), p. 111301. ISSN: 0021-4922. DOI: `10.7567/JJAP.57.111301`.

[86] C. J. Wort and R. S. Balmer. “Diamond as an electronic material”. In: *Materials Today* 11.1-2 (2008), pp. 22–28. ISSN: 13697021. DOI: `10.1016/S1369-7021(07)70349-8`.

[87] *Element Six, Diamond handbook.* https://e6cvd.com/media/wysiwyg/pdf/Element_Six_CVD_Diamond_handbook_2022.pdf. 2022.

[88] M. Radtke, E. Bernardi, A. Slablab, R. Nelz, and E. Neu. "Nanoscale sensing based on nitrogen vacancy centers in single crystal diamond and nanodiamonds". In: *Nano Futures* 3.4 (2019), p. 042004. DOI: 10.1088/2399-1984/ab5f9b.

[89] U. F. S. D'Haenens-Johansson, J. E. Butler, and A. N. Katrusha. "Synthesis of Diamonds and Their Identification". In: *Reviews in Mineralogy and Geochemistry* 88.1 (2022), pp. 689–753. ISSN: 1529-6466. DOI: 10.2138/rmg.2022.88.13.

[90] M. Schwander and K. Partes. "A review of diamond synthesis by CVD processes". In: *Diamond and Related Materials* 20.9 (2011), pp. 1287–1301. ISSN: 09259635. DOI: 10.1016/j.diamond.2011.08.005.

[91] F. C. Waldermann, P. Olivero, J. Nunn, K. Surmacz, Z. Y. Wang, D. Jaksch, R. A. Taylor, I. A. Walmsley, M. Draganski, P. Reichart, A. D. Greentree, D. N. Jamieson, and S. Prawer. "Creating diamond color centers for quantum optical applications". In: *Diamond and Related Materials* 16.11 (2007), pp. 1887–1895. ISSN: 09259635. DOI: 10.1016/j.diamond.2007.09.009.

[92] T.-L. Wee, Y.-K. Tzeng, C.-C. Han, H.-C. Chang, W. Fann, J.-H. Hsu, K.-M. Chen, and Y.-C. Yu. "Two-photon excited fluorescence of nitrogen-vacancy centers in proton-irradiated type Ib diamond". In: *The journal of physical chemistry. A* 111.38 (2007), pp. 9379–9386. ISSN: 1089-5639. DOI: 10.1021/jp073938o.

[93] A. D. Greentree, P. Olivero, M. Draganski, E. Trajkov, J. R. Rabeau, P. Reichart, B. C. Gibson, S. Rubanov, S. T. Huntington, D. N. Jamieson, and S. Prawer. "Critical components for diamond-based quantum coherent devices". In: *Journal of Physics: Condensed Matter* 18.21 (2006), S825–S842. ISSN: 0953-8984. DOI: 10.1088/0953-8984/18/21/S09.

[94] J. Meijer, B. Burchard, M. Domhan, C. Wittmann, T. Gaebel, I. Popa, F. Jelezko, and J. Wrachtrup. "Generation of single color centers by focused nitrogen implantation". In: *Applied Physics Letters* 87.26 (2005). ISSN: 0003-6951. DOI: 10.1063/1.2103389.

[95] C. Santori, P. E. Barclay, K.-M. C. Fu, and R. G. Beausoleil. "Vertical distribution of nitrogen-vacancy centers in diamond formed by ion implantation and annealing". In: *Physical Review B* 79.12 (2009). ISSN: 1098-0121. DOI: 10.1103/PhysRevB.79.125313.

[96] N. B. Manson, J. P. Harrison, and M. J. Sellars. "Nitrogen-vacancy center in diamond: Model of the electronic structure and associated dynamics". In: *Physical Review B* 74.10 (2006). ISSN: 1098-0121. DOI: 10.1103/PhysRevB.74.104303.

[97] T. Gaebel, M. Domhan, C. Wittmann, I. Popa, F. Jelezko, J. Rabeau, A. Greentree, S. Prawer, E. Trajkov, P. R. Hemmer, and J. Wrachtrup. "Photochromism in single nitrogen-vacancy defect in diamond". In: *Applied Physics B* 82.2 (2006), pp. 243–246. ISSN: 0946-2171. DOI: 10.1007/s00340-005-2056-2.

[98] A. e. a. Gruber. “Scanning Confocal Optical Microscopy and Magnetic Resonance on Single Defect Centers”. In: *Science* 276.5321 (1997), pp. 2012–2014. ISSN: 0036-8075. DOI: `10.1126/science.276.5321.2012`.

[99] L. García-Álvarez, A. Ferraro, and G. Ferrini. “From the Bloch Sphere to Phase-Space Representations with the Gottesman–Kitaev–Preskill Encoding”. In: *International Symposium on Mathematics, Quantum Theory, and Cryptography*. Ed. by T. Takagi. Vol. 33. Mathematics for Industry Ser. Singapore: Springer Singapore Pte. Limited, 2021, pp. 79–92. ISBN: 978-981-15-5190-1. DOI: `10.1007/978-981-15-5191-8{\textunderscore}9`.

[100] P. Krantz, M. Kjaergaard, F. Yan, T. P. Orlando, S. Gustavsson, and W. D. Oliver. “A quantum engineer’s guide to superconducting qubits”. In: *Applied Physics Reviews* 6.2 (2019). DOI: `10.1063/1.5089550`.

[101] E. V. Levine, M. J. Turner, P. Kehayias, C. A. Hart, N. Langellier, R. Trubko, D. R. Glenn, R. R. Fu, and R. L. Walsworth. “Principles and techniques of the quantum diamond microscope”. In: *Nanophotonics* 8.11 (2019), pp. 1945–1973. ISSN: 2192-8606. DOI: `10.1515/nanoph-2019-0209`.

[102] H. H. Vallabhapurapu, J. P. Slack-Smith, V. K. Sewani, C. Adambukulam, A. Morello, J. J. Pla, and A. Laucht. “Fast Coherent Control of a Nitrogen-Vacancy-Center Spin Ensemble Using a KTaO3 Dielectric Resonator at Cryogenic Temperatures”. In: *Physical Review Applied* 16.4 (2021). DOI: `10.1103/PhysRevApplied.16.044051`. URL: `https://journals.aps.org/prapplied/pdf/10.1103/PhysRevApplied.16.044051`.

[103] B. Naydenov, F. Dolde, L. T. Hall, C. Shin, H. Fedder, L. C. L. Hollenberg, F. Jelezko, and J. Wrachtrup. “Dynamical decoupling of a single-electron spin at room temperature”. In: *Physical Review B* 83.8 (2011). ISSN: 1098-0121. DOI: `10.1103/PhysRevB.83.081201`. URL: `https://journals.aps.org/prb/pdf/10.1103/PhysRevB.83.081201`.

[104] A. Jarmola, V. M. Acosta, K. Jensen, S. Chemerisov, and D. Budker. “Temperature- and magnetic-field-dependent longitudinal spin relaxation in nitrogen-vacancy ensembles in diamond”. In: *Physical review letters* 108.19 (2012), p. 197601. DOI: `10.1103/PhysRevLett.108.197601`.

[105] J.-C. Jaskula, E. Bauch, S. Arroyo-Camejo, M. D. Lukin, S. W. Hell, A. S. Trifonov, and R. L. Walsworth. “Superresolution optical magnetic imaging and spectroscopy using individual electronic spins in diamond”. In: *Optics express* 25.10 (2017), pp. 11048–11064. DOI: `10.1364/OE.25.011048`.

[106] K. Y. Han, S. K. Kim, C. Eggeling, and S. W. Hell. “Metastable dark States enable ground state depletion microscopy of nitrogen vacancy centers in diamond with diffraction-unlimited resolution”. In: *Nano letters* 10.8 (2010), pp. 3199–3203. DOI: `10.1021/nl102156m`.

[107] X. Chen, C. Zou, Z. Gong, C. Dong, G. Guo, and F. Sun. “Subdiffraction optical manipulation of the charge state of nitrogen vacancy center in diamond”. In: *Light: Science & Applications* 4.1 (2015), e230–e230. DOI: `10.1038/lsa.2015.3`.

[108] J.-P. Tetienne, T. Hingant, J.-V. Kim, L. H. Diez, J.-P. Adam, K. Garcia, J.-F. Roch, S. Rohart, A. Thiaville, D. Ravelosona, and V. Jacques. “Nanoscale imaging and control of domain-wall hopping with a nitrogen-vacancy center microscope”. In: *Science (New York, N.Y.)* 344.6190 (2014), pp. 1366–1369. DOI: 10.1126/science.1250113.

[109] R. Schirhagl, K. Chang, M. Loretz, and C. L. Degen. “Nitrogen-vacancy centers in diamond: nanoscale sensors for physics and biology”. In: *Annual review of physical chemistry* 65 (2014), pp. 83–105. DOI: 10.1146/annurev-physchem-040513-103659.

[110] Rayleigh. “XV. On the theory of optical images, with special reference to the microscope”. In: *The London, Edinburgh, and Dublin Philosophical Magazine and Journal of Science* 42.255 (1896), pp. 167–195. ISSN: 1941-5982. DOI: 10.1080/14786449608620902.

[111] Rayleigh. “XXXI. Investigations in optics, with special reference to the spectroscope”. In: *The London, Edinburgh, and Dublin Philosophical Magazine and Journal of Science* 8.49 (1879), pp. 261–274. DOI: 10.1080/14786447908639684.

[112] V. K. Sewani, H. H. Vallabhapurapu, Y. Yang, H. R. Firgau, C. Adambukulam, B. C. Johnson, J. J. Pla, and A. Laucht. “Coherent control of NV− centers in diamond in a quantum teaching lab”. In: *American Journal of Physics* 88.12 (2020), pp. 1156–1169. ISSN: 0002-9505. DOI: 10.1119/10.0001905.

[113] J. H. Scofield. “Frequency-domain description of a lock-in amplifier”. In: *American Journal of Physics* 62.2 (1994), pp. 129–133. ISSN: 0002-9505. DOI: 10.1119/1.17629.

[114] L. Colombo. “Combining Nitrogen-Vacancy and Time-Resolved Kerr Microscopy”. Technische Universität München, 2023.

[115] F. Vilsmeier, C. Riedel, and C. H. Back. “Spatial control of hybridization-induced spin-wave transmission stop band”. In: *Applied Physics Letters* 124.13 (2024). ISSN: 0003-6951. DOI: 10.1063/5.0188193.

[116] K. Perzlmaier, G. Woltersdorf, and C. H. Back. “Observation of the propagation and interference of spin waves in ferromagnetic thin films”. In: *Physical Review B* 77.5 (2008). ISSN: 1098-0121. DOI: 10.1103/physrevb.77.054425.

[117] Y. Au, T. Davison, E. Ahmad, P. S. Keatley, R. J. Hicken, and V. V. Kruglyak. “Excitation of propagating spin waves with global uniform microwave fields”. In: *Applied Physics Letters* 98.12 (2011). ISSN: 0003-6951. DOI: 10.1063/1.3571444. URL: https://pubs.aip.org/aip/apl/article/98/12/122506/339841.

[118] H. G. Bauer, J.-Y. Chauleau, G. Woltersdorf, and C. H. Back. “Coupling of spin-wave modes in wire structures”. In: *Applied Physics Letters* 104.10 (2014), p. 102404. ISSN: 0003-6951. DOI: 10.1063/1.4868250. URL: https://pubs.aip.org/aip/apl/article/104/10/102404/130475.

[119] J. Stigloher, T. Taniguchi, H. S. Körner, M. Decker, T. Moriyama, T. Ono, and C. H. Back. “Observation of a Goos-Hänchen-like Phase Shift for Magnetostatic Spin Waves”. In: *Physical review letters* 121.13 (2018). DOI: 10.1103/physrevlett.121.137201.

[120] R. Dreyer, N. Liebing, E. R. J. Edwards, A. Müller, and G. Woltersdorf. “Spin-wave localization and guiding by magnon band structure engineering in yttrium iron garnet”. In: *Phys. Rev. Mat.* 5.6 (2021). DOI: 10.1103/PhysRevMaterials.5.064411.

[121] A. Nayak. “Development of a Widefield NV Imager for Magnetic Nanostructures”. Technische Universität München, 2024.

[122] A. Dréau, M. Lesik, L. Rondin, P. Spinicelli, O. Arcizet, J.-F. Roch, and V. Jacques. “Avoiding power broadening in optically detected magnetic resonance of single NV defects for enhanced dc magnetic field sensitivity”. In: *Physical Review B* 84.19 (2011). ISSN: 1098-0121. DOI: 10.1103/PhysRevB.84.195204.

[123] T. de Guillebon, B. Vindolet, J.-F. Roch, V. Jacques, and L. Rondin. “Temperature dependence of the longitudinal spin relaxation time T1 of single nitrogen-vacancy centers in nanodiamonds”. In: *Physical Review B* 102.16 (2020). ISSN: 1098-0121. DOI: 10.1103/PhysRevB.102.165427.

[124] J.-P. Tetienne, T. Hingant, L. Rondin, A. Cavaillès, L. Mayer, G. Dantelle, T. Gacoin, J. Wrachtrup, J.-F. Roch, and V. Jacques. “Spin relaxometry of single nitrogen-vacancy defects in diamond nanocrystals for magnetic noise sensing”. In: *Physical Review B* 87.23 (2013). ISSN: 1098-0121. DOI: 10.1103/physrevb.87.235436.

[125] R. Hanson, V. V. Dobrovitski, A. E. Feiguin, O. Gywat, and D. D. Awschalom. “Coherent dynamics of a single spin interacting with an adjustable spin bath”. In: *Science (New York, N.Y.)* 320.5874 (2008), pp. 352–355. DOI: 10.1126/science.1155400.

[126] S. Ernst, P. J. Scheidegger, S. Diesch, L. Lorenzelli, and C. L. Degen. “Temperature Dependence of Photoluminescence Intensity and Spin Contrast in Nitrogen-Vacancy Centers”. In: *Physical review letters* 131.8 (2023), p. 086903. DOI: 10.1103/PhysRevLett.131.086903.

[127] I. Cardoso Barbosa, J. Gutsche, D. Lönard, S. Dix, and A. Widera. In: *Phy. Rev. Research* 6.2 (2024). DOI: 10.1103/PhysRevResearch.6.023078.

[128] V. Cherepanov, I. Kolokolov, and V. L’vov. “The saga of YIG: Spectra, thermodynamics, interaction and relaxation of magnons in a complex magnet”. In: *Physics Reports* 229.3 (1993), pp. 81–144. ISSN: 0370-1573. DOI: 10.1016/0370-1573(93)90107-O.

[129] P. Andrich, C. F. de las Casas, X. Liu, H. L. Bretscher, J. R. Berman, F. J. Heremans, P. F. Nealey, and D. D. Awschalom. “Long-range spin wave mediated control of defect qubits in nanodiamonds”. In: *npj Quantum Information* 3.1 (2017). DOI: 10.1038/s41534-017-0029-z.

[130] W. Greiner. "Faraday's Law of Induction". In: *Classical electrodynamics*. Ed. by W. Greiner and D. A. Bromley. Classical theoretical physics. New York, Berlin, and Heidelberg: Springer, 1998, pp. 237–249. ISBN: 978-0-387-94799-0. DOI: `10.1007/978-1-4612-0587-6{\textunderscore}12`.

[131] W. Greiner and D. A. Bromley, eds. *Classical electrodynamics*. Classical theoretical physics. New York, Berlin, and Heidelberg: Springer, 1998. ISBN: 978-0-387-94799-0. DOI: `10.1007/978-1-4612-0587-6`.

[132] E. Lenz. "Ueber die Bestimmung der Richtung der durch elektrodynamische Vertheilung erregten galvanischen Ströme". In: *Annalen der Physik* 107.31 (1834), pp. 483–494. ISSN: 1521-3889. DOI: `10.1002/andp.18341073103`. URL: `https://onlinelibrary.wiley.com/doi/10.1002/andp.18341073103`.

[133] T. K. Yeung, D. Le Sage, L. M. Pham, P. L. Stanwix, and R. L. Walsworth. "Antireflection coating for nitrogen-vacancy optical measurements in diamond". In: *Applied Physics Letters* 100.25 (2012). ISSN: 0003-6951. DOI: `10.1063/1.4730401`.

[134] J. Yoon, J. Jeong, and D. Lee. "Field averaging effect and estimation of minimum sample size in wide-field diamond microscopy". In: *Journal of the Korean Physical Society* 82.10 (2023), pp. 970–974. ISSN: 0374-4884. DOI: `10.1007/s40042-023-00801-1`.

[135] C. Lüthi, L. Flacke, A. Aqeel, A. Kamra, R. Gross, C. Back, and M. Weiler. "Hybrid magnetization dynamics in Cu2OSeO3/NiFe heterostructures". In: *Applied Physics Letters* 122.1 (2023). ISSN: 0003-6951. DOI: `10.1063/5.0128733`. URL: `https://pubs.aip.org/aip/apl/article/122/1/012401/2876434/Hybrid-magnetization-dynamics-in-Cu2OSeO3-NiFe`.

[136] C. Lüthi, L. Colombo, F. Vilsmeier, and C. Back. *Comparative analysis of spin wave imaging using nitrogen vacancy centers and time resolved magneto-optical measurements*. URL: `http://arxiv.org/pdf/2405.02014`.

A

NON-PHASE-RESOLVED IMAGING WITH REVERSED FIELD DIRECTION

In Fig. A.1, NV centers were continuously excited at 2.47 GHz by a MW current while the sample was scanned. In comparison to Fig. 6.6, the in-plane external magnetic field $\mathbf{B_0}$ direction was rotated by 180°. The DE spin waves now travel in the opposite direction, resulting in an increased contrast in the region between the U-shaped microstrip line.

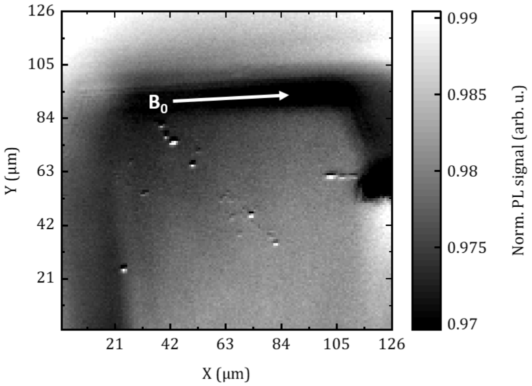

Figure A.1.: PL signal of NV centers excited at 2.47 GHz by a MW current sent through a U-shaped microstrip line while the sample is scanned. The external magnetic field $\mathbf{B_0}$, rotated by 180° compared to Fig.6.6, causes DE spin waves to propagate in the opposite direction, enhancing the contrast between the U-shaped microstrip line.

B

ANGLE CORRECTION

In Fig. B.1, the PL signal for a spatial scan over the sample is shown for different external fields in the range of 22.33 mT to 26.94 mT increasing from (a) to (f). The scanning direction of the stage on which the sample is mounted is slightly misaligned with S2. By rotating the images by an angle $\theta = -2.5°$, this misalignment can be corrected.

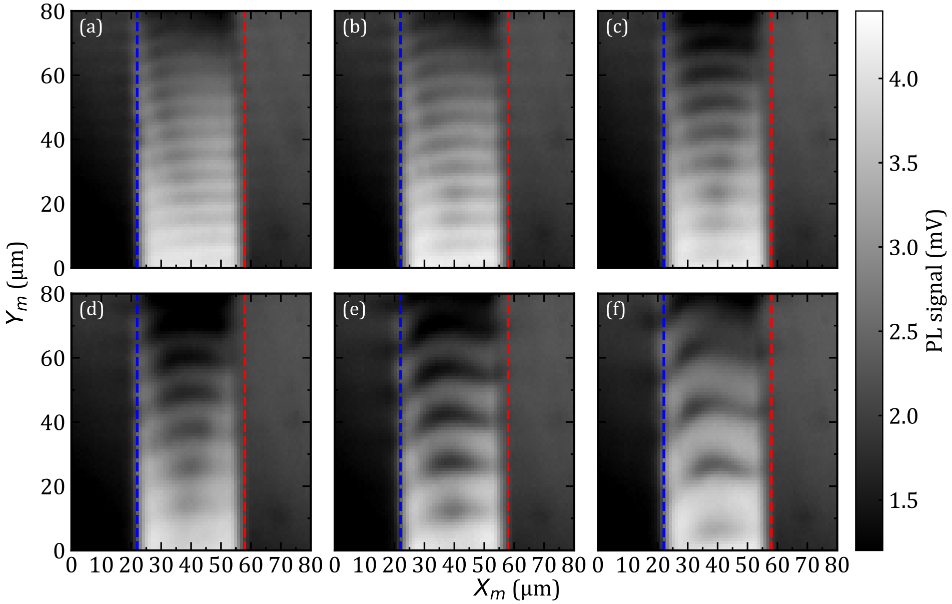

Figure B.1.: Non-rotated images of the NV center spin wave measurements. The microstrip line S2 is not perfectly aligned with the scanning direction of the stage.

LIST OF ABBREVIATIONS

AC Alternating Current

APD Avalanche Photodiode

AR Anti-Reflection

BV Backward Volume

CMOS Complementary Metal-Oxide Semiconductor

CPW Coplanar Waveguide

CW Continuous-Wave

CVD Chemical Vapor Deposition

DC Direct Current

DE Damon-Eshbach

ESR Electron Spin Resonance

FM Flip Mirror

FMR Ferromagnetic Resonance

FV Forward Volume

HPHT High Pressure High Temperature

IP In-Plane

ISC Intersystem Crossing

L Lens

LED Light-Emitting Diode

LMOKE Longitudinal Magneto-Optical Kerr Effect

LP Long-Pass

M Mirror

MW Microwave

ND Neutral-Density

NV Nitrogen-Vacancy

OOP Out-Of-Plane

ODMR Optically Detected Magnetic Resonance

PL Photoluminescence

PMOKE Polar Magneto-Optical Kerr Effect

P Polarizer

PSB Phonon Sideband

Py Permalloy

SP DM Short-Pass Dichroic Mirror

SNS Super-Nyquist Sampling

TR-MOKE Time-Resolved Magneto-Optical Kerr Effect

YIG Yttrium Iron Garnet

ZFD Zero-Field Dip

ZPL Zero-Phonon Line

LIST OF FIGURES

LIST OF TABLES

LIST OF PUBLICATIONS

2. C. Lüthi, L. Flacke, A. Aqeel, A. Kamra, R. Gross, C. Back, and M. Weiler. "Hybrid magnetization dynamics in Cu2OSeO3/NiFe heterostructures". In: *Applied Physics Letters* 122.1 (2023). ISSN: 0003-6951. DOI: `10.1063/5.0128733`. URL: `https://pubs.aip.org/aip/apl/article/122/1/012401/2876434/Hybrid-magnetization-dynamics-in-Cu2OSeO3-NiFe`

1. C. Lüthi, L. Colombo, F. Vilsmeier, and C. Back. *Comparative analysis of spin wave imaging using nitrogen vacancy centers and time resolved magneto-optical measurements.* URL: `http://arxiv.org/pdf/2405.02014`

ACKNOWLEDGEMENTS

I would like to express my thanks to friends and colleagues who helped make this work possible. A heartfelt thanks to:

Prof. Dr. Christian Back, for giving me the opportunity to pursue my PhD at his chair. Thank you for the valuable advices and discussions, and for always having an open door for all kinds of matters.

Prof. Dr. Dominik Bucher for sharing his expertise on NV centers with us and for serving as the second examiner of this thesis.

Prof. Dr. Martin Brandt, for providing us with his expertise on NV centers.

Prof. Dr. Toeno van der Sar from TU Delft, for the opportunity to visit his laboratories.

Prof. Dr. Rudolf Gross, for acting as the mentor throughout my project.

Dr. Lin Chen, for your helpfulness and the good advice on various scientific problems.

Lukas Colombo and Ankita Nayak, for their motivation, helpfulness, and excellent collaboration. Special thanks to Lukas for the numerous insightful discussions about NV centers and various other topics.

Dr. Thomas Meier, for proofreading this thesis, for your helpfulness, and for the valuable advices.

Anastasiia Korniienko and Robin Brabants, for the friendship that began in the office and extended into our personal lives. Thank you for the lovely evenings and trips we spent together.

Laura Pietanesi, Wilhelm Witl, Sina Mehboodi, and Maximilian Mangold, for the fun coffee breaks, lunches, and poker nights.

Franz Vilsmeier, for his help with the SNS-MOKE measurements and for proofreading the paper.

Gertrud Weiß, for your friendliness and patience in assisting with organizational matters.

Stefan Lichtenauer, for your helpful advices and crafting many technical components for my setup.

The entire EFS group, for creating a great atmosphere at the chair.

My friends from the "Stammtisch", Klaus Eibensteiner, Katharina Raschke, Manuel Lebert, Markus Edeer, Patrick Wastian, Wolfgang Gottwald, Jakob Unfried, and Rika Unkelbach, for the fun dinners that made many workdays end on a cheerful note.

My relatives Sylvie, Albi, Philippe, and Fabio, for the great holidays and family gatherings that always brought a pleasant break to my free time.

My parents, for their support and their lighthearted approach to my work. Thank you also for the many great weekends in Zurich.

Aline Lüthi, for being the best sister in the world. Thank you for the wonderful holidays together and your support in every situation.

Nico Huber, for always supporting, motivating, and amusing me, and for the great conversations about the world (and physics). For the lovely evenings together and all the fun I have with you. I love you a lot.